

**A Scanning Tunnelling Microscopy and
Spectroscopic Study of Bromine
Functionalised Molecules on
Metal Surfaces**



A thesis for the degree of
PHILOSOPHIAE DOCTOR

Tom Carpy B.Sc

School of Physical Sciences
Dublin City University

Research Supervisor: **Dr. Tony Cafolla**

January 2015

Declaration

I hereby certify that this material, which I now submit for assessment on the programme of study leading to the award of Doctor of Philosophy is entirely my own work, that I have exercised reasonable care to ensure that the work is original, and does not to the best of my knowledge breach any law of copyright, and had not been taken from the work of others save and to the extent that such work has been cited and acknowledged within the text of my work.

Signed: _____

ID No.: _____

Date: _____

Acknowledgements

First and foremost I must thank a very patient and intelligent man, Dr Tony Cafolla. His guidance, dedication and enthusiasm made this all possible. From early morning STM scanning to discussions regarding our most recent food devouring adventures helped make this project a (mostly) enjoyable experience.

Thank you to all my lab friends in DCU and MAX-Lab, Dr Catherine Doyle, Dr John Cunniffe, Dr Hooi Ling Lee, Mr Konstantin Simonov and Dr Alexei Preobrajenski. Also, thank you to Dr Enda McGlynn for recommending me for entry into my B.Sc at DCU which provided some base knowledge for my PhD.

Thank you to Science Foundation Ireland for giving me money. I could not have survived without it.

Thank you to all my friends in DCU for keeping me sane. Henry, Dan, Niamh and numerous others in the physics department.

Last but by no means least, I must acknowledge and give a special thank you to five people. My parents Ken and Doris, without their constant support and fantastic genetic code this would never have been possible; Paul and Adam, my brothers, who only receive a mention because they are family; and finally, I would like to thank my most loyal and loving friend, Denise.

Thank you all.

For the Old Dears, Bob and Emma

Publications and Conference Contributions

Papers:

Effect of Substrate Chemistry on the Bottom-Up Fabrication of Graphene Nanoribbons: Combined Core-Level Spectroscopy and STM Study

Simonov, K.A., Vinogradov, N.A., Vinogradov, A.S., Generalov, A.V., Zagrebina, E.M., Martensson, N., Cafolla, A.A., Carpy, T., Cunniffe, J.P. & Preobrajenski, A.B. 2014, Journal of Physical Chemistry C, vol. 118, no. 23, pp. 12532-12540.

Oral Presentations:

An STM and XPS study of covalently bonded 2, 3, 6, 7, 10, 11 hexabromotriphenylene on Au(111), Ag(111) and Cu(111)

ECOSS-29, Edinburgh, Scotland, 7th September 2012.

Bottom-up Fabrication of Graphene Nanoribbons on Metal Surfaces

EVC 2014 – 13th European Vacuum Conference, Aveiro, Portugal, 8th September 2014

Poster Presentations:

An STM and XPS study of covalently bonded 2, 3, 6, 7, 10, 11 hexabromotriphenylene on Au(111), Ag(111) and Cu(111)

BOC Gases Postgraduate Poster Competition, School of Physical Sciences, Dublin City University, 20th February 2013.

The growth and characterisation of Graphene Nanoribbons on Au(111), Ag(111) and Cu(111)

2014 IOP Ireland Spring Meeting Conference, Dublin, Ireland, 8th March 2014. Finalist.

Abstract

This thesis discusses deposition, self-assembly, polymerisation and covalent bonding of bromine functionalised molecules on Au(111), Ag(111), Cu(111) and Cu(110) metal substrates are investigated. The debromination and subsequent covalent bonding is found to depend heavily on the reactivity of the substrate, the molecular coverage and anneal temperatures. Characterisation was performed using scanning tunnelling microscopy (STM), x-ray photoelectron spectroscopy (XPS) and synchrotron based photoelectron spectroscopy (PES) as well as x-ray absorption spectroscopy (XAS).

Deposition of hexabromotriphenylene (**HBTP**) on the Au(111), Ag(111) and Cu(111) surfaces resulted in the formation of disordered, covalently bonded nano-networks which remained stable up to a temperature of 300°C. C-Br bonds of HBTP can cleave at room temperature (RT) on Ag and Cu due to the substrate reactivity allowing new covalent C-C bonds to form. In the case of Cu, disordered networks are observed at RT while in contrast, more ordered networks develop on the Ag and Au substrates after annealing to 150°C and 200°C respectively. On the Au(111) surface bromine desorption begins at 250°C whereas on the Ag(111) and Cu(111) surfaces the atomic bromine remains on the surface and forms a $(\sqrt{3}\times\sqrt{3})R30^\circ$ structure.

The formation of atomically precise graphene nanoribbons (GNR) from a 10,10'-dibromo-9,9'-bianthryl (**DBBA**) precursor molecule was investigated on the Au(111), Ag(111), Cu(111) and Cu(110) surfaces. After deposition, the **DBBA** molecules undergo two thermally induced chemical changes; (i) a debromination reaction to produce covalently bonded polymerised chains and (ii) a cyclodehydrogenation reaction at higher temperatures to form GNRs. The threshold for the debromination reaction, polymerisation and final cyclodehydrogenation reaction decreases proportionally with the reactivity of the substrate.

Ni(II) 5,15-dibromo-10,20-diphenyl (DBrDPP) was studied on the Cu(110) surface to investigate its suitability for integration into GNRs. Thermally induced covalent bonding of **DBrDPP** was observed via a C-Cu-C organo-metallic bond while a Ni-Cu ion exchange reaction occurs in the porphyrin macrocycle. At higher anneal temperatures domains of graphene emerge which exhibit a moiré pattern with varying periodicities indicating a lattice mismatch between the graphene layer and the underlying copper substrate.

Contents

Declaration.....	ii
Acknowledgements.....	iii
List of Publications	v
Abstract	vi
List of Figures.....	xi
List of Abbrevs	xxi

Chapter 1

Introduction

1.1 Graphene and Moiré pattern.....	3
1.2 Graphene Nanoribbons (GNRs).....	4
1.3 Thesis outline.....	5
1.4 References	7

Chapter 2

Theory and experimental details

2.1 Omicron Ultra High Vacuum (UHV)	12
2.2 Scanning Tunnelling Microscopy	13
2.2.1 Introduction	13
2.2.2 Theory of STM.....	15
2.2.3 STM Tip Preparation	17
2.2.4 STM Data Analysis	18

2.3 Photoelectron Spectroscopy	19
2.3.1 X-Ray Photoelectron Spectroscopy	19
2.3.2 XPS Data Analysis	24
2.3.3 Synchrotron Radiation	25
2.3.4 PES Data Analysis	26
2.3.5 X-ray Absorption Spectroscopy	27
2.4 Ullman Reaction	29
2.5 Metal Surfaces	30
2.5.1 The Au(111), Ag(111) and Cu(111) Surfaces	30
2.5.2 The Cu(110) Surface	32
2.6 Evaporation Cell	32
2.7 Graphene and Graphene Nanoribbons	32
2.8 References	35

Chapter 3

Self-assembly and Covalent Bonding of Hexabromotriphenylene (HBTP) Molecules on Au(111), Ag(111) and Cu(111) Surfaces

3.1 Introduction	38
3.2 STM and XPS Study of HBTP on the Au(111) Surface	40
3.3 Covalent Bonding Configurations on the Au(111) Surface	45
3.4 STM and XPS Study of HBTP on the Ag(111) Surface	48

3.5 STM and XPS Study of HBTP on the Cu(111) Surface	53
3.6 Comparison of HBTP on Au(111), Ag(111) and Cu(111) Surfaces at Room Temperature	57
3.7 Dissociated Bromine on the Ag(111) and Cu(111) Surfaces	58
3.8 Summary.....	61
3.9 References	63

Chapter 4

STM, PES and XAS Study of 10,10'-dibromo-9,9'-biantracene (DBBA) on Au(111), Ag(111) and Cu(111) Surfaces

4.1 Introduction	65
4.2 Formation of GNRs on the Au(111) Surface.....	68
4.3 GNR Formation on the Ag(111) Surface	79
4.4 Formation of GNRs on the Cu(111) Surface.....	88
4.5 Summary.....	101
4.6 References	104

Chapter 5

STM Study of DBBA in the Cu(110) Surface

5.1 Introduction	107
5.2 Submonolayer Coverage of DBBA on the Cu(110) Surface.....	107

5.3 Decomposition of DBBA Molecules on the Cu(110) Surface	114
5.4 Graphene Formation from DBBA Precursors on the Cu(110) Surface	116
5.5 Summary.....	119
5.6 References	120

Chapter 6

An STM Study of Dibromodiphenyl Porphyrin (DBrDPP) on the Cu(110) Surface

6.1 Introduction	122
6.2 STM Study of DBrDPP on the Cu(110) Surface at Low Coverage	123
6.3 STM Study of DBrDPP on the Cu(110) Surface at High Coverage.....	130
6.4 Summary.....	146
6.5 References	147

Chapter 7

Future Work and Summary

7.1 Future Work.....	149
7.2 Summary.....	158
7.3 References	161

List of Figures

1.1 Bonding strategy for a brominated molecule (DBBA), to radical formation and subsequent covalently bonded chain.....	5
2.1 Bonding strategy for a brominated molecule (DBBA), to radical formation and subsequent covalently bonded chain.....	13
2.2 Schematic diagram showing the STM and its components.....	14
2.3 Schematic diagram of a sample in close proximity to a tip where a bias is induced enabling quantum tunnelling to occur.....	15
2.4 Representation of the interaction of a photon with energy $h\nu$ and core level electrons bound by E_b	19
2.5 Electron mean free path curve	21
2.6 Schematic of a Mg/Al twin anode x-ray source	23
2.7 Hemispherical analyser showing electron path from sample to detector.....	24
2.8 Experimental stations at synchrotron radiation facility. D1011 beamline, MAX-lab, Lund University, Sweden.....	26
2.9 Principle of X-ray Absorption Spectroscopy.....	27
2.10 Orientation of π^* and σ^* molecular orbitals on a benzene ring	28
2.11 Ullmann reaction with copper chosen as the catalyst	29
2.12 Ullmann reaction showing the intermediate stage where metal and halogen form a metal/organic complex.....	29
2.13 STM images of atomically clean substrates	30

2.14 Face-centred cubic crystal showing the (111) plane where ‘a’ is the lattice parameter.....	31
2.15 The (110) plane of a FCC crystal where ‘a’ is the lattice parameter	32
2.16 Structural model for graphene, top down view.....	33
2.17 Schematic diagrams showing the orbital configuration from a side and top down view.....	33
2.18 Structural model for a graphene nanoribbon	34
3.1 Chemical structure of HBTP with dimensions calculated from Chems sketch	39
3.2 STM for 1ML of HBTP deposited on Au(111) held at room temperature	40
3.3 XPS of ~1 ML of HBTP deposited on room temperature Au(111) and progressive anneal stages.....	41
3.4 STM image of HBTP molecules deposited at RT and annealed to 350°C.....	42
3.5 STM for HBTP deposited on Au(111) held at a temperature of (a) 150°C ($V_b = 1.7V$, $I_t = 0.06nA$), (b) and (c) 200°C ($V_b = 1.4V$, $I_t = 0.32nA$) and (d) 250°C ($V_b = 1.0V$, $I_t = 0.45nA$).	43
3.6 XPS of HBTP deposited onto elevated substrate temperatures.....	44
3.7 Different bonding configurations of HBTP molecules	45
3.8 Different covalent bonding formations of HBTP on the Au(111) surface.....	46
3.9 STM images for approximately 1ML of HBTP deposited on the Ag(111) surface held at room temperature	48
3.10 XPS of ~1 ML of HBTP deposited on the Ag(111) surface held at RT and subsequently annealed.....	49

3.11 STM images of HBTP deposited at RT on the Ag(111) surface and subsequently annealed to 150°C	50
3.12 STM for HBTP deposited at RT on the Ag(111) surface and subsequently annealed to 250°C.....	51
3.13 XPS of HBTP deposited on the Ag(111) surface held at different temperatures	51
3.14 STM images of HBTP deposited on the Ag(111) surface elevated to (a) 420K, (b) 470K and (c) 520K	52
3.15 STM images for HBTP on Cu(111).....	53
3.16 XPS spectra of ~0.5ML of HBTP deposited on room temperature Cu(111) and subsequently annealed to 200°C and then 250°C	54
3.17 XPS of HBTP deposited on the Cu(111) surface held at different temperatures and then annealed from 150°C to 285°C.....	55
3.18 STM images of HBTP deposited on the Cu(111) surface elevated to (a) 150°C, (b) 200°C and (c) 150°C	56
3.19 XPS spectra of HBTP deposited at room temperature on the Au(111), Ag(111) and Cu(111) surfaces.....	58
3.20 Evidence of dissociated bromine structure on the Ag(111) surface after RT deposition of HBTP and subsequent 250°C anneal.	59
3.21 Graphical representation of the Ag(111) surface, bromine structural overlayer and corresponding lattice vectors	60
3.22 STM images of HBTP on Cu(111) showing (a) a disordered covalently bonded region of HBTP and (b) a magnification of the white circled region, both at ($V_b = 1.5V$, $I_t = 0.10nA$).	60

3.23 Graphical representation of the Cu(111) surface, bromine structural overlayer and corresponding lattice vectors.....	61
4.1 Chemical structure of DBBA with dimensions calculated from Chemskech and graphical representation, with and without hydrogens	66
4.2 Reaction mechanisms showing the formation of 7-AGNRs from DBBA precursor molecules.....	68
4.3 STM images of 0.65ML of DBBA deposited onto RT Au(111) and subsequently annealed to 200°C	69
4.4 STM images of approximately 0.65ML of DBBA deposited onto RT Au(111) and then annealed to 400C.....	71
4.5 GNR length distribution when grown on the Au(111) substrate	72
4.6 Apparent GNR height on the Au(111) surface at varying voltages.....	73
4.7 Fast Fourier Transform (FFT) of GNRs on Au(111) indicating possible preferential directional GNR growth.....	73
4.8 Evolution of the Br 3d PE spectra of DBBA/Au(111) as a function of sample temperature. $h\nu = 170\text{eV}$	74
4.9 Evolution of the C 1s PE spectra of DBBA/Au(111) as a function of sample temperature. $h\nu=380\text{eV}$	75
4.10 XAS spectra of DBBA on Au(111) showing successive anneal stages and schematic showing the chemical alterations when increasing the anneal temperature	77
4.11 STM images (a) and (c) showing the alignment of DBBA chains on the RT Ag(111) surface	79

4.12 STM image of DBBA deposited onto the Ag(111) surface after annealing to 150°C.....	80
4.13 GNRs on the Ag(111) surface taken after annealing to 370°C.....	81
4.14 Graphical representation of a 14-AGNR formed through cross dehydrogenation between adjacent 7-AGNRs	82
4.15 Evolution of the Br 3d PE spectra of DBBA/Ag(111) as a function of increasing sample temperature	83
4.16 Evolution of the C 1s PE spectra of DBBA/Ag(111) as a function of increasing sample temperature	84
4.17 XAS spectra of DBBA on Au(111) showing successive anneal stages.....	87
4.18 High density and magnified areas ((a) and (b) respectively) of DBBA molecular chains deposited at RT	88
4.19 Graphical representation of organo-metallic bonding between sequential DBBA units.....	89
4.20 (a) Large scale STM image of covalently bonded anthracene chains formed from deposition of DBBA on the Cu(111) substrate held at RT and FFT of (a).....	90
4.21 Principal crystallographic directions of the Cu(111) surface and the directions of anthracene chains.....	90
4.22 (a) STM image of the GNRs formed on the Cu(111) surface after thermal activation to 200°C and (b) a graphical representation of a GNR	91
4.23 Apparent GNR height on the Cu(111) surface at varying voltages	92
4.24 GNR distribution on the Cu(111) surface	92

4.25 (a) Large scale image of GNRs formed from deposition of DBBA on the Cu(111) substrate at RT and subsequently annealed to 200°C. (b) FFT taken from (a) of GNRs on Cu(111) indicating six preferential growth directions	93
4.26 Principal and additional crystallographic directions of the Cu(111) surface and the directions of GNRs.	93
4.27 Br 3d PE spectra of DBBA/Cu(111) as a function of increasing sample temperature.....	94
4.28 Evolution of the C 1s PE spectra of DBBA/Cu(111) as a function of increasing sample temperature	95
4.29 STM images of GNRs after annealing to 420°C.....	97
4.30 Graphene islands on Cu(111).	99
4.31 C K-edge NEXAFS spectra of DBBA on Cu(111) at 50° incidence angle taken after annealing to 100°C, 200°C and then 750°C.....	100
4.32 Graph showing the apparent heights of the GNRs.....	103
5.1 STM image showing RT deposited DBBA on the Cu(110) surface and corresponding schematic of the molecular arrangement.....	107
5.2 STM images of (a) large scale arrangement of DBBA molecules showing evidence of dimers and (b) magnified region highlighting DBBA molecules, the unit cell and bromine/copper atoms.....	108
5.3 Schematic representation of an organo-metallic link (C-Cu-C bond) between DBBA molecules in a chain and also, how a dimer could form between rows.....	109
5.4 STM images showing the different packing of DBBA molecules and most common unit cell is shown in the schematic	110

5.5 High resolution images of DBBA on Cu(110) held at 115°C	111
5.6 Schematic showing the proposed orientation of DBBA molecules on the Cu(110) surface.	112
5.7 STM images of (a) densely packed region of DBBA molecules exhibiting similar structures seen after depositing onto Cu(110) held at 115°C and (b) shows a solitary DBBA molecules highlighted by the white arrow clearly indicating the rows of the underlying substrate.....	113
5.8 STM image after annealing the surface to 300°C	113
5.9 Large scale STM image showing decomposed DBBA molecules	114
5.10 Domains of previously decomposed material are observed in this STM image which occurs after a surface anneal to 550°C.....	114
5.11 STM image of (a) island formation, (b) and (c) successive magnification of an island	115
5.12 STM images showing (a) graphene boundaries and ‘climbing’ a step edge (red oval), (b) graphene boundary exhibiting the ‘stitching’ effect.....	116
5.13 FFT of graphene image in Figure 5.12 (d) exhibiting three distinct periodicities ...	117
5.14 STM images after annealing the Cu(110) surface to 800°C.....	118
6.1 Structure of DBrDPP, dimensions determined from Chems sketch. Hydrogen atoms are not shown.....	123
6.2 STM images of 0.1ML of DBrDPP deposited on RT Cu(110) at different bias	123
6.3 STM images of the same 25 × 25 nm area taken within a 5 minute period of each other showing a single porphyrin molecule migrating towards and bonding to an already established chain	125

6.4 STM images and schematics of the DBrDPP chains and organo-metallic bonding..	126
6.5 STM images (a) (-0.91V, 0.39nA) and (b) (-0.83V, 0.45nA) showing chain alignment, (c) all possible C-Cu-C organo-metallic bonding preferences and (d) a schematic showing the movement of DBrDPP circled in the STM images	128
6.6 STM images of a post 300°C anneal of DBrDPP on the Cu(110) surface.....	129
6.7 STM image of the initial stages of DBrDPP nanoline decomposition (red arrow) and intact porphyrins (white arrow)	130
6.8 STM image after annealing to 105°C from RT deposited DBBA molecules.....	131
6.9 Schematic diagram showing the arrangement of two DBrDPP molecules on the Cu(110) surface.	132
6.10 STM images post 255°C anneal showing (a) a more ordered alignment of the molecules in the [001] direction, and (b) the different bonding where 3 copper atoms create a larger molecular separation (red dots) and where C-Cu-C bonds enable closer centre to centre distances to be observed	133
6.11 STM images after annealing to 300°C exhibiting differences in the macrocycle core.....	134
6.12 Schematic diagram showing a more accurate arrangement of two DBrDPP molecules on the Cu(110) surface	135
6.13 STM images after annealing to 350°C. (a) and (b), large scale and magnified images respectively	136
6.14 STM image post 400°C anneal	136
6.15 STM image showing decomposition after annealing the Cu(110) substrate to 500°C.....	137

6.16 STM image of graphene island formation on the Cu(110) substrate after annealing to 700°C.....	137
6.17 STM images showing graphene domains through subsequent magnifications	138
6.18 Magnified STM image showing the hexagonal carbon lattice structure of graphene and the corresponding FFT	139
6.19 STM images showing (a) large graphene domains, (b) and (b) magnified graphene domain to emphasise the hexagonal lattice and moiré pattern with (c) corresponding FFT and (d) observation of graphite.....	140
6.20 STM image of a graphene domain exhibiting defects in the layer	141
6.21 STM images showing (a) DBBA organo-metallic chains on the Cu(110) surface surrounded by graphene islands, (b) magnification of a graphene domain and (c) the DBBA chains exhibiting the previously observed tilting effect,.....	142
6.22 STM images of (a) and (c) exhibiting graphene and cyclodehydrogenated DBBA molecules, and respectively, (b) a magnified graphene domain, and (d) DBBA where copper ‘spacers’ are observed	143
6.23 Schematic showing the proposed orientation of DBBA molecules on the Cu(110) surface.	144
6.24 STM images of (a) the graphene domains surrounded by (b) disordered, decomposed DBBA molecules.....	145
7.1 TBrPP molecule proposed as a promising candidate for GNR integration.....	150
7.2 STM images ((a), (b), (c) and (d)) showing TBrPP covalently bonding with DBBA molecules and (e) a schematic model of the bonding configuration shown in (d).....	151
7.3 STM images showing covalent bonding between TBrPP molecules and GNRs	152

7.4 (a) 5,15-dibromo-10,20-diphenyl and (b) 5-bromo-10,15,20-triphenyl	153
7.5 (a) Proposed arrangement of DBDPP/DBBA and (b) BrTriPP/DBBA	154
7.6 Evidence of dimer formation between two BrTriPP molecules	154
7.7 Molecular building blocks, synthesised precursor molecules for GNR growth and the resultant GNRs	156
7.8 Examples of nitrogen and oxygen functionalised Graphene Nanoribbons	157

List of Abbreviations

Armchair Graphene Nanoribbons	AGNRs
5-bromo-10,15,20-triphenyl Porphyrins	BrTriPP
Dibromobianthracene	DBBA
Ni(II) 5,15-dibromo-10,20-diphenyl	DBDPP
Density Functional Theory	DFT
Fast Entry Load-lock	FEL
Field-effect transistor	FET
Fast Fourier Transform	FFT
Functionally-integrated Graphene Nanoribbons	fGNRs
Graphene Nanoribbons	GNRs
Hexabromotriphenylene	HBTP
Inelastic Mean Free Path	IMFP
Low Energy Diffraction Optics	LEED
Monolayer	ML
Near-edge X-ray Absorption Fine Structure	NEXAFS
5,10,15,20-tetrakis(4-bromo-phenyl)porphyrinato-Ni(II)	NiTBrPP
Photoelectron Spectroscopy	PES
Scanning Tunnelling Microscopy	STM
Scanning Tunnelling Spectroscopy	STS
1,3,5-tris(4-bromophenyl)benzene	TBB
Tetra(4-bromophenyl) porphyrin	TBrPP
Titanium Sublimation Pumps	TSP
Ultra High Vacuum	UHV
Variable Temperature Scanning Tunnelling Microscope	VT-STM
X-Ray Photoelectron Spectroscopy	XPS

Chapter 1

Introduction

This surface science project is an investigation of a ‘bottom up’ approach to the formation of covalently bonded nano-structures on metal surfaces. Network formation, and in particular covalently bonded networks form the basis of the work explored in this thesis. Such networks are becoming an increasingly important research topic due to the possibility for controlled architecture of bottom-up fabricated overlayers. Molecular electronics, gas sensors and protective coatings are but a few of the important applications of such covalently bonded molecular structures ^[1]. The adsorption of precursor molecules onto surfaces for the formation of covalently bonded nanonetworks for device applications has been studied extensively ^[2, 3, 4, 5, 6, 7, 8, 9].

This chapter introduces the chemical reactions investigated, self-assembly, dehalogenation, and covalent bonding resulting in the formation of molecular networks, graphene nanoribbons (GNRs) and graphene. A brief discussion of these topics is accompanied by an overview of previously published literature pertaining to each. Finally, an outline of the thesis is presented.

In 1904, Ullmann and Bielecki, discovered how copper acts as a catalyst in the coupling of iodobenzene to produce biaryls ^[10]. This reaction has become widespread in the chemical synthesis of biphenyl derivatives through dehalogenation ^[11]. The surface assisted polymerisation of molecular building blocks with specific functionalities has become a goal in the realisation of molecular electronics for device manufacture ^[2, 12]. The main obstacle to overcome is the controlled patterning of strong covalently bonded structures on surfaces from a bottom up approach, as opposed to a top down lithographic approach ^[7]. Recent work under UHV conditions has successfully demonstrated that covalent bonding, most notably through Ullmann dehalogenation reactions, can be activated through thermally induced cleaving of halogen-carbon bonds and subsequent radical addition resulting in

network formation ^[13, 14, 15]. McCarthy *et al.* ^[16] and Lipton-Duffin *et al.* ^[17] observed that iodine dissociates from diiodobenzene at room temperature when deposited on the Cu(111) and Cu(110) surfaces, enabling covalent network formation to occur between molecules. Two-dimensional organic networks on Cu(111), Ag(111) and Cu(110) using tetrathienoanthracene as the molecular precursor have been demonstrated by Gutzler *et al.* where the surface was identified as having a major influence on dehalogenation and subsequent network formation. Furthermore, organo-metallic structures are observed when tetrathienoanthracene molecules are deposited and annealed on the Cu(111) and Ag(111) surfaces ^[14].

The research presented in this thesis is specifically concerned with dissociation of bromine from organic molecules and subsequent formation of covalently bonded architectures.

Grill *et al.* ^[13] were successful in the debromination and covalent network formation of tetra(4-bromophenyl)porphyrin on the Au(111) surface held at an elevated temperature (~340°C) during deposition. Additionally, mono and di bromophenylporphyrins exhibited the same mechanisms resulting in dimers and chains respectively. Studies conducted by Park *et al.* ^[18] show the catalytic scission of Br-C bonds and formation of anthracene chains on Ag(111) at room temperature. A C-Ag-C organo-metallic bond between adjacent anthracene units was observed where dissociated bromine atoms formed Br-H bonds at hollow sites between the hybrid chains. Bombis *et al.* reported on the debromination of dibromoterfluorene on the Au(111) surface at ~250°C. They observed that the resultant poly(9,9-dimethylfluorene) chains make connections with the metal and an adsorbed NaCl island which occurs due to chain growth over the insulating islands ^[19]. This investigation in molecular architectures has also been investigated for an atomic scale nanopad as a contact for molecular wires. From a theoretical perspective, Bjork *et al.* calculated that the metal surfaces effectively reduce the barriers for C-Br scission of bromobenzene, with the largest barrier for Au(111) and smallest for Cu(111) ^[20].

To realise the goal of bringing molecular architectures to applications in device manufacturing, it is essential to understand the processes involved at the atomic scale. An ever expanding study of molecular growth dynamics based on organo-metallic bonding has recently been observed to alter the covalent bonding between molecules on surfaces. As a result of this, direct molecule to molecule bonding can be restricted by the presence of

surface atoms engaging in the bonding process. Hanke *et al.* recently demonstrated via STM and DFT calculations how non functionalised Cu-porphyrins self-assemble on Cu(110) and thereafter, by thermal activation, form C-Cu-C organo-metallic coupling between molecules in a chain and across adjacent rows ^[21]. Fan *et al.* developed this idea further by depositing 4,4-dibromo-meta-terphenyl onto the Cu(111) surface where debromination occurs at room temperature causing meta-terphenyl fragments to form exhibiting C-Cu-C bonds. They propose that Cu adatoms participate in the cleaving of the C-Br bond such that Br atom is directly replaced with the Cu atom ^[22]. Other examples of such bonding configurations have been reported for organic halogen functionalised molecules ^[23, 24, 25].

1.1 Graphene and Moiré pattern

Graphene is an atomically thick plane of graphite, is the thinnest known and strongest material measured to date and has charge carriers exhibiting high mobility due to minimal scattering effects ^[26]. Ever since its discovery, in 2004, it has become a promising candidate for molecular device applications ^[27]. Recently, high-frequency field-effect transistors (FETs) have been fabricated from graphene which exhibit faster response times when compared to silicon (GHz range) ^[28, 29]. Chen and Tao demonstrated how the electronic properties of benzene change depending on its surroundings. From a near insulating single molecule (large LUMO-HOMO gap) to a multi-benzene system such as semi-conducting PTCDI (smaller LUMO-HOMO gap) to a graphene sheet (small or zero band gap) ^[30].

Techniques for graphene fabrication include micromechanical exfoliation of bulk graphene ^[31], sublimation of Si from SiC substrates ^[32] and chemical vapour deposition ^[33]. The work presented in this thesis focuses on the bottom up approach to graphene formation from precursor building blocks. Reports to date include thermal cracking of propylene molecules on Pt, Ir and Ni resulting in an atomic layer of graphene ^[34] and similarly, the thermal decomposition and subsequent graphene formation from ethylene molecules exhibit a ‘stitching’ effect between adjacent graphene domains ^[35]. Phark *et al.* successfully decomposed C₂H₄ on Ir(111) resulting in graphene domains exhibiting a rippling effect attributed to a moiré structure ^[36]. This type of periodic structure superimposed on graphene

has been observed in numerous cases. Dedkov and Voloshina^[37] observed variations of the moiré structure as a function of the STM bias voltage when examining graphene on the Ir(111) surface. Spectroscopy maps were measured by Tapasztó *et al.* revealing evidence that the observed structural ripples (moiré patterns) in graphene on Cu(111) affect the local electronic structure of graphene which encourages one-dimensional electronic superlattices^[38]. Furthermore, Vinogradov *et al.* observed similar superstructures when investigating graphene on Fe(110), in particular, a corrugation periodicity and height of ~4 nm and ~0.06 nm respectively^[39].

1.2 Graphene Nanoribbons (GNRs)

Narrow chains of graphene, graphene nanoribbons, are a potential candidate for device manufacture due to the high carrier mobility of graphene. The advantage of GNRs over graphene is the ability to finely tune their electronic properties by lateral quantum confinement i.e. changing the width of the GNRs has a direct effect on the band gap, something which graphene lacks^[40]. Recent techniques for GNR formation have concentrated on top down methodologies such as the unzipping of carbon nanotubes as well as lithographic, micromechanical cleavage and alternative chemical techniques^[41, 42, 43, 44, 45]. This however, poses problems for integration of GNRs into current device structures due to a lack of control over the edge structure and subsequently, the fine tuning of a band gap. For this reason, extensive research into the bottom up surface assisted fabrication of GNRs using precursor building blocks has taken precedence over the top down approach. Cai *et al.* were one of the first groups to demonstrate a simple method for the formation of atomically precise GNRs. This was achieved by thermally activating dibromobianthracene molecules after room temperature deposition on the Au(111) substrate^[46]. Vo *et al.* reported similar findings on the Ag(111) surface while also observed the emergence of 14 and 21-AGNRs using dibromobianthracene as the precursor. This occurred due to cross cyclodehydrogenation between neighbouring 7-AGNRs^[47]. The first electronic characteristics of GNRs were probed by Ruffieux *et al.* who fabricated armchair GNRs (AGNRs) where scanning tunnelling spectroscopy (STS) measurements show that a band gap of 2.3eV existed for the 7-AGNR on the Au(111) surface^[48]. This

research topic is still in the early days of development. Further reading can be found in the following published material ^[49, 50, 51, 52, 53, 54].

1.3 Thesis Outline

Bromine functionalised organic molecules; their self-assembly, covalent bonding and network formation, in addition to their interaction with the substrate are investigated in this thesis. This is achieved through a dehalogenation and subsequent radical addition reaction described in the following papers by Grill *et al.* ^[13], Barth *et al.* ^[2], Walch *et al.* ^[24], Xi *et al.* ^[55], and Lipton-Duffin *et al.* ^[17]. The bonding strategy is shown in Figure 1.1. This work incorporates molecules exhibiting different numbers of bromine atoms per molecule. Furthermore, the chosen molecules range in size and chemical composition. Examination of these molecules is undertaken on the Au(111), Ag(111), Cu(111) and Cu(110) surfaces.

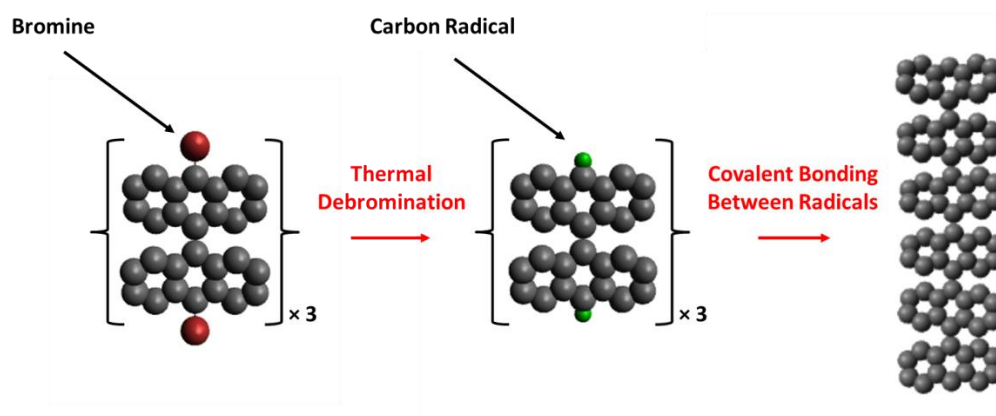


Figure 1.1: Bonding strategy for a brominated molecule (DBBA), to radical formation and subsequent covalently bonded chain. Hydrogen atoms have been omitted for clarity.

This thesis is divided into six chapters. Chapter 2 introduces the experimental apparatus and techniques used to study the molecular systems on surfaces. These include Scanning tunnelling microscopy, x-ray photoelectron spectroscopy, photoemission spectroscopy and x-ray absorption spectroscopy. The molecules and metal substrates used in experiments are also discussed.

Chapter 3 describes an investigation of hexabromotriphenylene (HBTP) on the Au(111), Ag(111) and Cu(111) surfaces. Self-assembly at room temperature and covalent bonding

are discussed, in addition to a reconstruction of dissociated bromine atoms on the Ag(111) and Cu(111) surfaces.

The extensive results for dibromobianthracene (DBBA) molecules on the Au(111), Ag(111) and Cu(111) surfaces are described and discussed in Chapter 4. Complimentary results from scanning tunnelling microscopy, photoemission and x-ray absorption measurements compared and presented. Furthermore, the formation of graphene and moiré patterns are observed and discussed.

Chapter 5 presents an STM study of DBBA molecules on Cu(110) self-assembly, debromination and subsequent bonding is discussed.

Chapter 6, investigates the deposition and subsequent bonding of DBrDPP on the Cu(110) surface. The scanning tunnelling microscopy results are presented showing covalent nanostructures, the formation of graphene and moiré superstructures within the graphene domains.

Chapter 7 provides an overall summary of the findings presented in this thesis, some preliminary results from further investigation of the systems presented here and suggestions for future experiments.

1.4 References

- [1] Bartels, L. 2010, "Tailoring molecular layers at metal surfaces", *Nature Chemistry*, vol. 2, no. 2, pp. 87-95.
- [2] Barth, J.V., Costantini, G. & Kern, K. 2005, "Engineering atomic and molecular nanostructures at surfaces", *Nature*, vol. 437, no. 7059, pp. 671-679.
- [3] BINNING, G., ROHRER, H., GERBER, C. & WEIBEL, E. 1982, "Surface Studies by Scanning Tunneling Microscopy", *Physical Review Letters*, vol. 49, no. 1, pp. 57-61.
- [4] Braunschweig, A.B., Choi, J.W., Flood, A.H., Nygaard, S., Steuerman, D.W., Laursen, B.W., Luo, Y., DeIonno, E., Peters, A.J., Jeppesen, J.O., Stoddart, J.F. & Heath, J.R. 2005, "Similarities across environments in molecular electronics", *Abstracts of Papers of the American Chemical Society*, vol. 230, pp. U3224-U3225.
- [5] El Garah, M., MacLeod, J.M. & Rosei, F. 2013, "Covalently bonded networks through surface-confined polymerization", *Surface Science*, vol. 613, pp. 6-14.
- [6] Flood, A.H., Stoddart, J.F., Steuerman, D.W. & Heath, J.R. 2004, "Whence molecular electronics?", *Science*, vol. 306, no. 5704, pp. 2055-2056.
- [7] Heath, J.R. 2003, *A systems approach to molecular electronics*.
- [8] Heath, J.R. & Ratner, M.A. 2003, "Molecular electronics", *Physics Today*, vol. 56, no. 5, pp. 43-49.
- [9] Heath, J.R., Stoddart, J.F. & Williams, R.S. 2004, "More on molecular electronics", *Science*, vol. 303, no. 5661, pp. 1136-1137.
- [10] Ullmann, F. 1904, "Ueber symmetrische biphenylderivate", *Justus Liebigs Annalen der Chemie*, vol. 332, no. 1-2, pp. 38-81.
- [11] Lin, H. & Sun, D. 2013, "Recent Synthetic Developments and Applications of the Ullmann Reaction. A Review", *Organic Preparations and Procedures International*, vol. 45, no. 5, pp. 341-394.
- [12] Joachim, C., Gimzewski, J. & Aviram, A. 2000, "Electronics using hybrid-molecular and mono-molecular devices", *Nature*, vol. 408, no. 6812, pp. 541-548.
- [13] Grill, L., Dyer, M., Lafferentz, L., Persson, M., Peters, M.V. & Hecht, S. 2007, "Nano-architectures by covalent assembly of molecular building blocks", *Nature Nanotechnology*, vol. 2, no. 11, pp. 687-691.

- [14]Gutzler, R., Cardenas, L., Lipton-Duffin, J., El Garah, M., Dinca, L.E., Szakacs, C.E., Fu, C., Gallagher, M., Vondracek, M., Rybachuk, M., Perepichka, D.F. & Rosei, F. 2014, "Ullmann-type coupling of brominated tetrathienoanthracene on copper and silver", *Nanoscale*, vol. 6, no. 5, pp. 2660-2668.
- [15]Grill, L. 2008, "Functionalized molecules studied by STM: motion, switching and reactivity", *Journal of Physics-Condensed Matter*, vol. 20, no. 5, pp. 053001.
- [16]McCarty, G.S. & Weiss, P.S. 2002, "Footprints of a surface chemical reaction: Dissociative chemisorption of p-diiodobenzene on Cu{111}", *Journal of Physical Chemistry B*, vol. 106, no. 33, pp. 8005-8008.
- [17]Lipton-Duffin, J.A., Ivasenko, O., Perepichka, D.F. & Rosei, F. 2009, "Synthesis of Polyphenylene Molecular Wires by Surface-Confined Polymerization", *Small*, vol. 5, no. 5, pp. 592-597.
- [18]Park, J., Kim, K.Y., Chung, K., Yoon, J.K., Kim, H., Han, S. & Kahng, S. 2011, "Interchain Interactions Mediated by Br Adsorbates in Arrays of Metal-Organic Hybrid Chains on Ag(111)", *Journal of Physical Chemistry C*, vol. 115, no. 30, pp. 14834-14838.
- [19]Bombis, C., Ample, F., Lafferentz, L., Yu, H., Hecht, S., Joachim, C. & Grill, L. 2009, "Single Molecular Wires Connecting Metallic and Insulating Surface Areas", *Angewandte Chemie-International Edition*, vol. 48, no. 52, pp. 9966-9970.
- [20]Bjork, J., Hanke, F. & Stafstrom, S. 2013, "Mechanisms of Halogen-Based Covalent Self-Assembly on Metal Surfaces", *Journal of the American Chemical Society*, vol. 135, no. 15, pp. 5768-5775.
- [21]Hanke, F., Haq, S., Raval, R. & Persson, M. 2011, "Heat-to-Connect: Surface Commensurability Directs Organometallic One-Dimensional Self-Assembly", *Acs Nano*, vol. 5, no. 11, pp. 9093-9103.
- [22]Fan, Q., Wang, C., Han, Y., Zhu, J., Kuttner, J., Hilt, G. & Gottfried, J.M. 2014, "Surface-Assisted Formation, Assembly, and Dynamics of Planar Organometallic Macrocycles and Zigzag Shaped Polymer Chains with C-Cu-C Bonds", *Acs Nano*, vol. 8, no. 1, pp. 709-718.
- [23]Walch, H., Dienstmaier, J., Eder, G., Gutzler, R., Schloegl, S., Sirtl, T., Das, K., Schmittel, M. & Lackinger, M. 2011, "Extended Two-Dimensional Metal-Organic Frameworks Based on Thiolate-Copper Coordination Bonds", *Journal of the American Chemical Society*, vol. 133, no. 20, pp. 7909-7915.
- [24]Walch, H., Gutzler, R., Sirtl, T., Eder, G. & Lackinger, M. 2010, "Material- and Orientation-Dependent Reactivity for Heterogeneously Catalyzed Carbon-Bromine

- Bond Homolysis", *Journal of Physical Chemistry C*, vol. 114, no. 29, pp. 12604-12609.
- [25]Gutzler, R., Walch, H., Eder, G., Kloft, S., Heckl, W.M. & Lackinger, M. 2009, "Surface mediated synthesis of 2D covalent organic frameworks: 1,3,5-tris(4-bromophenyl)benzene on graphite(001), Cu(111), and Ag(110)", *Chemical Communications*, , no. 29, pp. 4456-4458.
- [26]Geim, A.K. 2009, "Graphene: Status and Prospects", *Science*, vol. 324, no. 5934, pp. 1530-1534.
- [27]Novoselov, K.S., Geim, A.K., Morozov, S.V., Jiang, D., Zhang, Y., Dubonos, S.V., Grigorieva, I.V. & Firsov, A.A. 2004, "Electric field effect in atomically thin carbon films", *Science*, vol. 306, no. 5696, pp. 666-669.
- [28]Jenkins, K.A., Lin, Y.-., Farmer, D., Dimitrakopoulos, C., Chiu, H.-., Valdes-Garcia, A., Avouris, P. & Grill, A. 2010, "Graphene RF Transistor Performance", *Graphene, Ge/iii-V, and Emerging Materials for Post-Cmos Applications 2*, vol. 28, no. 5, pp. 3-13.
- [29]Lin, Y.-., Dimitrakopoulos, C., Jenkins, K.A., Farmer, D.B., Chiu, H.-., Grill, A. & Avouris, P. 2010, "100-GHz Transistors from Wafer-Scale Epitaxial Graphene", *Science*, vol. 327, no. 5966, pp. 662-662.
- [30]Chen, F. & Tao, N.J. 2009, "Electron Transport in Single Molecules: From Benzene to Graphene", *Accounts of Chemical Research*, vol. 42, no. 3, pp. 429-438.
- [31]Zhang, Y.B., Tan, Y.W., Stormer, H.L. & Kim, P. 2005, "Experimental observation of the quantum Hall effect and Berry's phase in graphene", *Nature*, vol. 438, no. 7065, pp. 201-204.
- [32]Berger, C., Song, Z., Li, X., Wu, X., Brown, N., Naud, C., Mayou, D., Li, T., Hass, J., Marchenkov, A.N., Conrad, E.H., First, P.N. & de Heer, W.A. 2006, "Electronic confinement and coherence in patterned epitaxial graphene", *Science*, vol. 312, no. 5777, pp. 1191-1196.
- [33]Kim, K.S., Zhao, Y., Jang, H., Lee, S.Y., Kim, J.M., Kim, K.S., Ahn, J., Kim, P., Choi, J. & Hong, B.H. 2009, "Large-scale pattern growth of graphene films for stretchable transparent electrodes", *Nature*, vol. 457, no. 7230, pp. 706-710.
- [34]Ng, M.L., Balog, R., Hornekaer, L., Preobrajenski, A.B., Vinogradov, N.A., Martensson, N. & Schulte, K. 2010, "Controlling Hydrogenation of Graphene on Transition Metals", *Journal of Physical Chemistry C*, vol. 114, no. 43, pp. 18559-18565.

- [35]Gao, L., Guest, J.R. & Guisinger, N.P. 2010, "Epitaxial Graphene on Cu(111)", *Nano Letters*, vol. 10, no. 9, pp. 3512-3516.
- [36]Phark, S., Borme, J., Vanegas, A.L., Corbetta, M., Sander, D. & Kirschner, J. 2011, "Direct Observation of Electron Confinement in Epitaxial Graphene Nanoislands", *Acc Nano*, vol. 5, no. 10, pp. 8162-8166.
- [37]Dedkov, Y. & Voloshina, E. 2014, "Multichannel scanning probe microscopy and spectroscopy of graphene moire structures", *Physical Chemistry Chemical Physics*, vol. 16, no. 9, pp. 3894-3908.
- [38]Tapaszto, L., Dumitrica, T., Kim, S.J., Nemes-Incze, P., Hwang, C. & Biro, L.P. 2012, "Breakdown of continuum mechanics for nanometre-wavelength rippling of graphene", *Nature Physics*, vol. 8, no. 10, pp. 739-742.
- [39]Vinogradov, N.A., Zakharov, A.A., Kocevski, V., Rusz, J., Simonov, K.A., Eriksson, O., Mikkelsen, A., Lundgren, E., Vinogradov, A.S., Martensson, N. & Preobrajenski, A.B. 2012, "Formation and Structure of Graphene Waves on Fe(110)", *Physical Review Letters*, vol. 109, no. 2, pp. 026101.
- [40]Han, M.Y., Oezylmaz, B., Zhang, Y. & Kim, P. 2007, "Energy band-gap engineering of graphene nanoribbons", *Physical Review Letters*, vol. 98, no. 20, pp. 206805.
- [41]Kosynkin, D.V., Higginbotham, A.L., Sinitskii, A., Lomeda, J.R., Dimiev, A., Price, B.K. & Tour, J.M. 2009, "Longitudinal unzipping of carbon nanotubes to form graphene nanoribbons", *Nature*, vol. 458, no. 7240, pp. 872-U5.
- [42]Chen, Z., Lin, Y., Rooks, M.J. & Avouris, P. 2007, "Graphene nano-ribbon electronics", *Physica E-Low-Dimensional Systems & Nanostructures*, vol. 40, no. 2, pp. 228-232.
- [43]Jiao, L., Zhang, L., Wang, X., Diankov, G. & Dai, H. 2009, "Narrow graphene nanoribbons from carbon nanotubes", *Nature*, vol. 458, no. 7240, pp. 877-880.
- [44]Datta, S.S., Strachan, D.R., Khamis, S.M. & Johnson, A.T.C. 2008, "Crystallographic etching of few-layer graphene", *Nano Letters*, vol. 8, no. 7, pp. 1912-1915.
- [45]Campos-Delgado, J., Romo-Herrera, J.M., Jia, X., Cullen, D.A., Muramatsu, H., Kim, Y.A., Hayashi, T., Ren, Z., Smith, D.J., Okuno, Y., Ohba, T., Kanoh, H., Kaneko, K., Endo, M., Terrones, H., Dresselhaus, M.S. & Terrones, M. 2008, "Bulk production of a new form of sp(2) carbon: Crystalline graphene nanoribbons", *Nano Letters*, vol. 8, no. 9, pp. 2773-2778.
- [46]Cai, J., Ruffieux, P., Jaafar, R., Bieri, M., Braun, T., Blankenburg, S., Muoth, M., Seitsonen, A.P., Saleh, M., Feng, X., Muellen, K. & Fasel, R. 2010, "Atomically

- precise bottom-up fabrication of graphene nanoribbons", *Nature*, vol. 466, no. 7305, pp. 470-473.
- [47]Vo, T.H., Shekhirev, M., Kunkel, D.A., Morton, M.D., Berglund, E., Kong, L., Wilson, P.M., Dowben, P.A., Enders, A. & Sinitskii, A. 2014, "Large-scale solution synthesis of narrow graphene nanoribbons", *Nature Communications*, vol. 5, pp. 3189.
- [48]Ruffieux, P., Cai, J., Plumb, N.C., Patthey, L., Prezzi, D., Ferretti, A., Molinari, E., Feng, X., Muellen, K., Pignedoli, C.A. & Fasel, R. 2012, "Electronic Structure of Atomically Precise Graphene Nanoribbons", *Acs Nano*, vol. 6, no. 8, pp. 6930-6935.
- [49]Son, Y., Cohen, M.L. & Louie, S.G. 2006, "Half-metallic graphene nanoribbons", *Nature*, vol. 444, no. 7117, pp. 347-349.
- [50]Stampfer, C., Schurtenberger, E., Molitor, F., Guettinger, J., Ihn, T. & Ensslin, K. 2008, "Tunable graphene single electron transistor", *Nano Letters*, vol. 8, no. 8, pp. 2378-2383.
- [51]Tan, Y., Yang, B., Parvez, K., Narita, A., Osella, S., Beljonne, D., Feng, X. & Muellen, K. 2013, "Atomically precise edge chlorination of nanographenes and its application in graphene nanoribbons", *Nature Communications*, vol. 4, pp. 2646.
- [52]Nakada, K., Fujita, M., Dresselhaus, G. & Dresselhaus, M.S. 1996, "Edge state in graphene ribbons: Nanometer size effect and edge shape dependence", *Physical Review B*, vol. 54, no. 24, pp. 17954-17961.
- [53]Wakabayashi, K. 2001, "Electronic transport properties of nanographite ribbon junctions", *Physical Review B*, vol. 64, no. 12, pp. 125428.
- [54]Yang, L., Park, C., Son, Y., Cohen, M.L. & Louie, S.G. 2007, "Quasiparticle energies and band gaps in graphene nanoribbons.", *Physical Review Letters*, vol. 99, no. 18, pp. 186801-186801.
- [55]Xi, M. & Bent, B.E. 1993, "Mechanisms of the Ullmann Coupling Reaction in Adsorbed Monolayers", *Journal of the American Chemical Society*, vol. 115, no. 16, pp. 7426-7433.

Chapter 2

Theory and Experimental Details

This chapter introduces and describes the experimental techniques used in this research project. The molecules and metal surfaces utilised and ultra-high vacuum conditions under which all experiments were conducted are discussed.

2.1 Omicron Ultra High Vacuum (UHV)

Figure 2.1 shows a schematic diagram of the Omicron UHV system which consists of three interconnected vacuum chambers; (1) analysis chamber; (2) preparation chamber and (3) STM chamber. The analysis chamber houses a sample manipulator (11) with both direct and resistive heating; an Omicron low energy electron diffraction optics (LEED) (B); a DAR 400 twin-anode X-ray source; an EA 125 hemispherical electron energy analyser and an Omicron Variable Temperature Scanning Tunnelling Microscope (VT-STM). The preparation chamber is equipped with a sample manipulator (11) equipped with resistive heating, three ports for evaporation cells used for molecular deposition and an Omicron ISE5 Argon Ion Gun for sample cleaning. Ion pumps, not shown in Figure 2.1, are enclosed in the bench assembly (5) of the UHV system and titanium sublimation pumps (TSP) (10) are present in both the analysis and preparation chamber and keep the base pressure $<10^{-10}$ mbar. Manual gate valves (7) provide isolation between the analysis and preparation chamber, and between the fast entry load-lock (FEL) (4) and preparation chamber. The fast entry load lock allows for rapid transfer of samples and STM tips without the need for venting the system. Low pressures are maintained by a turbo molecular pump (9) which can pump either the preparation and analysis chambers or the load-lock through backing lines which may be isolated by an all metal valve (8) and a pneumatic gate valve (6). All moveable components, including magnetic transfer rod (13) and wobble stick (12), are shown in purple in Figure 2.1 and permit transfer through the system from the FEL to the STM.

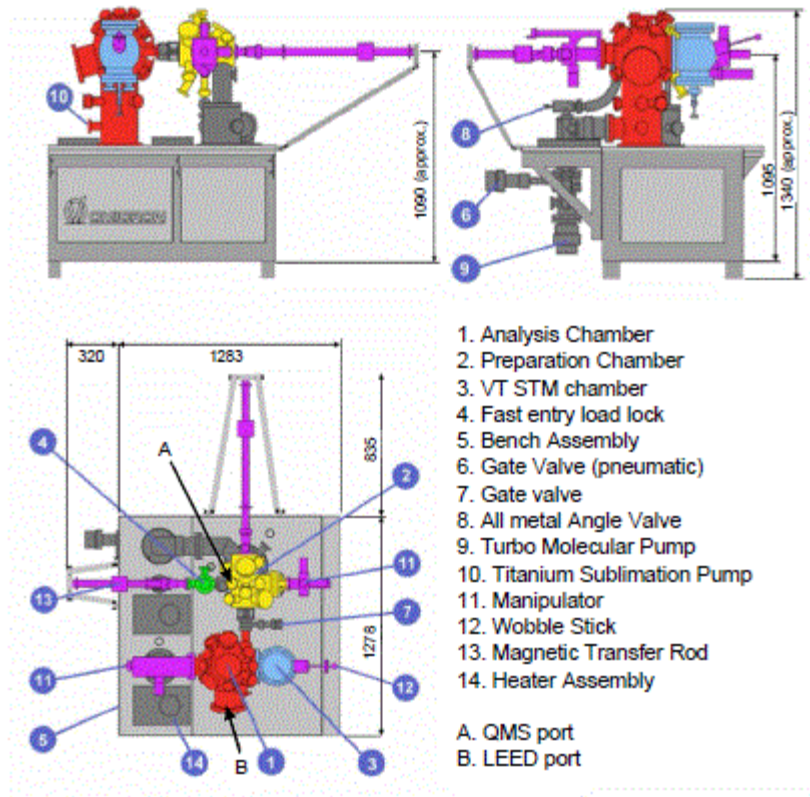


Figure 2.1: Omicron UHV system; side and top view.

2.2 Scanning Tunnelling Microscopy

2.2.1 Introduction

In the early 1980s, Gerd Binnig and Heinrich Rohrer developed the concept of the STM and successfully acquired topographic pictures of surfaces with atomic scale resolution for the first time ^[1]. This explorative and powerful technique relies on the phenomenon of quantum mechanical tunnelling which allows electrons to tunnel between a metal tip and a conductive surface (or vice versa) when a bias voltage is present in a non-contact vacuum environment i.e. a vacuum gap. When the tip and sample are separated by a distance on the order of a few Ångstroms, quantum mechanical tunnelling occurs either to filled or empty electronic states, depending on the chosen bias. It is important to minimise external mechanical vibrations when attempting to achieve atomic resolution. The main components of the STM include a sample stage and STM tip which is mounted on top of the piezo

electric tube scanner. The STM is isolated from the main chamber by a metal spring suspension system and an eddy-current dampening system to reduce vibrational interference. Further elimination of vibrations can be achieved through mounting the UHV system on viscoelastic pads.

Scanning the tip within a few Ångströms of the surface by applying small voltages to the piezo tube scanner, allows a topographical representation of the surface electron density to be recorded. This is achieved by measuring the amplified tunnel current at specific locations on the conductive surface. The tunnel current depends exponentially on the vacuum gap. In the most common scanning mode, (constant current mode), the height of the piezo-electric tube scanner responds depending on the feedback loop set point ^[2]. (Figure 2.2).

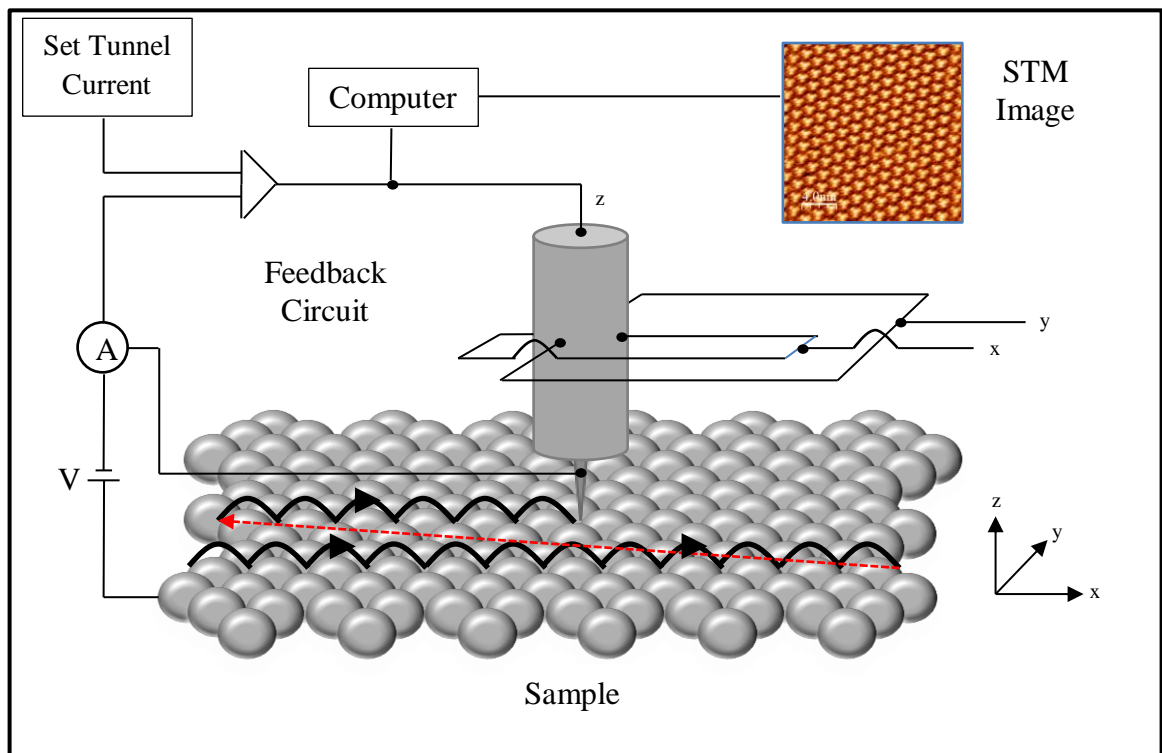


Figure 2.2: Schematic diagram showing the STM and its components.

2.2.2 Theory of STM

In order for quantum tunnelling to occur, the following conditions must hold: the tip and sample must be within ~ 1 nm of one another; the bias voltage must be such that empty states exist for electrons to tunnel into or filled states exist from which electrons can originate from; a finite barrier is present which the electrons can tunnel through.

If we consider an electron with mass m and energy E , experiencing a potential $U(z)$, then it can be described by the Schrödinger equation which requires that the wavefunction, $\Psi(z)$, of the electron satisfies the following equation:

$$-\frac{\hbar^2}{2m} \frac{d^2}{dz^2} \Psi(z) + U(z)\Psi(z) = E\Psi(z) \quad 2.1$$

where $\hbar = h/2\pi$ and h is Planck's constant ^[2].

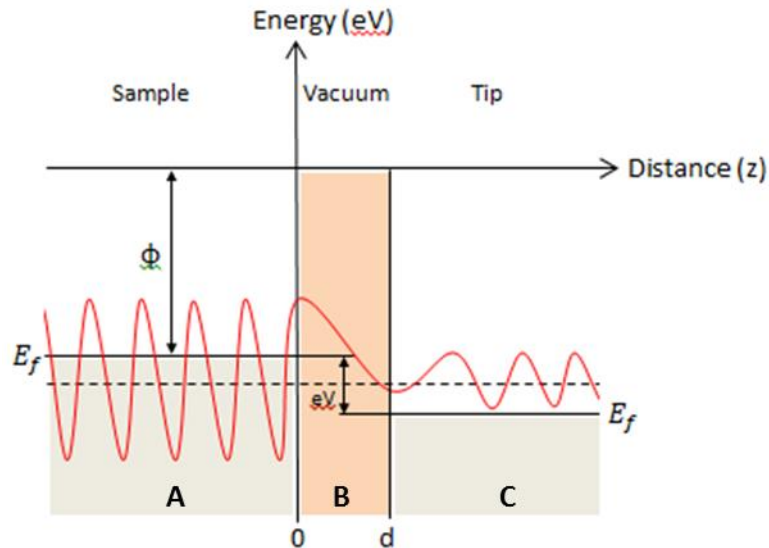


Figure 2.3: Schematic diagram of a sample in close proximity to a tip where a bias is induced enabling quantum tunnelling to occur. This bias creates a shift in the Fermi level of the tip, effectively increasing the work function (Φ).

The vacuum gap acts as a potential barrier between the tip and the sample (see Figure 2.3). In regions A, B and C, the solution to the Schrödinger equation is

$$\Psi_A(z) = A_1 e^{ik_1 z} + A'_1 e^{-ik_1 z} \quad 2.2$$

$$\Psi_B(z) = A_2 e^{ik_2 z} + A'_2 e^{-ik_2 z} \quad 2.3$$

$$\Psi_C(z) = A_3 e^{ik_3 z} \quad 2.4$$

where

$$k_1 = \frac{\sqrt{2mE}}{\hbar}, \quad k_2 = \frac{\sqrt{2m(U-E)}}{\hbar} \quad \text{and} \quad k_3 = \frac{\sqrt{2m(E \pm eV)}}{\hbar}$$

k_1 and k_3 are the wave vectors in regions A and C respectively and k_2 is the inverse decay length in region B. Figure 2.3 implies an exponential decay and it can be assumed that the work functions of both tip and sample are equal before a bias is applied. At the boundaries between regions A, B and C, the total wavefunctions and its derivatives are continuous. This yields four conditions to solve for the unknown wavefunction amplitudes, A_1 , A_2 , A'_1 , A'_2 and A_3 . One prefactor remains indeterminate. By applying a potential bias, appropriate boundary conditions, a finite potential (vacuum gap) and separation between tip and sample, d , then the transmission coefficient T , can be approximated by

$$T = \left| \frac{A_3}{A_1} \right|^2 = 16 \left(\frac{E}{U(z)} \right) \left(1 - \frac{E}{U(z)} \right) e^{-2k_2 d} \quad 2.5$$

Since the tunnel current is directly proportional to the transmission coefficient which is dominated by the exponential term, then

$$I \propto e^{-2k_2 d} \quad 2.6$$

If d decreases by 0.1 nm, the tunnel current increases by approximately one order of magnitude [3, 4, 5, 6]. This extreme sensitivity enables the STM to produce atomically resolvable images of surfaces.

The work function of the tip and sample are assumed to be equal where the magnitude dictates the height of the potential barrier. If the vacuum level is taken as 0 eV (see Figure 2.3) then the Fermi energy, $E_f = -\phi$. When a bias voltage is applied this creates an offset in the Fermi energy of tip and sample. For small bias voltages only electrons close to the Fermi energy are involved in the tunnelling process. The probability of an electron taking part in quantum tunnelling through a barrier of width d is

$$P \propto |\Psi(0)|^2 e^{-2\kappa d} \quad 2.7$$

where

$$\kappa = \frac{\sqrt{2m\phi}}{\hbar}$$

is the inverse decay length for all tunnelling electrons and $\Psi(0)$ is the wavefunction evaluated at $d = 0$. The tunnelling current is directly proportional to the probability of electrons tunnelling through the potential barrier. By summing over all possible electron states in the allowed range, $E_f - eV \leq E \leq E_f$, the tunnel current can be expressed as

$$I_t \propto \sum_{E_n}^E \rho_s(E_f + \frac{eV}{2}) |\Psi(0)|^2 \rho_t(E_f + \frac{eV}{2}) e^{-2\kappa d} \quad 2.8$$

Where ρ_s and ρ_t are the density of states of the sample and tip respectively.

2.2.3 STM Tip Preparation

Tip preparation is of vital importance in order to achieve high resolution STM imaging. The geometry of the tip has a huge bearing on the quality of the STM image and in the absence of a sharp, clean, symmetrical atomically sharp tip, false imaging is inevitable^[7, 8]. In the case of these experiments a physicochemical approach to tip manufacture was employed in preference to mechanical procedures such as cutting or machining metal wires^[8, 9]. An Omicron electrochemical tip etching kit was utilised to prepare tips for all of the STM imaging described in this work^[10].

A 5 molar concentration of sodium hydroxide was used as the etching solvent. Tungsten wire, approximately 7 mm in length, with diameter of 0.25 mm was slowly etched at the meniscus of the NaOH solution by applying 6 V between the submerged part of the wire and a circular stainless steel electrode. Once the etching process completes, and the immersed portion of the wire (~2 mm) breaks off, the remaining wire, which will eventually act as the STM tip, is cleaned in deionised water and ethanol baths before drying with nitrogen gas. The tip was then mounted onto an Omicron tip holder and transferred into the UHV chamber through the fast entry load lock. A more thorough cleaning process was carried out in the STM by applying a high electric field between the tip and surface in conjunction with the nanostructuring features in the Omicron SCALA PRO 5.0 software such as high voltage pulsing ^[11]. This tip cleaning procedure was required to remove residual NaOH resulting from the etching process, the oxide layer that forms on the tip due to exposure to air and additional contaminants picked up by the tip in air.

2.2.4 STM Data Analysis

All STM images were recorded at room temperature. The STM images, line profiles and Fast Fourier Transform (FFT) filtered images were analysed and processed using the WSxM software package ^[12]. Plane subtraction and contrast manipulation were used to visually enhance the STM images. The line profile tool can produce a 1D cross section of the 2D STM image and is mostly used to determine protrusions and depressions in the surface as well as lengths and widths of features.

The FFT tool produces a Fourier transform filtered image (which represents the reciprocal space of surface structures) allowing the line profile tool to be used for further analysis purposes on these new images. These new images, in conjunction with analysis tools in the WSxM software package allow measurements of periodicities in STM images to be calculated accurately ^[13].

2.3 Photoelectron Spectroscopy

2.3.1 X-Ray Photoelectron Spectroscopy

Photoelectron Spectroscopy, (PES), and in particular, X-ray photoelectron spectroscopy, (XPS), is an important tool for investigating the chemical composition of matter. These techniques rely upon the interaction of light and matter. Photons of known energy impinge on a sample and eject photoelectrons. The kinetic energies of the photoelectrons are measured by the hemispherical analyser. From knowledge of the kinetic energies, the binding energies of the electrons can be determined. This is the photoelectric effect in its simplest form and is described by:

$$E_K = h\nu - E_b - \phi \quad 2.9$$

Where E_K is the kinetic energy of the ejected photoelectron, $h\nu$ is the energy of the incident photon, E_b is the binding energy of the electron and ϕ is the work function of the surface which relates the vacuum level to the Fermi level of a solid. An incident photon will only eject a photoelectron if $h\nu > (E_b + \phi)$ rendering the excess energy of the photon as the kinetic energy of the emitted electron. A schematic diagram showing the principle of the photoelectron effect is shown in Figure 2.4.

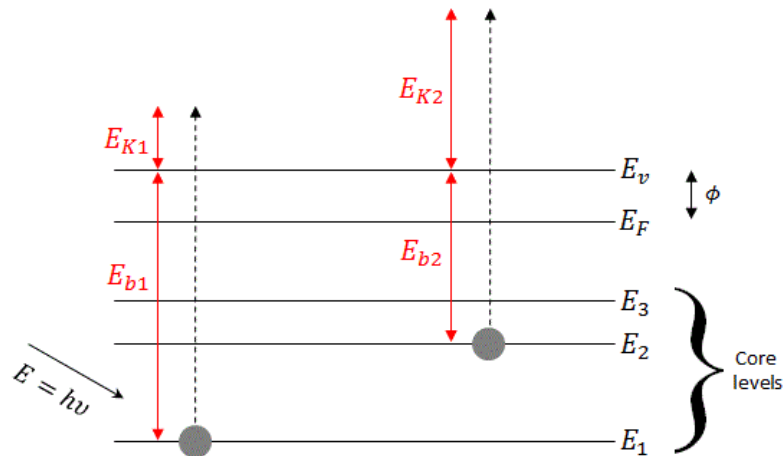


Figure 2.4: Representation of the interaction of a photon with energy $h\nu$ and core level electrons bound by E_b . Subsequent ejection results in electrons with kinetic energy, E_K .

Equation 2.9 relies upon the assumption that there is no electron rearrangement in the sample upon photoelectron ejection. However, the simplified model will suffice for analysis of the experimental data presented in this thesis. In this simple model the photoelectron process can be described by a three step model:

1. Excitation of an electron in a solid by an incident photon
2. Migration of photoelectron to the surface
3. Electron ejection from the solid to the vacuum

Fermi's Golden Rule provides a general and widely applied theoretical description of the photoemission process where photoexcitation of a core electron exhibits a transition probability given by

$$w_{fi} = \frac{2\pi}{\hbar} |\langle \Psi_f, K_f | H^{int} | \Psi_i, K_i \rangle|^2 \delta(E_f - E_i - h\nu) \quad 2.10$$

Where Ψ_i and E_i are the wave function and the energy of the initial multi-electron system and Ψ_f and E_f refer to the wave function and energy of the final state, respectively. K_i is the wave vector of the electron bound in its initial state and K_f is the wave vector of the photoelectron in its final state inside the solid under investigation. The perturbation Hamiltonian, H^{int} , describes the interaction of an electron with the electromagnetic field of a photon and is given by

$$H^{int} = \frac{e}{mc} A \cdot \hat{p} \quad 2.11$$

where \hat{p} is the momentum operator of the electron and A is the vector potential of the electromagnetic field.

As the excited electron propagates towards the surface, energy is lost via scattering and interactions with other electrons in the solid. The distance the electron travels before experiencing any reduction in energy is called the mean free path, denoted λ . Since electron-phonon interactions are only significant at low electron energies, the energy loss

contribution comes mostly from electron-electron interactions. Thus, the mean free path is a function of the excitation energy E and wave vector k , which is related to the scattering lifetime τ and electron velocity in the final state v

$$\lambda(E, k) = \tau v \quad 2.12$$

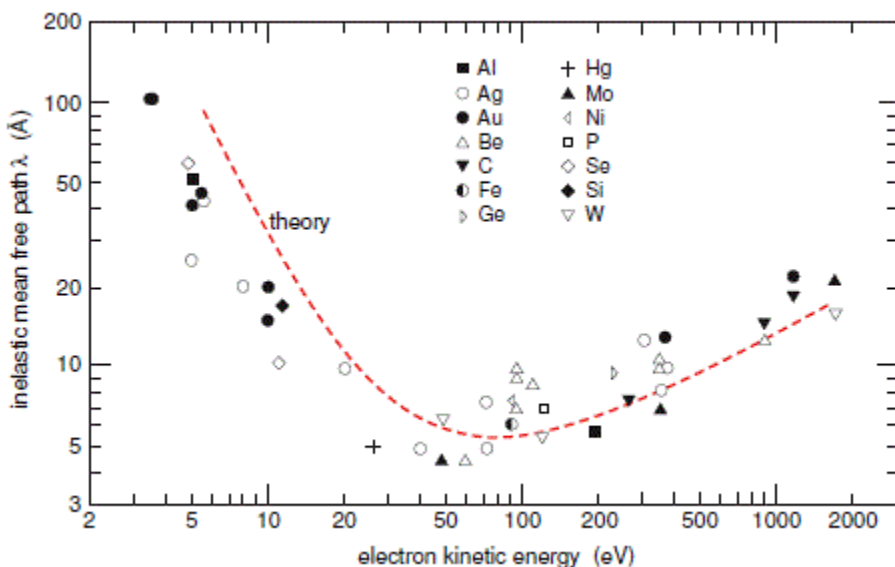


Figure 2.5: Electron mean free path curve. The dashed line indicates the theoretical predictions while the symbols represent experimentally obtained values for different elements. Taken from *Handbook of Vacuum Science and Technology* [14].

Figure 2.5 displays the mean free path of photoelectrons within a solid due to scattering effects, which are predominantly due to electron-electron interactions. Low energy electrons ($<10\text{eV}$) do not have sufficient energy to effectively interact within the solid and are therefore able to propagate through greater distances equating to a high probability of electrons being ejected; this probability is related to the photoionisation cross-section. Similarly, high energy electrons ($>200\text{eV}$) have low cross-sections and are able to travel larger distances without scattering effects. Electrons with energy ranging from 30eV to 200eV are more susceptible to interaction with other electrons due to the high cross-section and hence they exhibit a short inelastic mean free path (IMFP). Thus the electrons which escape the solid come from a short escape depth of approximately 1.5 nm [3, 6, 15]. XPS measurements must be performed in UHV ($<10^{-9}\text{mbar}$) to eliminate or minimise scattering

effects due to residual gas atoms as the electrons travel from the surface of the solid to the analyser. These low pressures also ensure the sample surface retains its cleanliness for the duration of experiments. Inelastic scattering phenomenon inside the solid, such as plasmon coupling and electron-electron interaction, contribute to a low energy background spectrum in XPS measurements. Furthermore, photoelectron interaction with other bound electrons, promoting them to higher energy states or states above the vacuum level create spectral features such as discrete shake-up satellite peaks and broader shake-off peaks^[3]. These peaks are also present in the background measurements.

The third step in the model involves electrons ejected from the solid surface into the vacuum. In order for this to occur, they must overcome the potential barrier between the highest occupied molecular orbital in the solid, and the vacuum level where $eV_0 = E_v - E_0$; V_0 being the surface potential and E_0 the energy of the highest occupied atomic orbital.

XPS studies described in this thesis used a twin anode (Mg/Al) x-ray source (Figure 2.6). The Mg and Al anodes are most commonly used because the x-ray emission for each element has two intense yet unresolved emission lines produced by the $2p_{1/2} \rightarrow 1s$ and $2p_{3/2} \rightarrow 1s$ transitions ($K_{\alpha 1,2}$) where the $K_{\alpha 1}$ dominates^[3]. The $K_{\alpha 1,2}$ spectral lines have certain widths respectively for each element and together with their separation, determine the ultimate resolution of approximately 1eV. There are additional weak spectral lines which contribute to peaks in the XPS. These are removed by a monochromator leading to enhanced resolution. Electrons produced by thermionic emission from a filament are accelerated towards the anode which is held at a potential of 14kV. These electrons can excite bound electrons in the Mg or Al anode resulting in the creation of a core hole. This in turn leads to an electron filling the vacant state with the emission of an x-ray photon. The emission lines for Mg and Al produce x-ray photons with energies of 1253.6eV and 1486.7eV respectively.

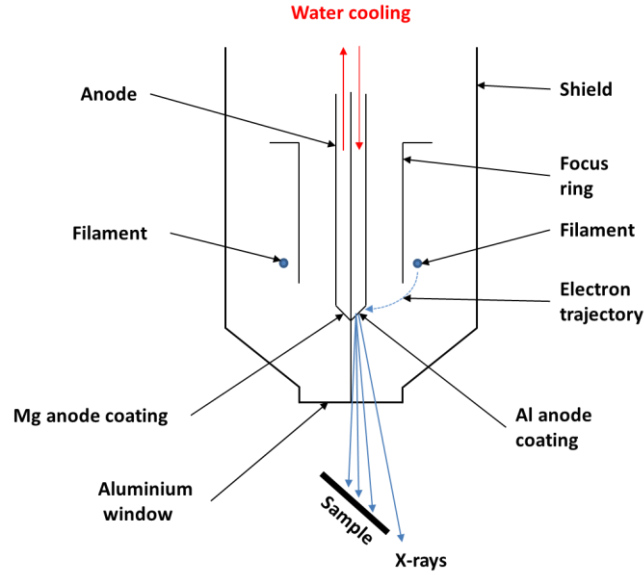


Figure 2.6: Schematic of a Mg/Al twin anode x-ray source.

A hemispherical electron analyser, shown schematically in Figure 2.7, measures the kinetic energy of the photoelectrons ejected from the sample. It consists of inner and outer hemispheres of radii r_1 and r_2 , biased positively and negatively respectively to help focus electrons towards the detector.

The condition for an electron to ‘pass’ through the analyser to the detection stage is determined by the pass energy, E_p .

$$E_p = \frac{eV}{\left(\frac{r_2}{r_1} - \frac{r_1}{r_2}\right)} \quad 2.13$$

Where, V is the potential difference between the hemispheres. The energy resolution, ΔE of the analyser depends on the energy uncertainty in the sample, analyser and Lorentzian broadening of the x-ray source and is given by

$$\Delta E = E_p \left(\frac{d}{2r_0} + \alpha^2 \right) \quad 2.14$$

where d is the width of the entrance slit, α the acceptance angle and the central radius $r_0 = (r_1 + r_2)/2$ (see Figure 2.7). The lens stack acts as a focussing and decelerating tool allowing the highest possible electron yield, with the correct pass energy, to reach the entrance slit of the analyser. If the energy of the electron is too high or too low, it will collide with either the outer or inner hemisphere respectively. Only electrons with the correct pass energy will reach the detector.

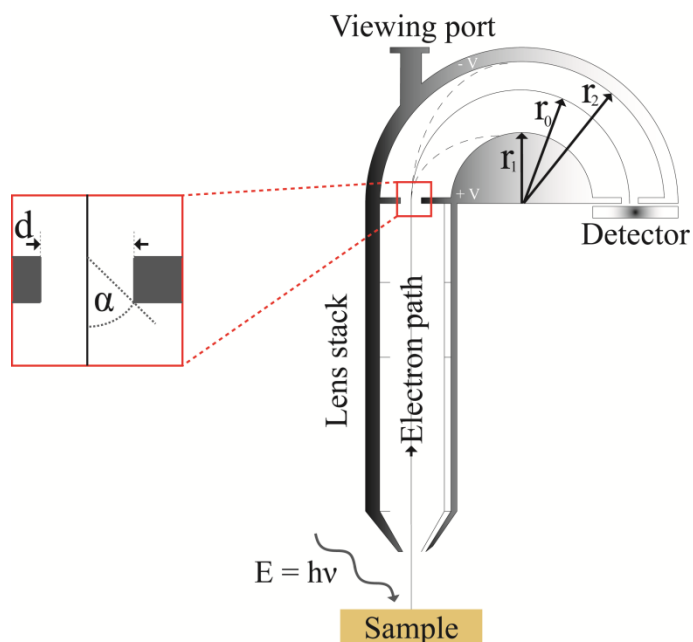


Figure 2.7: Hemispherical analyser showing electron path from sample to detector. Dashed lines represent the electron paths which have $E_k \neq E_p$.

2.3.2 XPS Data Analysis

The XPS system comprises an Omicron DAR 400 Mg/Al twin anode X-ray source and an Omicron EA 125 Hemispherical Energy Analyser. The analyser is equipped with a five channeltron array of detectors with amplification capabilities in the $10^7 - 10^8$ range. An Omicron 554-S X-ray Source Control Package software was used to control the X-ray source. The spectra were acquired using the Omicron EIS/EIS Sphera software^[16]. An Origin 8.0 software package allows spectra background subtraction (e.g. linear, Shirley) where the spectra can be normalised to the number of scans if necessary^[17]. The spectra are fitted with Gaussian or Voigt line-shapes where appropriate (A Voigt line-shape being a convolution of a Gaussian and a Lorentzian). This is conducted via Aanalyzer, Fityk and

FitXPS peak fitting software. Molecular coverage can be approximated from STM images and XPS spectra where ratios of C 1s peaks to an appropriate substrate peak are determined, e.g. the C 1s peak relative to the Au 4d peak.

2.3.3 Synchrotron Radiation

Synchrotron based photoelectron spectroscopy (PES) is used, to provide an insight into the chemical composition of matter. The advantages of PES over XPS are its tuneable photon energy, high intensity, variable polarisation and small spot size.

To produce this wide range of photon energies, electrons are accelerated at velocities close to the speed of light around a storage ring. This is achieved using undulators and dipole magnets which steer the electrons and allow focussing. When the vector path changes, electromagnetic radiation ranging from radio to hard x-rays waves are emitted and photons of the appropriate wavelength can be selectively chosen and utilised at an experimental station. A monochromator allows selection of a photon wavelength and filters enable linearly polarised light to then be manipulated for experimental purposes. The synchrotron radiation experiments described in this thesis were carried out on the D1011 beamline at the MAX-II storage ring in Lund, Sweden. The D1011 beamline station comprises of an upper chamber for sample preparation, equipped with an argon ion sputter gun, LEED system, fast entry load lock, thermal evaporation molecular deposition ports and an adjoining lower chamber for PES and NEXAFS experiments. The analysis chamber, where the photons enter from the main beamline, contains a concentric hemispherical electron analyser (VG Scienta SES200) and a microchannel plate detector for electron yield detection whilst conducting XAS measurements (discussed below). The manipulator which can pass from the upper to lower chamber, allows for sample transfer, heating and orientation. Photon energies between 40eV and 1500eV with resolving power (E/dE) of 1.5×10^3 to 1.3×10^4 and photon flux at the sample of 10^{10} to 10^{11} photons/s/100mA are available on the D1011 beamline.

2.3.4 PES Data Analysis

The spectra obtained in MAX-lab were background subtracted and peak fitted using FitXPS. They were normalised to the beam current and the binding energies were corrected using the Fermi level measured from the metallic substrate. Pictures of the D1011 beamline apparatus are shown in Figure 2.8.

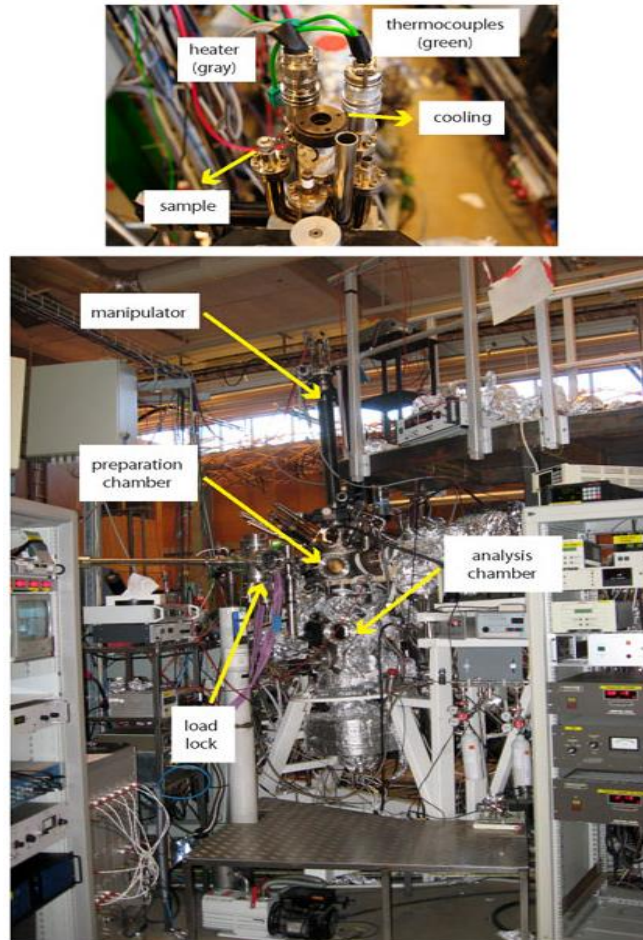


Figure 2.8: Experimental stations at synchrotron radiation facility. D1011 beamline, MAX-lab, Lund University, Sweden.

2.3.5 X-ray Absorption Spectroscopy

X-ray absorption spectroscopy is an important and powerful technique for investigation and characterisation of matter using synchrotron radiation. X-rays of varying energies are used to probe the unoccupied energy levels of a sample yielding information about the chemical state, interatomic distances and orientation of absorbed molecules. Experimental results contained in this thesis focus on Near Edge X-ray Absorption Fine Structure (NEXAFS) but for brevity, the acronym XAS shall be used.

During the process of x-ray absorption, an incident photon may be absorbed by an atom if the energy $h\nu$, of the x-ray photon is close to the binding energy of a core level electron. If this energy is equal to or above the ionisation energy, then photoionization takes place where photoelectrons are detected and contribute to the continuum absorption (transitions into the vacuum level), starting at the absorption edge, where $h\nu = E_i$.

If $h\nu < E_i$, then a photon can excite an electron from a core level into a higher unoccupied state associated within the same atom. Photoexcitation occurs into levels below the vacuum level. It is this second case which provides sharp and well defined structures which appear in the pre-edge spectral region, hence the name, Near Edge X-ray Absorption Fine Structure^[18]. Figure 2.9.

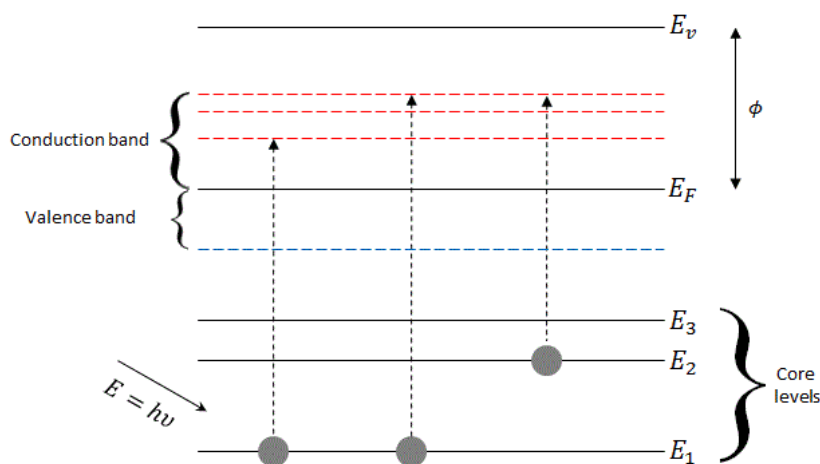


Figure 2.9: Principle of X-ray Absorption Spectroscopy.

Transitions from the 1s energy level exhibit one absorption edge known as the K-edge and have associated peaks labelled π^* and σ^* depending on the chemical nature and orientation of the atoms and molecules under investigation ^[19]. The molecules or atoms are susceptible to the polarisation of the incident photons depending on their orientation on the substrate. In a π conjugated molecular structure such as graphene lying parallel to the substrate, the π^* orbitals are perpendicular to the carbon lattice plane while the σ^* orbitals lie parallel to the plane (see Figure 2.10). Therefore, if the electric field vector is orientated perpendicular to the surface (grazing incidence) there will be a strong interaction with the π electrons. Conversely, if the synchrotron radiation is incident at normal incidence, i.e. the electric field vector is parallel to the plane, the σ electrons exhibit the more intense spectral features. From these spectral features it is possible to deduce the atomic coordination, chemical environment and molecular orientation of absorbed material on the surface if XAS spectra are measured at multiple incident angles.

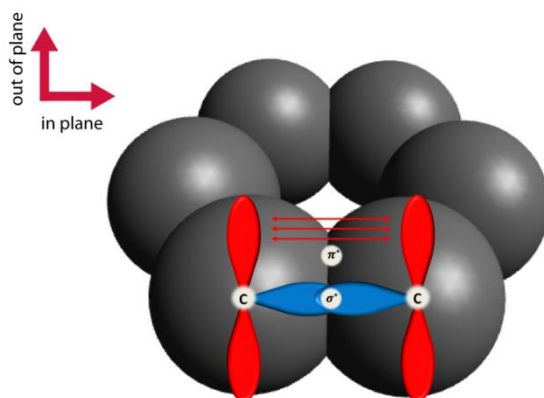


Figure 2.10: Orientation of π^ and σ^* molecular orbitals on a benzene ring.*

On Beamline D1011 a Partial Electron Yield (PEY) detection system is used to measure the XAS spectra. If the retarding voltage is set to zero, all electrons are analysed and the slow, low energy electrons, which have escaped from 10 – 20 nm dominate. It is advantageous to eliminate these electrons to enhance the signal to background noise level and also for greater surface sensitivity i.e. probing less than 5 nm of the surface is preferred ^[19]. By using a retarding negative voltage it becomes possible to stop the low energy electrons from reaching the analyser.

2.4 Ullmann reaction

Surface assisted synthesis of bromine functionalised organic molecules into polymerised and covalently bonded nanostructures is fundamental to this project and relies upon an Ullmann reaction. Ullmann, along with co-author Bielecki discovered how copper acts as a catalyst in the coupling of aromatic halides to produce biaryls ^[20, 21, 22] as shown in the reaction scheme in Figure 2.11. This concept was developed further, in solution and on surfaces ^[21, 20], and in particular, Rosei *et al.* have recently shown that an organometallic intermediate bonding of 1, 4-dibromobenzene to a covalently bonded polymerised nanostructure is possible ^[23]. An in depth discussion and applications of the Ullmann reaction can be found here ^[24, 25].



Figure 2.11: Ullmann reaction with copper chosen as the catalyst.

When analysing the Ullmann reaction on surfaces, it is found that there are two main reaction mechanisms which are substrate and temperature dependent ^[20]. If we denote Z to be any of the four metallic substrates investigated (Cu(111), Ag(111), Au(111) and Cu(110)) and X to be bromine then Figure 2.12 shows the chemical changes which occur upon interaction with the substrate and through thermal annealing ^[26].

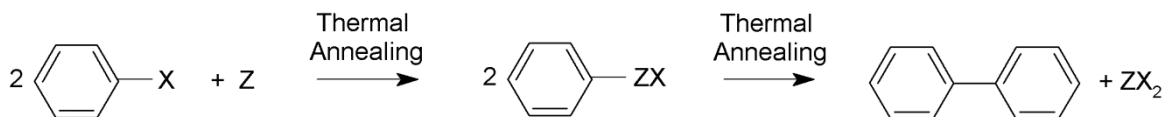


Figure 2.12: Ullmann reaction showing the intermediate stage where metal and halogen form a metal/organic complex.

2.5 Metal Surface

2.5.1 The Au(111), Ag(111) and Cu(111) surfaces

The metal substrates used in this thesis, Au(111), Ag(111), Cu(111) and Cu(110) were single crystals supplied by Surface Preparation Laboratory (SPL) in the Netherlands. All crystals had one side polished and were cut to a precision of $<0.5^\circ$. Figure 2.13 shows STM images of the four crystal surfaces after argon ion sputtering and annealing cycles. The cleanliness was checked visually via STM scanning and verified by XPS measurements where a low carbon to metal ratio would signify a high degree of cleanliness.

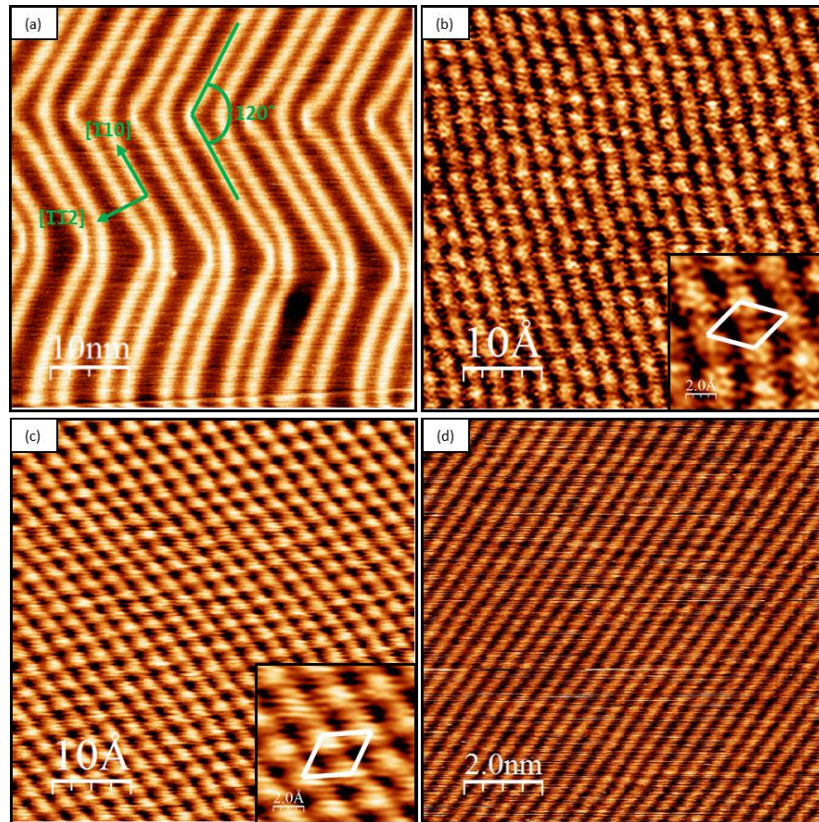


Figure 2.13: STM images of atomically clean substrates. (a) Au(111), ($V_b = -1.40V$, $I_t = 0.79nA$), (b) Ag(111), ($V_b = -2.71V$, $I_t = 2.28nA$), (c) Cu(111), ($V_b = 0.01V$, $I_t = 1.50nA$) and (d) Cu(110), ($V_b = -0.10V$, $I_t = 1.37nA$).

Au, Ag and Cu are all face centred cubic (fcc) crystals. A model of the (111) surfaces is shown in Figure 2.14 and information about the individual substrates highlighted in Table 2.1.

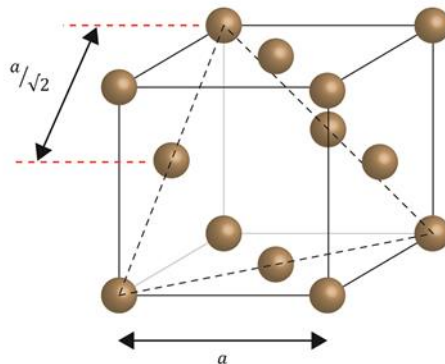


Figure 2.14: Face-centred cubic crystal showing the (111) plane where ‘a’ is the lattice parameter.

Element	Lattice parameter a (nm)	Surface atomic separation $a/\sqrt{2}$ (nm)	Interplane separation $a/\sqrt{3}$ (nm)
Au	0.408	0.288	0.236
Ag	0.409	0.289	0.236
Cu	0.361	0.255	0.208

Table 2.1: Information for the (111) crystal parameters.

The atomically clean Ag(111) and Cu(111) substrates exhibit a bulk extended 1×1 termination while the Au(111) reconstructs with a $22 \times \sqrt{3}$ unit cell often referred to as the ‘herringbone’ reconstruction, Figure 2.13 (a). This is caused by relaxation of the surface atoms at room temperature between fcc and hcp regions ^[27]. A contraction of the top layer of gold atoms in the $[\bar{1}\bar{1}0]$ direction gives rise to an hcp arrangement (bright rows) and a less densely packed fcc arrangement (dark rows). This arrangement occurs naturally to relieve stress in the crystal i.e. this is the most energetically favourable configuration where 23 gold atoms occupy 22 bulk lattice sites. The hcp region has a width of 2.5 nm which is narrower than the adjacent fcc region of 3.8 nm and exhibit a periodicity between parallel lines of approximately 6.3 nm ^[2].

Monocrystalline silver has a fcc lattice structure. The polished Ag(111) surface exhibits a hexagonal lattice with an interatomic distance of 0.289 nm. Gold is the least reactive of the

metal crystals under investigation, and conversely, copper is the most reactive and is therefore expected to have greater interaction with any adsorbate.

2.5.2 The Cu(110) Surface

The Cu(110) surface exhibits a ‘missing row’ reconstruction with a 2×1 periodicity shown in Figure 2.15. An STM image of the Cu(110) surface is shown in Figure 2.13 (d).

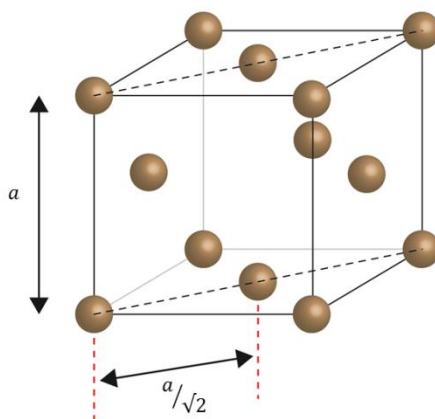


Figure 2.15: The (110) plane of a FCC crystal where ‘a’ is the lattice parameter.

2.6 Evaporation Cell

The molecules were deposited using a home-made evaporation cell which consisted of a Mo crucible resistively heated by a tungsten filament. A thermocouple, spot welded to the bottom of the crucible was used to monitor the temperature of the cell during deposition and initial degassing which all molecules required to ensure they were contaminant free. The temperatures required for deposition differ depending on the molecule.

2.7 Graphene and Graphene Nanoribbons

Graphene, first isolated in 2004 by Geim and Novosolov, consists of a single layer of carbon atoms arranged in a regular hexagonal array, Figure 2.16 [28]. The graphene sheet consists of hexagonal carbon rings. The intra planer bonding between adjacent carbon atoms is covalent and strong due to three electrons in sp^2 hybridised $2s$ and $2p_{xy}$ σ orbitals. The remaining electron occupies the $2p_z$ π orbital which is perpendicular to the

graphene plane, Figure 2.17. Since graphene exhibits perfect symmetry, the π electrons are delocalised throughout the one atom thick structure and it is this π conjugated electron arrangement which gives graphene its unique properties.

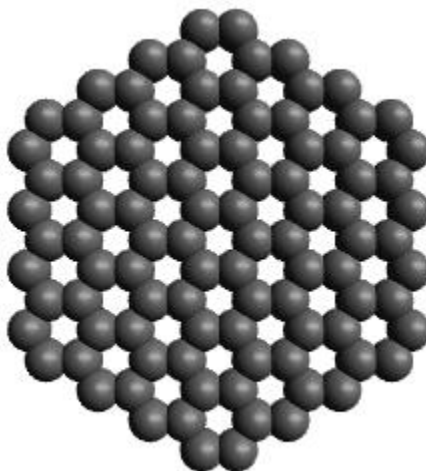


Figure 2.16: Structural model for graphene, top down view.

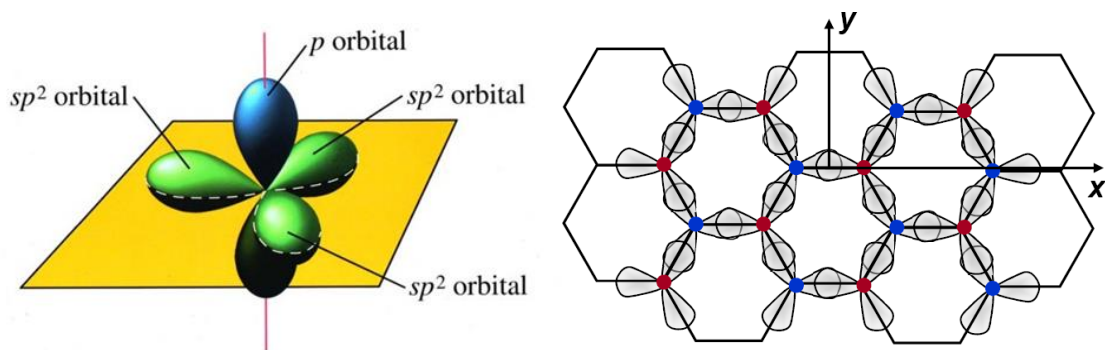


Figure 2.17: Schematic diagrams showing the orbital configuration from a side and top down view.

Due to its high charge carrier mobility, mechanical strength, flexibility and transparency, graphene is a very attractive material for applications in electronics, ultrafast photonics, photovoltaic cells, light emitting devices and touch screen technology ^[29]. Graphene devices have the potential of being smaller and transmitting data faster, while consuming less energy than the corresponding silicon based components in use today. For example, graphene-based transistors could run at speeds hundred to a thousand times faster than silicon transistors ^[30]. However, graphene has one significant disadvantage when compared with the silicon technology; it has no energy band-gap and therefore it cannot be used to

make transistors with a sufficient on/off ratio for electronic applications. A significant research effort has focused on this problem and has demonstrated that a significant energy band gap, inversely proportional to the width of the conducting channel, can be achieved by lateral confinement in graphene nanoribbons (GNRs), see Figure 2.18 ^[31]. However, a sizable gap can only be achieved in extremely narrow graphene nanoribbons (typically <10 nm) and this poses a serious technical challenge ^[32]. Chapters 5 and 6 address this issue by exploring a novel bottom-up approach to the formation of narrow nanoribbons on metal surfaces using a precursor molecule, 10,10'-dibromo-9,9'-bianthryl (DBBA) which can produce nanoribbons with a large energy band-gap. These aforementioned chapters describe the growth and spectroscopic characterisation of graphene nanoribbons and subsequent formation of graphene by Scanning Tunnelling Microscopy (STM) and synchrotron based x-ray spectroscopies.

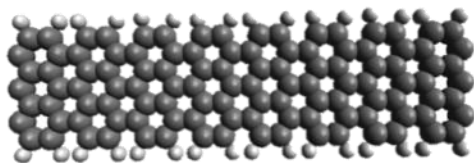


Figure 2.18: Structural model for a graphene nanoribbon where carbon atoms are represented in dark grey and hydrogen atoms in light grey.

2.8 References

- [1]BINNING, G., ROHRER, H., GERBER, C. & WEIBEL, E. 1982, "Surface Studies by Scanning Tunneling Microscopy", *Physical Review Letters*, vol. 49, no. 1, pp. 57-61.
- [2]Chen, C.J. 1993, *Introduction to scanning tunneling microscopy*, Oxford University Press New York.
- [3]Woodruff, D.P. & Delchar, T.A. 1994, *Modern techniques of surface science*, Cambridge University Press.
- [4]Wiesendanger, R. 1994, *Scanning probe microscopy and spectroscopy: methods and applications*, Cambridge University Press.
- [5]Tersoff, J. & Hamann, D. 1993, "Theory of the scanning tunneling microscope" in *Scanning Tunneling Microscopy* Springer, , pp. 59-67.
- [6]Vickerman, J.C. & Gilmore, I.S. 2009, *Surface analysis: the principal techniques*, Wiley Online Library.
- [7]Setvin, M., Javorsky, J., Turcinkova, D., Matolinova, I., Sobotik, P., Kocan, P. & Ost'adal, I. 2012, "Ultrasharp tungsten tips-characterization and nondestructive cleaning", *Ultramicroscopy*, vol. 113, pp. 152-157.
- [8]Zhang, R. & Ivey, D.G. 1996, "Preparation of sharp polycrystalline tungsten tips for scanning tunneling microscopy imaging", *Journal of Vacuum Science & Technology B*, vol. 14, no. 1, pp. 1-10.
- [9]Ekvall, I., Wahlstrom, E., Claesson, D., Olin, H. & Olsson, E. 1999, "Preparation and characterization of electrochemically etched W tips for STM", *Measurement Science & Technology*, vol. 10, no. 1, pp. 11-18.
- [10][*Tip Etching Kit User Manual, 1st ed., Omicron Nanotechnology, Taunusstein, Germany, 1998*].
- [11]Omicron NanoTechnology GmbH, URL <http://www.omicron.de/en/products/variable-temperature-spm/instrument-concept>.
- [12]Horcas, I., Fernandez, R., Gomez-Rodriguez, J., Colchero, J., Gómez-Herrero, J. & Baro, A. 2007, "WSXM: a software for scanning probe microscopy and a tool for nanotechnology", *Review of Scientific Instruments*, vol. 78, no. 1, pp. 013705.
- [13]I. Horcas, R. Fernandez, J.M. Gomez-Rodriguez, J. Colchero, J. Gomez-Herrero and A. M. Baro, *Rev. Sci. Instrum.* 78, 013705 (2007).

- [14]Hoffman, D., Singh, B. & Thomas III, J.H. 1997, *Handbook of vacuum science and technology*, Academic Press.
- [15]Seah, M. 1990, "Quantification of AES and XPS", *Practical surface analysis*, vol. 1, pp. 201-255.
- [16]*EIS/EIS Sphera Software User Guide, 2nd ed., Omicron Nanotechnology, Taunusstein, Germany, 2008.*
- [17]*Origin (OriginLab, Northampton, MA).*
- [18]Stöhr, J. 1992, *NEXAFS spectroscopy*, Springer.
- [19]Hähner, G. 2006, "Near edge X-ray absorption fine structure spectroscopy as a tool to probe electronic and structural properties of thin organic films and liquids", *Chemical Society Reviews*, vol. 35, no. 12, pp. 1244-1255.
- [20]Gutzler, R., Cardenas, L., Lipton-Duffin, J., El Garah, M., Dinca, L.E., Szakacs, C.E., Fu, C., Gallagher, M., Vondracek, M., Rybachuk, M., Perepichka, D.F. & Rosei, F. 2014, "Ullmann-type coupling of brominated tetrathienoanthracene on copper and silver", *Nanoscale*, vol. 6, no. 5, pp. 2660-2668.
- [21]Xi, M. & Bent, B.E. 1993, "Mechanisms of the Ullmann Coupling Reaction in Adsorbed Monolayers", *Journal of the American Chemical Society*, vol. 115, no. 16, pp. 7426-7433.
- [22]El Garah, M., MacLeod, J.M. & Rosei, F. 2013, "Covalently bonded networks through surface-confined polymerization", *Surface Science*, vol. 613, pp. 6-14.
- [23]Di Giovannantonio, M., El Garah, M., Lipton-Duffin, J., Meunier, V., Cardenas, L., Revurat, Y.F., Cossaro, A., Verdini, A., Perepichka, D.F., Rosei, F. & Contini, G. 2013, "Insight into Organometallic Intermediate and Its Evolution to Covalent Bonding in Surface-Confined Ullmann Polymerization", *Acs Nano*, vol. 7, no. 9, pp. 8190-8198.
- [24]Hassan, J., Sévignon, M., Gozzi, C., Schulz, E. & Lemaire, M. 2002, "Aryl-aryl bond formation one century after the discovery of the Ullmann reaction", *Chemical reviews*, vol. 102, no. 5, pp. 1359-1470.
- [25]Lin, H. & Sun, D. 2013, "Recent Synthetic Developments and Applications of the Ullmann Reaction. A Review", *Organic Preparations and Procedures International*, vol. 45, no. 5, pp. 341-394.
- [26]Fan, Q., Wang, C., Han, Y., Zhu, J., Kuttner, J., Hilt, G. & Gottfried, J.M. 2014, "Surface-Assisted Formation, Assembly, and Dynamics of Planar Organometallic

Macrocycles and Zigzag Shaped Polymer Chains with C-Cu-C Bonds", *Acs Nano*, vol. 8, no. 1, pp. 709-718.

- [27] Vanhove, M.A., Koestner, R.J., Stair, P.C., Biberian, J.P., Kesmodel, L.L., Bartos, I. & Somorjai, G.A. 1981, "The Surface Reconstructions of the (100) Crystal Faces of Iridium, Platinum and Gold .1. Experimental-Observations and Possible Structural Models", *Surface Science*, vol. 103, no. 1, pp. 189-217.
- [28] Geim, A.K. 2009, "Graphene: Status and Prospects", *Science*, vol. 324, no. 5934, pp. 1530-1534.
- [29] Stampfer, C., Schurtenberger, E., Molitor, F., Guettinger, J., Ihn, T. & Ensslin, K. 2008, "Tunable graphene single electron transistor", *Nano Letters*, vol. 8, no. 8, pp. 2378-2383.
- [30] Heath, J.R. 2009, "Molecular Electronics", *Annual Review of Materials Research*, vol. 39, pp. 1-23.
- [31] Jiao, L., Zhang, L., Wang, X., Diankov, G. & Dai, H. 2009, "Narrow graphene nanoribbons from carbon nanotubes", *Nature*, vol. 458, no. 7240, pp. 877-880.
- [32] Son, Y., Cohen, M.L. & Louie, S.G. 2006, "Half-metallic graphene nanoribbons", *Nature*, vol. 444, no. 7117, pp. 347-349.

Chapter 3

Self-assembly and Covalent Bonding of Hexabromotriphenylene (HBTP) Molecules on Au(111), Ag(111) and Cu(111) surfaces

3.1 Introduction

Chemical reactions involving the cleaving of carbon-halogen bonds have drawn considerable interest in the field of molecular electronics since such reactions provide opportunities for fabricating surfaces with desirable patterned networks^[1]. Previous studies of molecular nano-architectures formed through debromination of molecules have been carried out, most notably network formation of tetra(4-bromophenyl) porphyrin (TBrPP) on Au(111) reported by Grill *et al.*^[1]. In this study, the molecules were debrominated through thermal annealing and subsequently, after molecular diffusion on the surface, were capable of forming covalently bonded networks due to the debrominated porphyrin radical subunits. Gutzler *et al.*^[2] successfully showed that dehalogenation of 1,3,5-tris(4-bromophenyl) benzene (TBB) depends on the substrate which plays a vital chemical role. They observed an intermediate organometallic stage in the covalent bonding process^[3]. In an Ullmann coupling reaction, a radical-copper bond is formed after dehalogenation and before covalent bonding between adsorbates begins. On Cu(111), this C-Cu-C arrangement has been observed as being stable at room temperature. Covalently bonded networks of a 5,10,15,20-tetrakis(4-bromophenyl) porphyrinatoNi(II) molecule (NiTBrPP) exhibit similar behaviour, as reported by Doyle *et al.*, where extended covalently bonded networks form on the Au(111) substrate and remain stable up to $\sim 530^\circ\text{C}$ ^[4]. These surface-assisted debromination reactions for forming covalently bonded organic material aid the understanding of the behaviour of molecules at the atomic scale and provide an insight into how molecular electronics may be developed.

In order to fully realise the goal of molecular electronics, strong, patterned, stable and electronically efficient covalent bonding must firstly be achieved. Moving through the stages, from single molecules with specific electronic properties to ordered surface

assemblies followed by designed, non-periodic surface assemblies will help promote molecular electronics to the forefront of surface science and, in particular, device manufacture ^[5]. Hindering these important technological advances however, is the lack of understanding of the fundamental atomic and molecular chemical changes which underpin the covalent bonding process. Understanding these changes forms the basis of this chapter. In this work, surface assisted cleaving of C-Br bonds through thermal activation, leads to the creation of free radicals which can subsequently diffuse on the surface and form covalent bonds ^[2]. This type of network formation is of paramount importance to the research and development of molecular electronics which uses a ‘bottom up’ approach. Presented in this chapter is an STM and XPS analysis of the self-assembly, debromination and subsequent covalent bonding of 2, 3, 6, 7, 10, 11, hexabromotriphenylene (HBTP) on the Au(111), Ag(111) and Cu(111) surfaces. Of particular interest is how the reactivity of the substrate affects the debromination process.

HBTP is a bromine functionalised molecule consisting of four centrally fused benzene rings with six bromine atoms at the 2, 3, 6, 7, 10 and 11 positions, as shown in Figure 3.1.

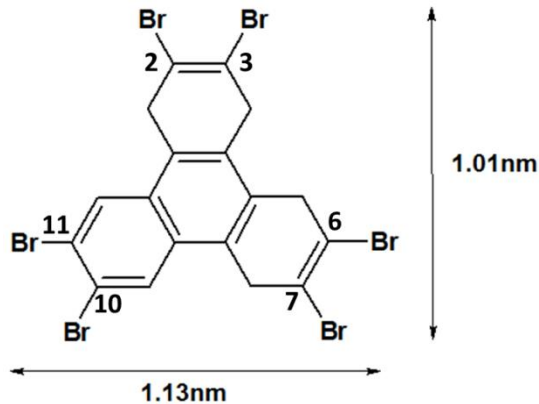


Figure 3.1: Chemical structure of HBTP with dimensions calculated from Chemsketch ^[6]. Hydrogen atoms are omitted for clarity.

3.2 STM and XPS Study of HBTP on the Au(111) Surface

Due to the nature of the weak molecular-substrate interaction HBTP molecules exhibit a high level of molecular mobility when submonolayer coverages are deposited on the Au(111) substrate. As a result, STM imaging of submonolayer coverages of this molecule on Au(111) at room temperature proved unsuccessful. Coverages of close to one monolayer (ML) and greater were achieved by deposition of HBTP onto the Au(111) surface at room temperature from a Knudsen cell held at 205°C for 2 hours. The result is a well-ordered and stable, self-assembled monolayer as shown in the STM image (Figure 3.2). Van der Waals interactions involving the hydrogen and bromine constituents of the HBTP molecules play a major role in the self-assembly where the underlying herringbone surface reconstruction ($22 \times \sqrt{3}$) is still visible. This suggests that the HBTP molecules are physisorbed on the substrate as the underlying reconstruction remains undisturbed, i.e. the molecule-molecule interaction dominates over the molecule-substrate interaction. This weak interaction between organic molecules and the gold surface has been previously reported by Jiang *et al.* [7] and others [8, 9]. At room temperature the HBTP molecules in each domain assemble in a hexagonally packed arrangement with a 120° rotation between adjacent domains. The contrast in the STM image results from differences in the electronic structure between the HBTP and the underlying Au(111) substrate in the FCC and HCP regions [10]. Line profile measurements are used which provide unit cell dimensions of $1.27 \times 1.13 \text{ nm} \pm 0.05 \text{ nm}$ in both the FCC and HCP regions of the surface, Figure 3.2 (b).

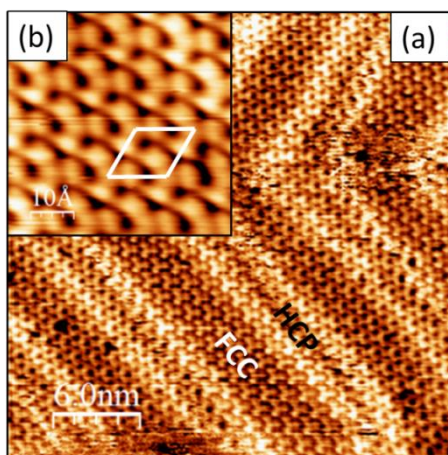


Figure 3.2: STM for 1ML of HBTP deposited on Au(111) held at room temperature. The FCC and HCP domains are shown. (a) ($V_b = 1.0\text{V}$, $I_t = 0.33\text{nA}$) and (b) a magnified image to highlight the unit cell ($V_b = 1.0\text{V}$, $I_t = 0.33\text{nA}$).

Figure 3.3 shows Br 3p core level XPS spectra, recorded from ~1 ML of HBTP on the Au(111) surface, after successive 15 minute anneals. This data was fitted with one (for the RT spectrum) or two (for the 150°C, 250°C and 350°C spectra) Gaussian function fitted doublets with a spin orbit splitting of $6.30 \pm 0.05\text{eV}$. The two doublets are separated by $1.80 \pm 0.05\text{eV}$. At RT the Br $3p_{3/2}$ component at $183.60 \pm 0.05\text{eV}$ is associated with molecular bromine (i.e. bromine attached to the HBTP molecule). The $3p_{3/2}$ component at a lower binding energy of $181.80 \pm 0.05\text{eV}$ is attributed to bromine atoms which have dissociated from the molecule onto the Au(111) substrate. This second doublet becomes apparent after annealing to 150°C.

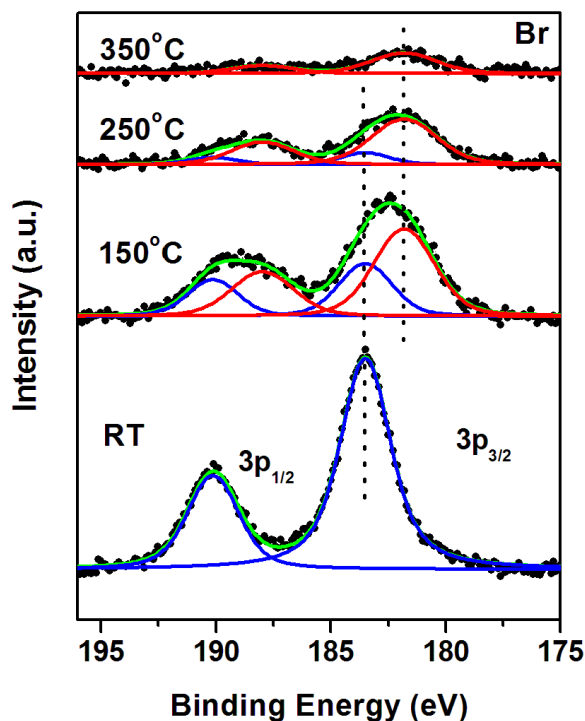


Figure 3.3: XPS of ~1 ML of HBTP deposited on room temperature Au(111) and progressive anneal stages. Br 3p region.

Little or no debromination has occurred at RT since only one component is observed and fitted in the spectrum. It is possible that a second doublet component could be present at lower binding energy but due to the statistics gathered and apparent noise in the spectrum, this is difficult to determine with any certainty. Upon annealing to 150°C, partial debromination occurs resulting in the appearance of the second doublet. The areas under

the Br 3p core level line shape enables percentages of molecular bromine and atomic bromine which are present to be calculated. At the 150°C anneal stage approximately 37% of the bromine is still bound to the HBTP molecule (2 bromine atoms) while the remaining bromine has dissociated and is attributed to bromine on the Au(111) surface (4 bromine atoms). There is also approximately a 26% decrease in intensity relative to the RT signal intensity. This decrease is attributed to desorption of HBTP molecules and atomic bromine from the surface. This is further evidence of the weak molecule-surface interaction. Increasing the anneal temperature to 250°C and 350°C results in further decreases in the total intensity of the Br 3p signal. This is accompanied by an increase in debromination with approximately 83% and 95% of total bromine dissociated onto the Au surface at 250°C and 350°C respectively. After annealing to 350°C there are disordered structures observed on the surface, where islands and chains of organic material are observed, Figure 3.4, where the Au(111) herringbone structure is still visible.

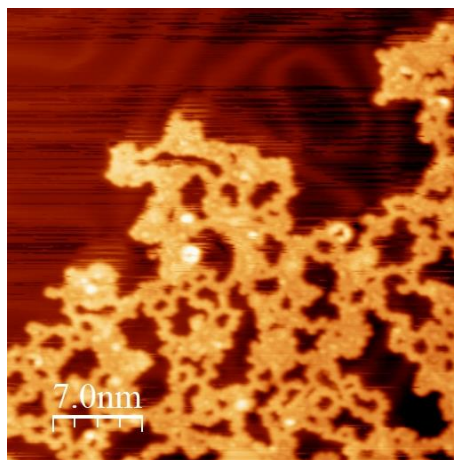


Figure 3.4: 35 nm × 35 nm STM image of HBTP molecules deposited at RT and annealed to 350°C. ($V_b = 0.19V$, $I_t = 0.44nA$).

In order to achieve more ordered networks, HBTP was deposited onto the clean Au(111) ($22 \times \sqrt{3}$) surface held at elevated temperatures of 150°C, 200°C and 250°C. Figure 3.5 show a series of STM images associated with each deposition and taken at different bias. The different bias conditions probe different molecular orbitals and hence provide different contrast in different images. The corresponding XPS spectra of the Br 3p core level representing each deposition are shown in Figure 3.6.

Figure 3.5 (a) shows evidence of unreacted HBTP molecules which have self-assembled amongst a disordered, covalently bonded network. The self-assembled arrangement mimics the previously observed arrangement of HBTP deposited onto the RT surface, as seen in Figure 3.2. This visual evidence of HBTP in two different states (in molecular and covalently bonded form) enhances the proposed idea from the XPS spectra (Figure 3.3) that partial debromination has taken place at this temperature. The unit cell of the ordered region has increased to 1.43×1.55 nm from the previously measured 1.27×1.13 nm. It is proposed that dissociated bromine acts as a ‘spacer’ between the HBTP molecules creating this enlarged unit cell.

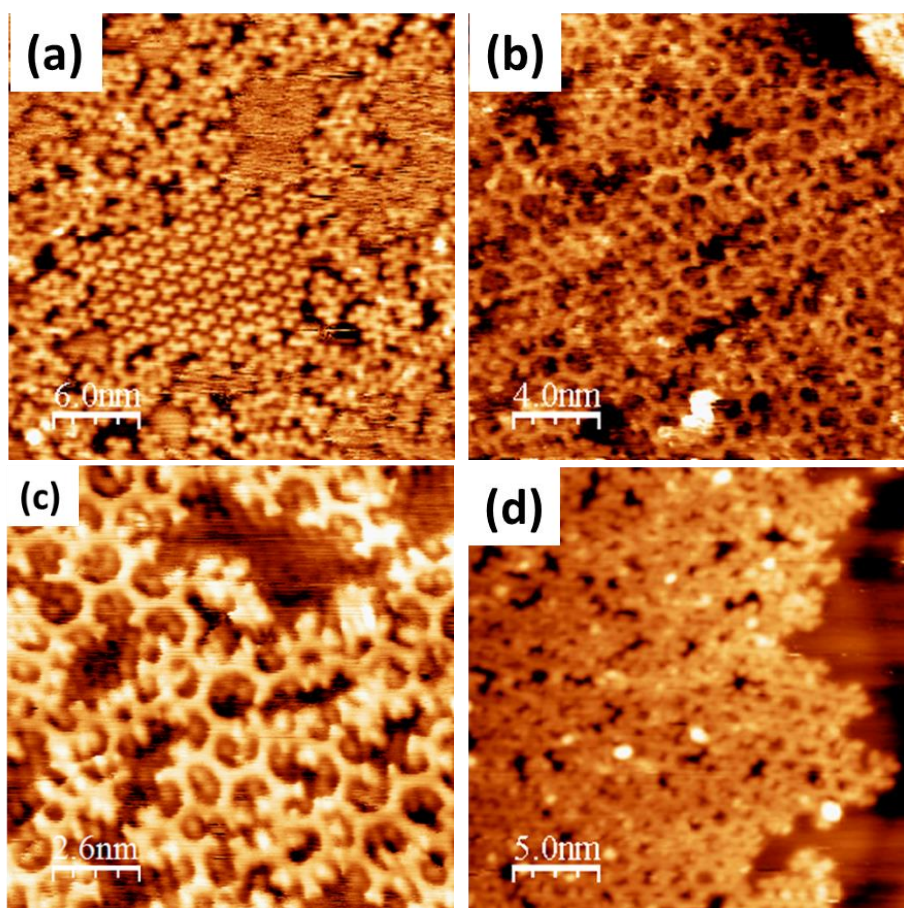


Figure 3.5: STM for HBTP deposited on Au(111) held at a temperature of (a) 150°C ($V_b = 1.7\text{V}$, $I_t = 0.06\text{nA}$), (b) and (c) 200°C ($V_b = 1.4\text{V}$, $I_t = 0.32\text{nA}$) and (d) 250°C ($V_b = 1.0\text{V}$, $I_t = 0.45\text{nA}$).

Figure 3.5 (b) and (c) show images of covalently bonded structures after depositing HBTP onto the Au(111) surface held at 200°C . Further debromination has occurred as indicated by the higher percentage of surface bromine in the XPS spectra. This increase in

debromination results in more active sites on the molecule, which in turn, leads to an increase in the probability that covalent bonding takes place. There is no evidence of self-assembled and unreacted HBTP molecules at this 200°C anneal stage as previously seen at 150°C. These networks are widespread over the Au(111) surface and exhibit uninterrupted covalently bonded chains up to 15 nm in length. Perfectly ordered networks are difficult to achieve using HBTP due to the six bromine atoms which provides six bonding sites after debromination. There are features within the hexagonal (width = 1.31 ± 0.05 nm) and pentagonal (width = 1.15 ± 0.05 nm) pores and also surrounding the networks. These features could be assigned to dissociated bromine atoms or perhaps gold adatoms.

XPS measurements shown in Figure 3.6 indicate that approximately 52% of bromine has dissociated from the HBTP molecule at 150°C. There is no STM evidence of unreacted HBTP molecules in the STM images of the higher temperature depositions. However, the percentage of dissociated bromine, as measured from the Br 3p XPS spectra, is approximately 54% and 56% at 200°C and 250°C respectively. The remaining bromine (approximately 46% and 44% respectively), still attached to the HBTP molecules, is evident from the unreacted region observed in the centre of Figure 3.5 (a) and in the unreacted areas of the networks in Figure 3.5 (c) and (d).

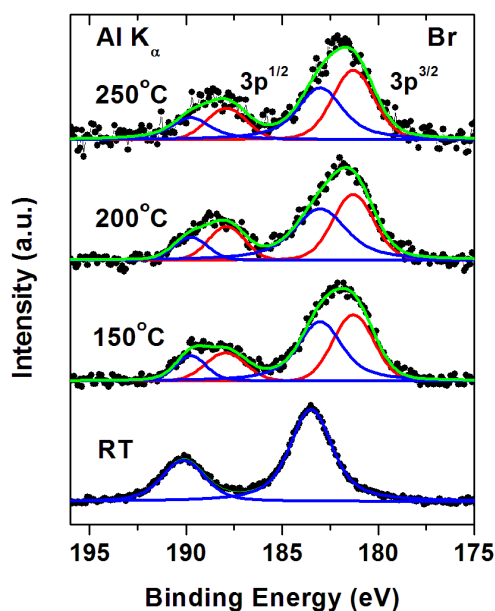


Figure 3.6: XPS of HBTP deposited onto elevated substrate temperatures. The RT deposition stage is shown as a guide.

When depositing onto the Au(111) surface held at 250°C, a highly disordered covalently bonded HBTP system is observed (Figure 3.5 (d)). Therefore, the optimum substrate temperature to achieve covalently bonded networks of HBTP on the Au(111) surface is between 150°C and 200°C.

3.3 Covalent Bonding Configurations on the Au(111) Surface

Different bonding configurations of HBTP molecules were observed on the Au(111) surface. Figure 3.7 shows models of the most common bonding arrangements. When three HBTP molecules align in the configuration shown in Figure 3.7 (a) they covalently bond creating a ring structure. On occasion, the molecules are not perfectly aligned when debromination occurs, as shown in Figure 3.7 (b), and subsequent covalent bonds create a disorder and rotation in the resultant networks. Calculation of distances using Chemsketch software in parallel with known models enables an accurate assessment to be made of bond formation between HBTP molecules. The model predicts a centre to centre distance of 0.94 nm when a double carbon square bridging bond is formed as shown in Figure 3.7 (c) – the covalent bonds are highlighted in green. This is in close agreement with a distance of 0.96 ± 0.02 nm determined from line profile measurements.

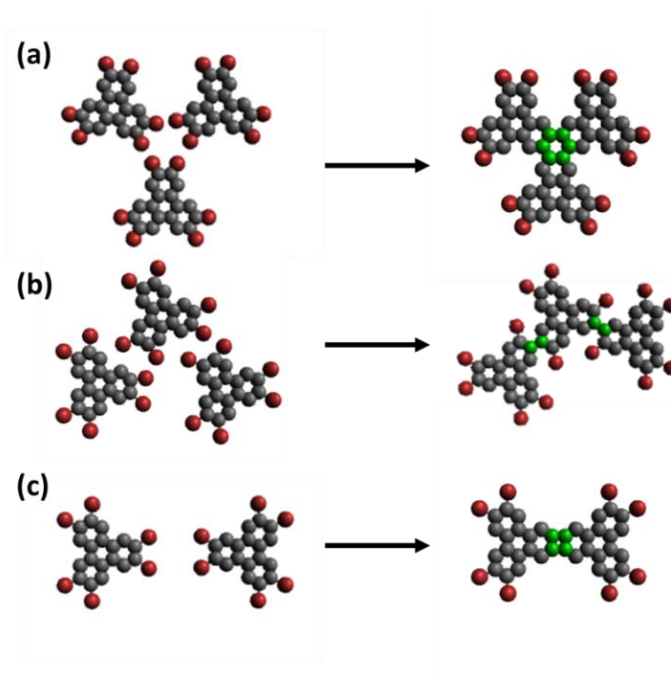


Figure 3.7: Different bonding configurations of HBTP molecules. The green atoms represent the newly formed bonds.

Figure 3.8 shows STM images of covalently bonded structures observed on the Au(111) surface and confirm the bonding arrangements discussed above. The insets in the corner of each image show models of the proposed bonding.

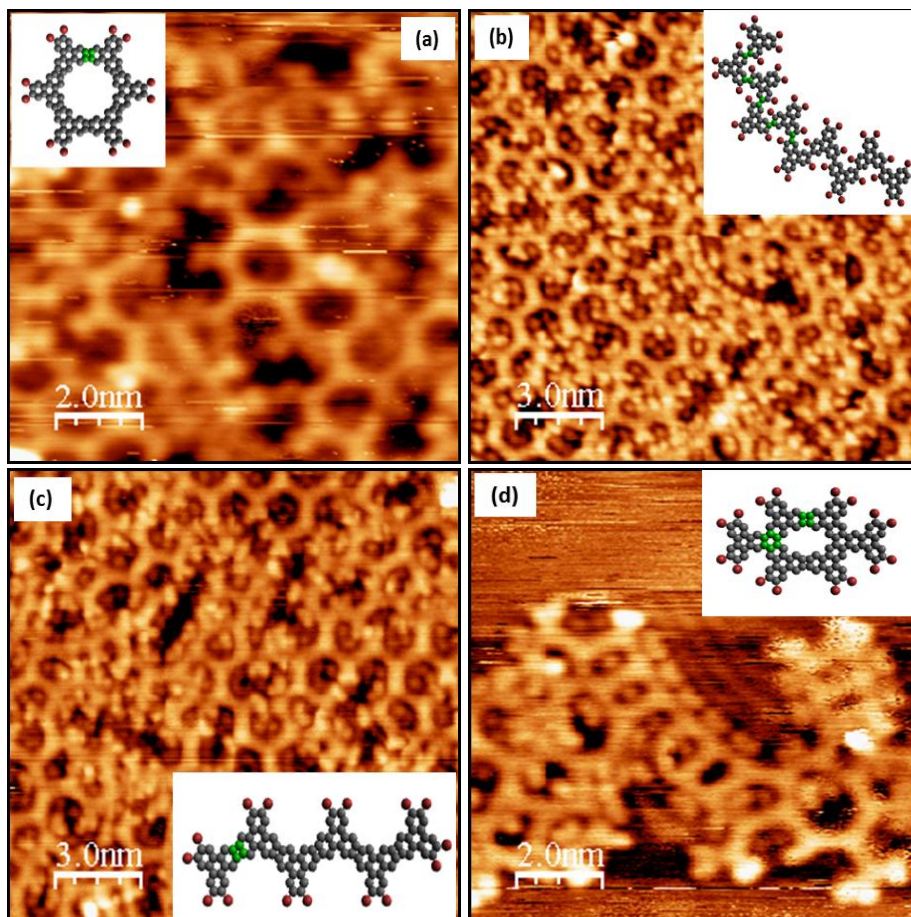


Figure 3.8: Different covalent bonding formations of HBTP on the Au(111) surface, (a) hexagonal ($V_b = 0.10V$, $I_t = 0.82nA$), (b) curved HBTP chain, ($V_b = -0.14V$, $I_t = 0.15nA$), (c) linear chain, ($V_b = 0.17V$, $I_t = 0.10nA$) and (d) elongated hexagonal bonding, ($V_b = -0.13V$, $I_t = 0.10nA$).

The images shown in Figure 3.8 provide direct evidence to support the proposed bonding configurations presented in Figure 3.7. Figure 3.8 (a) shows HBTP deposited onto the substrate held at 200°C and subsequently annealed to 250°C where hexagonal structures are observed. Figure 3.8 (b) shows HBTP deposited onto the Au(111) surface held at 200°C, showing a strained arc-like structure. This occurs when the HBTP molecules are misaligned during the reaction phase leading to one carbon-carbon bond forming between adjacent

subunits. This induces rotation around this bond. The same bonding process occurs through the chain leading to a curving effect. Figure 3.8 (c) shows an image of HBTP deposited on the Au(111) surface held at 200°C where linear chains are observed. These chains become disjointed and disrupted due to a high density of HBTP molecules and is also caused by the six carbon radical bonds created after debromination has occurred. Finally, Figure 3.8 (d) shows HBTP deposited onto the Au(111) surface held at 250°C resulting in an elongated hexagon which exhibits two different bonding configurations, a fused ring, Figure 3.7 (b), and a double carbon bridging bond, Figure 3.7 (c). Evidence of charge confinement between HBTP networks in the underlying Au(111) surface is apparent in Figure 3.8 (d) and shows a periodicity of $0.54 \text{ nm} \pm 0.02 \text{ nm}$.

3.4 STM and XPS Study of HBTP on the Ag(111) Surface

Figure 3.9 shows an STM image of the molecular packing configuration for a monolayer of HBTP deposited on the Ag(111) surface at RT. Similarly to HBTP deposition on the Au(111) surface, the molecules self-assemble with lattice dimensions of $1.55 \times 1.40 \text{ nm} \pm 0.05 \text{ nm}$. The fact that this unit cell is larger than that for HBTP deposition onto the RT Au(111) surface is due to dissociated bromine atoms between neighbouring molecules. These dissociated bromine atoms can be seen as bright circles (red spheres) between the molecules in Figure 3.9 (b). A model of HBTP molecules is superimposed onto the STM images to emphasise the orientation of the molecule on the Ag(111) surface. Three red bromine atoms per HBTP molecule have been omitted to emphasise the debromination at this stage. This appears to be an intermediate stage between bromine dissociation and covalent bonding. There is no evidence of network formation after room temperature deposition. However, partial debromination has occurred which allows the HBTP to adopt this structure.

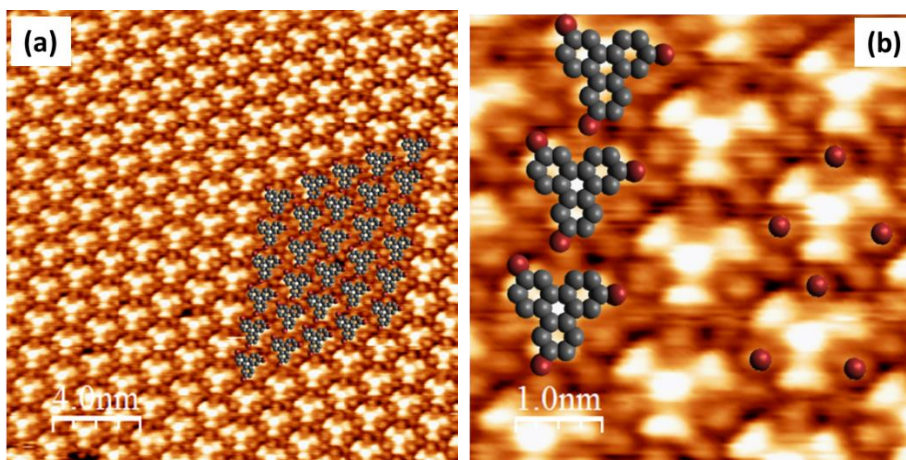


Figure 3.9: STM images for approximately 1ML of HBTP deposited on the Ag(111) surface held at room temperature. The vector directions of the unit cell are shown in (a) and a magnified image of the same surface in (b). A molecular schematic of the orientation of HBTP is provided in both (a) and (b) ($V_b = 1.7\text{V}$, $I_t = 0.26\text{nA}$)

The four connected bright lobes correspond to the four fused benzene rings of the HBTP molecule. The weaker protrusions observed between HBTP molecules have apparent widths of $0.20 \pm 0.02 \text{ nm}$, in agreement with a predicted bromine diameter of 0.22 nm and these features are therefore assigned to dissociated bromine. This proposed arrangement of

the HBTP molecules and dissociated bromine is confirmed by the normalised Br 3p XPS measurements shown in Figure 3.10. The RT spectrum here is significantly different from the spectra observed on the Au(111) surface at the same temperature. A second doublet, with approximately 51% of the total intensity, is observed at lower binding energy. This shows that, on average, three bromine atoms per molecule have dissociated at RT.

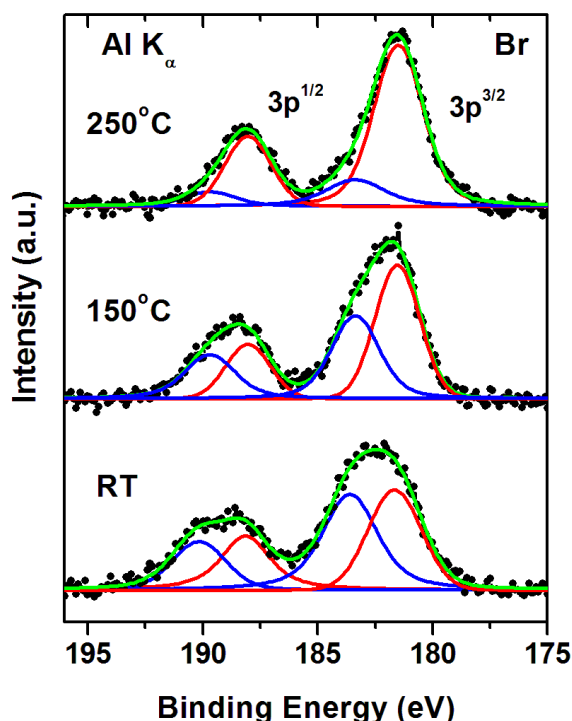


Figure 3.10: XPS of ~ 1 ML of HBTP deposited on the Ag(111) surface held at RT and subsequently annealed. Br 3p region.

The dissociated bromine component in the XPS spectra has a binding energy of 181.50 ± 0.05 eV (associated with the $3p_{3/2}$ transitions) and a spin orbit separation of 6.30 ± 0.05 eV. The $3p_{3/2}$ component of the bromine associated with the molecule has binding energy of 183.40 ± 0.05 eV. Annealing this surface to 150°C results in approximately 20% desorption of HBTP (not visible in the normalised data presented in Figure 3.10) from the surface and further debromination, where approximately 64% of bromine is now on the Ag(111) surface as opposed to the molecule and covalently bonded networks are observed as shown in the STM images in Figure 3.11.

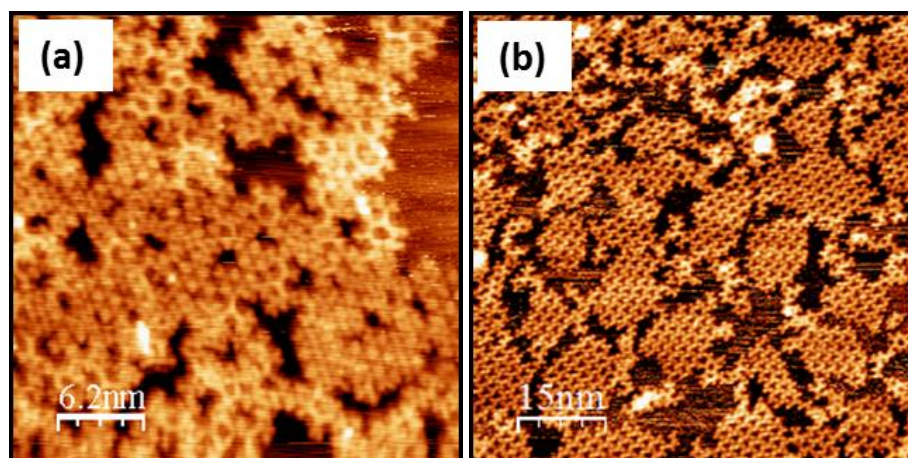


Figure 3.11: STM images of HBTP deposited at RT on the Ag(111) surface and subsequently annealed to 150°C (a) ($V_b = -0.38\text{V}$, $I_t = 0.14\text{nA}$) and (b) ($V_b = 1.4\text{V}$, $I_t = 0.24\text{nA}$).

When this surface is annealed to 250°C, the molecular bromine component at $183.40 \pm 0.05\text{eV}$ binding energy decreases in intensity and comprises approximately 19% of the total Br signal. This increase in bromine dissociation is accompanied by further desorption (approximately 20%) of HBTP molecules from the surface. The atomically resolved STM image shown in Figure 3.12 shows the remaining covalently bonded HBTP network after annealing to 250°C. Bromine atoms which have not dissociated from the HBTP molecule are observed as bright features at the edges of the covalently bonded structures and are associated with the 19% contribution in the XPS measurements. At this stage covalent bonding is complete. Hexagonal and pentagonal pores are observed with diameters of $1.49 \pm 0.05\text{ nm}$ and $1.17 \pm 0.05\text{ nm}$ respectively, in close agreement with the diameters measured on the Au(111) surface.

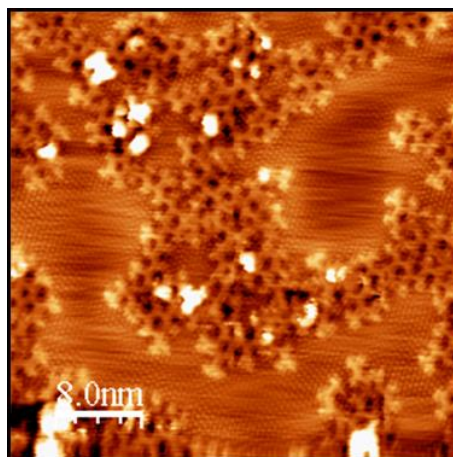


Figure 3.12: STM for HBTP deposited at RT on the Ag(111) surface and subsequently annealed to 250°C ($V_b = 0.18V$, $I_t = 0.26nA$).

Figure 3.13 shows the Br 3p photoemission spectra recorded for approximately 0.6, 0.7 and 0.8ML of HBTP deposited on the Ag(111) surface at 150°C, 200°C and 250°C respectively. The spectra have been normalised for comparison purposes and the room temperature spectrum is included as a reference.

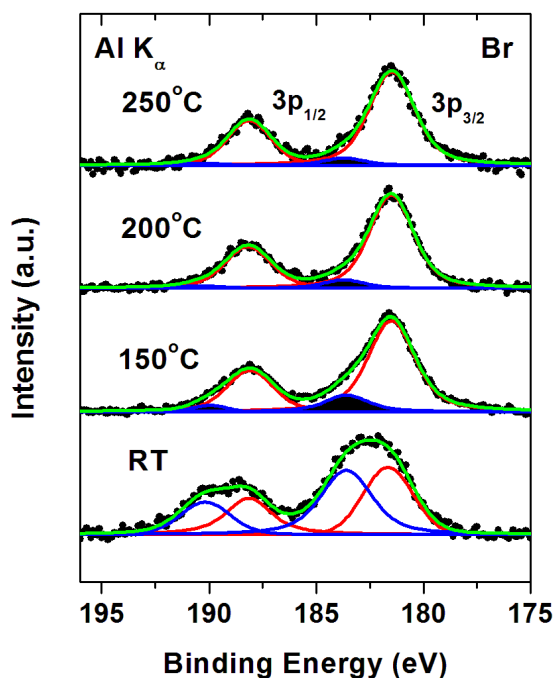


Figure 3.13: XPS of HBTP deposited on the Ag(111) surface held at different temperatures. RT deposition is shown as a reference. Br 3p region.

As before, the doublet with a $3p_{3/2}$ binding energy of $181.50 \pm 0.05\text{eV}$ is attributed to dissociated bromine while the doublet with a $3p_{3/2}$ binding energy of $183.40 \pm 0.05\text{eV}$ is attributed to bromine atoms which are still bonded to the HBTP molecule. There are differences in the relative intensities of the doublet when comparing room temperature deposition and subsequent annealing with elevated substrate temperature depositions. After depositing onto the Ag(111) surface held at 150°C , 200°C and 250°C , the XPS spectra shows that approximately 13%, 7% and 6% respectively, of the bromine signal, is attributed to molecular bromine. The remaining bromine atoms have dissociated and remain on the surface. Comparing these changes with HBTP deposited on room temperature Ag(111) and then annealed, it can be concluded that the cleaving of C-Br bonds occurs more efficiently when depositing onto a surface held at higher temperature. Covalently bonded porous networks are observed with varying degrees of order, Figure 3.14. The pores exhibit similar shapes and comparable dimensions to those found previously on the Au(111) substrate. Defects and disorder in the network formation process can be attributed to the steric hindrance of this system and the six bromine atoms of the HBTP molecule.

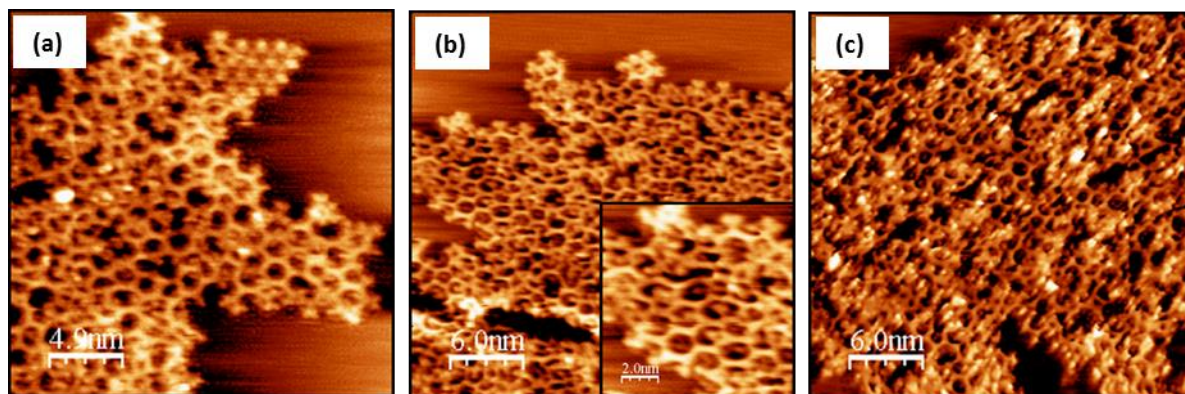


Figure 3.14: STM images of HBTP deposited on the Ag(111) surface elevated to (a) 420K ($V_b = 0.14\text{V}$, $I_t = 0.17\text{nA}$) (b) 470K (inset magnified $\times 3$), ($V_b = 0.18\text{V}$, $I_t = 0.26\text{nA}$) and (c) 520K ($V_b = -0.25\text{V}$, $I_t = 2.1\text{nA}$).

3.5 STM and XPS Study of HBTP on the Cu(111) Surface

In previous studies of the deposition of brominated tetrathienoanthracene and 1,4-dibromobenzene molecules onto the Cu(111) and Cu(110) surfaces respectively, it was found that debromination occurs at room temperature^[3, 11]. Furthermore, an intermediate organo-metallic bonding configuration has been observed, at room temperature, before the formation of covalent networks^[11].

Figure 3.15 (a) shows an STM image taken after deposition of approximately 0.5ML of HBTP on the Cu(111) substrate held at room temperature and Figure 3.15 (b) shows an STM image after the surface is annealed to 200°C. The presence of six bromine atoms and the reactivity of the copper at room temperature lead to either covalent bonding or the organo-metallic bonding described above. No long range order is observed at this stage. After annealing, the HBTP has started to decompose.

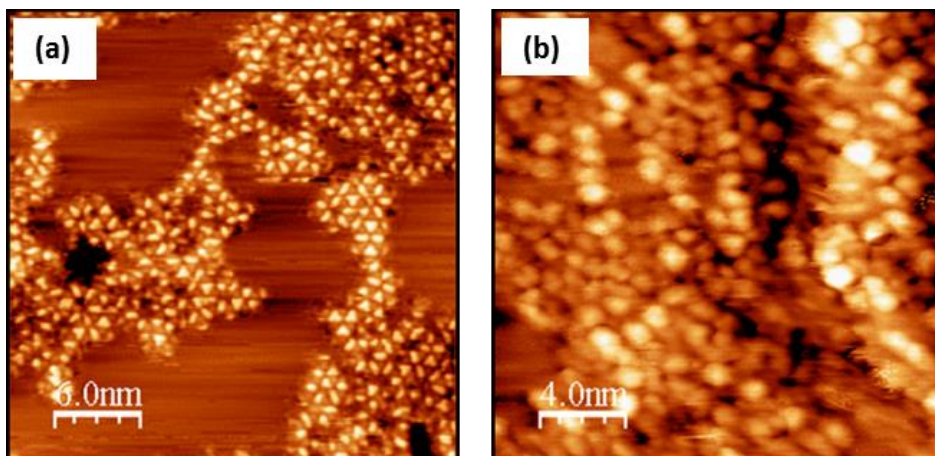


Figure 3.15: STM images for HBTP on Cu(111), (a) room temperature deposition ($V_b = 1.0V$, $I_t = 0.33nA$) and (b) annealing the surface to 200°C ($V_b = -1.0V$, $I_t = 1.0nA$).

Figure 3.16 shows Br 3p XPS spectra measured after depositing HBTP on the Cu(111) surface held at RT, 200°C and 250°C. The Br 3p_{3/2} component with a binding energy of 182.00 ± 0.05eV is attributed to dissociated bromine as previously discussed, while the component with a 3p_{1/2} binding energy of 184.80 ± 0.05eV is attributed to bromine atoms which are still bonded to the HBTP molecule. After depositing HBTP onto the Cu(111) surface at RT the Br signal attributed to bromine on the surface equates to approximately 95% of the total signal. Annealing to 200°C and then 250°C sees this signal increase to approximately 96% and 99% respectively. This implies that the majority of C-Br bonds cleave at RT on the Cu(111) surface and no significant change is observed during subsequent anneal stages. These measurements also suggest that bromine remains on the copper surface up to at least 250°C.

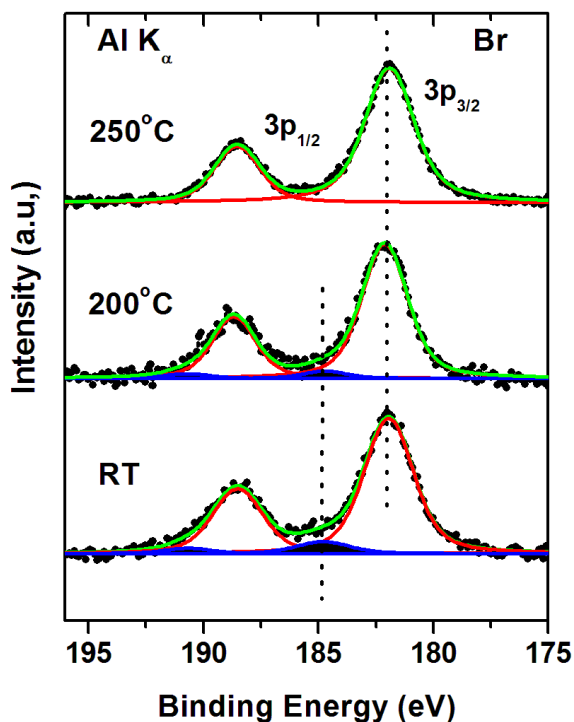


Figure 3.16: XPS spectra of ~0.5ML of HBTP deposited on room temperature Cu(111) and subsequently annealed to 200°C and then 250°C. Br 3p region.

Figure 3.17 shows the Br 3p core level photoemission spectra for two separate experiments recorded for approximately 0.4ML of HBTP on the Cu(111) surface. In the first experiment, the substrate is held at 150°C during deposition and subsequently annealed to 285°C. In the second, the substrate is held at 200°C during deposition. As before, the component with a Br 3p_{3/2} binding energy of 182.00 ± 0.05eV is attributed to dissociated bromine and the component with a Br 3p_{1/2} binding energy of 184.80 ± 0.05eV is molecular bromine (shaded in blue for clarity in Figure 3.17). The differences in the relative intensities of the components for deposition onto a substrate held at elevated temperatures, compared to depositing at room temperature and subsequent annealing, are negligible. After depositing onto the Cu(111) surface held at 150°C and 200°C, the proportion of the bromine signal attributed to surface bromine is approximately 95% and 96% respectively. After annealing the 150°C surface to 285°C, only one doublet is observed, i.e. debromination is complete and all Br species are found on the copper surface.

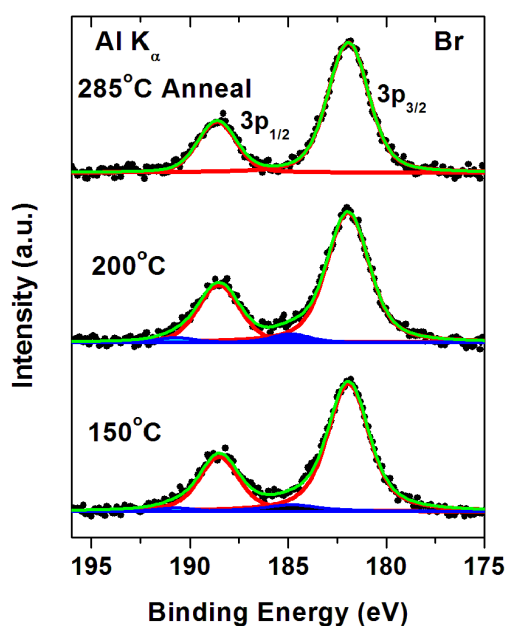


Figure 3.17: XPS of HBTP deposited on the Cu(111) surface held at different temperatures and then annealed from 150°C to 285°C. Br 3p region.

Comparing these changes with HBTP deposited on the Cu(111) surface at room temperature and subsequently annealed, it can be concluded that the cleaving of C-Br bonds occurs at room temperature. The high reactivity displayed by the copper surface could be due to its electronic structure and the availability of more adatoms at room temperature (when compared to Ag and Au) which can engage in the Ullmann reaction ^[12, 13]. These adatoms are less energetically bound on the copper surface and step edges, enabling such atoms to diffuse and engage more readily in reactions. The fact that the bromine is still present on the Cu(111) surface after annealing to 285°C suggests a strong bromine-copper interaction.

Figure 3.18 shows STM images recorded at both deposition stages described above for the XPS measurements.

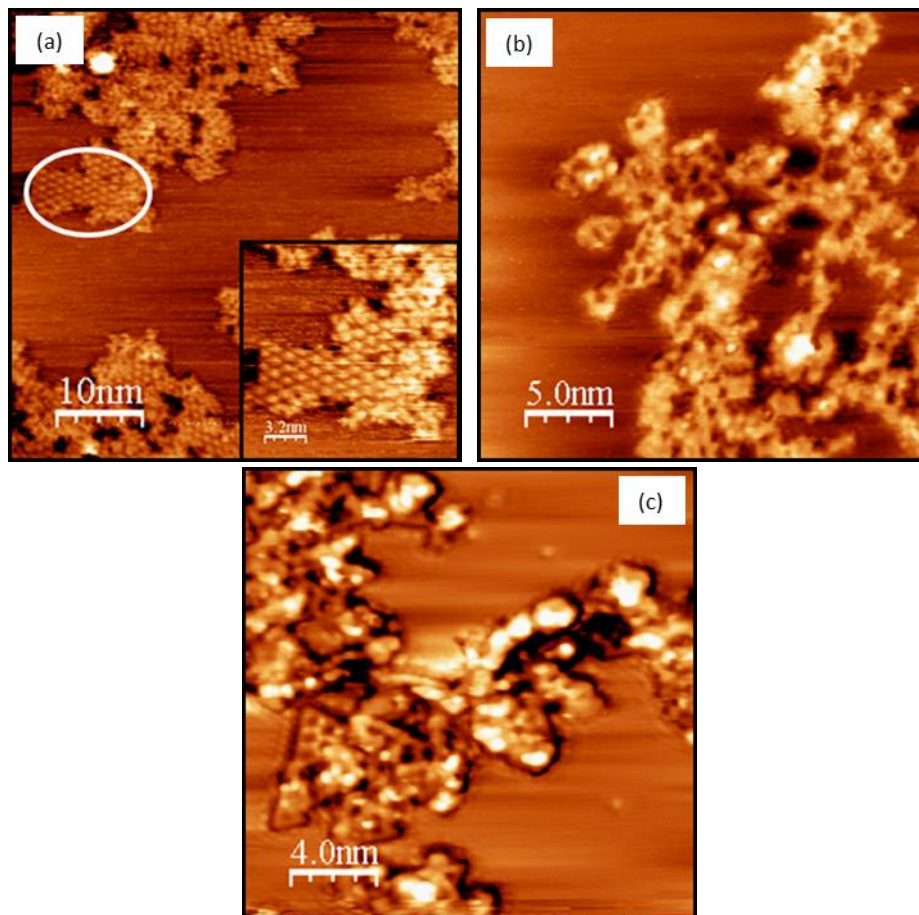


Figure 3.18: STM images of HBTP deposited on the Cu(111) surface elevated to (a) 150°C ($V_b = 1.0V$, $I_t = 0.1nA$) (b) 200°C ($V_b = 0.17V$, $I_t = 0.1nA$) and (c) 150°C surface annealed to 285°C ($V_b = -0.6V$, $I_t = 0.1nA$).

There is short range order observed in Figure 3.18 (a) which is either covalently bonded HBTP molecules or an organo-metallic configuration with Cu atoms between the HBTP molecules. No improvement is observed in the network formation when the sample temperature is increased, Figure 3.18 (b) and (c).

3.6 Comparison of HBTP on Au(111), Ag(111) and Cu(111) surfaces at Room Temperature

This study of HBTP deposited on the Au(111), Ag(111) and Cu(111) substrates allows two main conclusions to be made regarding the formation of covalently bonded structures. First, the substrate plays a significant role in the debromination reaction and hence, on the formation of molecular networks. Second, when debromination occurs there are six possible radical sites created which have the potential to form covalent bonds between neighbouring molecules, leading to different geometrical configurations during network formation. Au(111), Ag(111) and Cu(111) differ greatly in their surface reactivity. If we consider the dynamics of debromination at room temperature for the three substrates, it is confirmed that Au is the least reactive and Cu the most reactive, due to the observed debromination on Cu and lack of debromination on the Au surface at RT. Figure 3.19 shows the XPS spectra for room temperature deposition of HBTP on the three surfaces investigated.

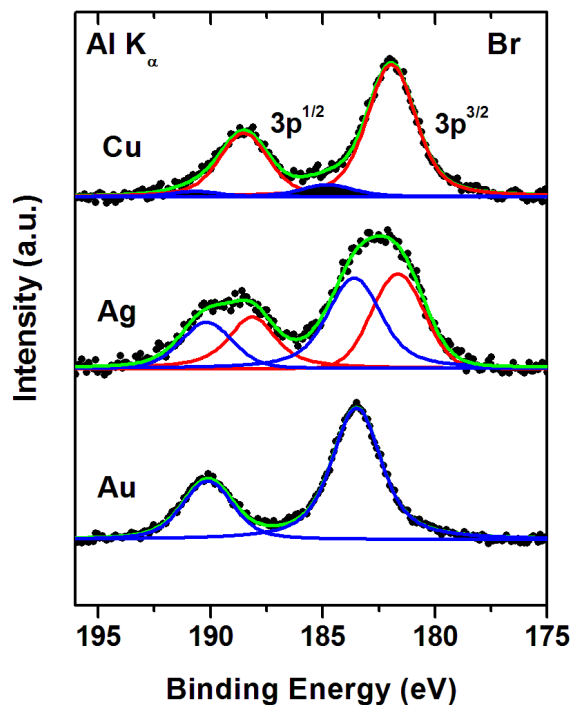


Figure 3.19: XPS spectra of HBTP deposited at room temperature on the Au(111), Ag(111) and Cu(111) surfaces.

In the case of Cu(111), debromination occurs readily at room temperature and approximately 95% of bromine is found to be dissociated. However, the high surface reactivity, cleaving of the C-Br bonds and presence of bromine on the surface does impinge on the quality of networks formed. For Ag(111), approximately 50% debromination has occurred at RT and subsequent annealing to 150°C allows covalently bonded nanostructures to form. Finally, the XPS spectrum for Au(111) shows that no debromination has taken place and temperatures of 200°C - 250°C are required to enable polymerisation and network formation on this surface. The fact that bromine desorbs more readily from the Au(111) surface, when compared to bromine desorption from the Cu(111) surface, is an additional indication of the strength of the Br-Cu interaction.

3.7 Dissociated Bromine on the Ag(111) and Cu(111) Surfaces

XPS spectra of HBTP deposited onto the Ag(111) surface and annealed to 250°C shows that approximately 80% of bromine has dissociated from the HBTP molecule but has not desorbed, i.e. atomic bromine is present on the Ag(111) surface. Upon further STM

analysis the atomic bromine was observed to form a $(\sqrt{3} \times \sqrt{3})R(30^\circ)$ structure on the surface. A large scale and magnified STM image of this reconstruction is shown in Figure 3.20.

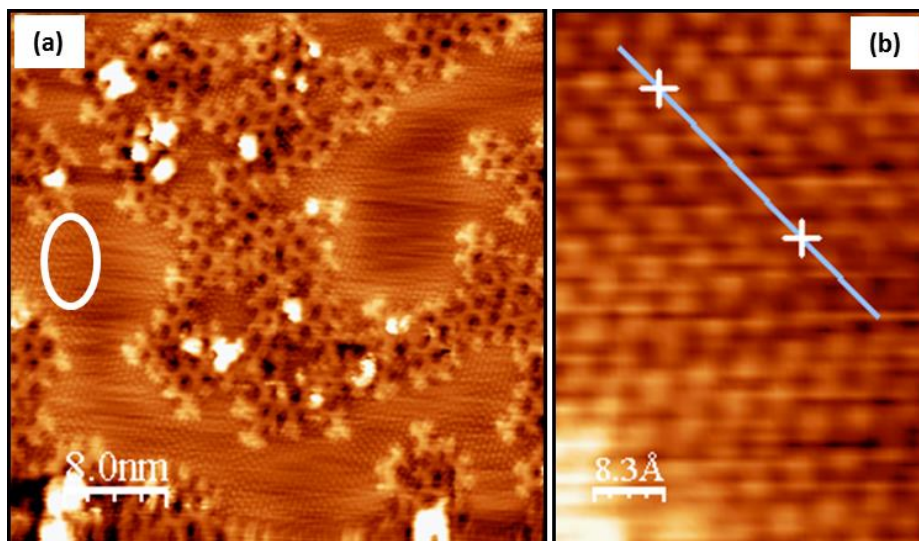


Figure 3.20: Evidence of dissociated bromine structure on the Ag(111) surface after RT deposition of HBTP and subsequent 250°C anneal. A large scale region of covalently bonded molecules is shown in (a) and (b) shows the magnified region circled in white in (a), both taken at $V_b = 0.19V$, $I_t = 0.27nA$.

It is not possible to predict whether the bromine atoms, which exhibit an apparent width of 0.29 ± 0.02 nm sit on a bridge or top site or FCC or HCP hollow site on the underlying silver substrate. Magnification (of the white circled region in Figure 3.20 (a)) and line spacing calculations from Figure 3.20 (b) show an area of isolated bromine atoms on the underlying Ag(111) surface where neighbouring atoms are 0.49 ± 0.05 nm apart. This separation is in agreement with the theoretically calculated $(\sqrt{3} \times \sqrt{3})$ spacing of 0.50 nm. This structure has been observed previously in electrochemical experiments and from a debromination process using 2,11-dibromohexabenzocoronene as a precursor molecule ^[14, 15]. A model of this structure is shown in Figure 3.21 assuming that the Br atoms sit in the hollow sites.

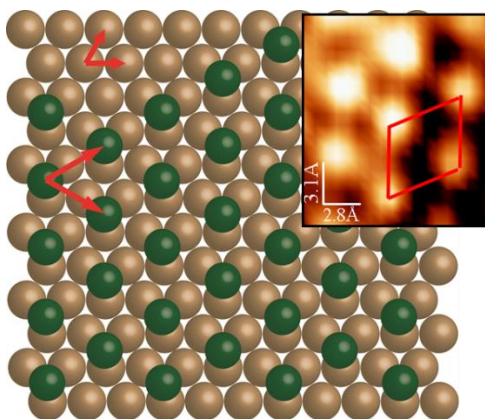


Figure 3.21: Graphical representation of the Ag(111) surface, bromine structural overlayer and corresponding lattice vectors with STM image showing atomic bromine.

Upon closer inspection of a region of the Cu(111) surface, close to a disordered covalently bonded region of HBTP on the Cu(111) substrate, an ordered feature is observed as shown in the area highlighted by a white oval in Figure 3.22 (a). The measured distance between these features, which are shown magnified in Figure 3.22 (b), is 0.45 ± 0.05 nm. The apparent width of these features attributed to bromine is 0.29 ± 0.02 nm, in agreement to their counterparts on the Ag(111) surface discussed above.

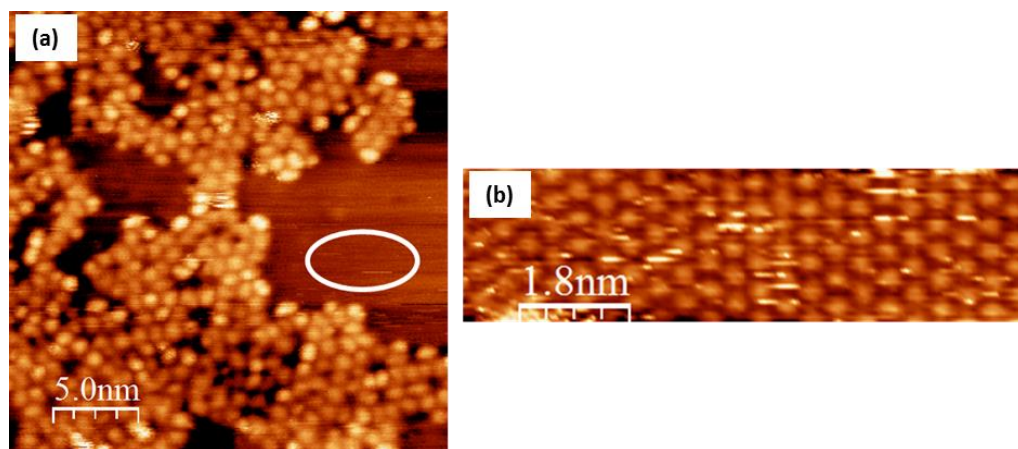


Figure 3.22: STM images of HBTP on Cu(111) showing (a) a disordered covalently bonded region of HBTP and (b) a magnification of the white circled region, both taken at $V_b = 1.5$ V, $I_t = 0.10$ nA.

The measured distances between atoms corresponds to the previously reported $(\sqrt{3}\times\sqrt{3})R(30^\circ)$ Br overlayer on Cu(111) ^[15]. The interatomic spacing on Cu(111) is 0.255 nm which leads to a bromine reconstruction of $0.255 \times \sqrt{3} = 0.441$ nm, in close agreement with calculated distances, supporting the proposed idea that these are bromine atoms ^[16]. Again, it is not possible to predict whether the bromine atoms conform to a hollow, bridge or top site on the underlying copper substrate. A model of this bromine structure (where hollow sites have been chosen) and corresponding STM image are shown in Figure 3.23.

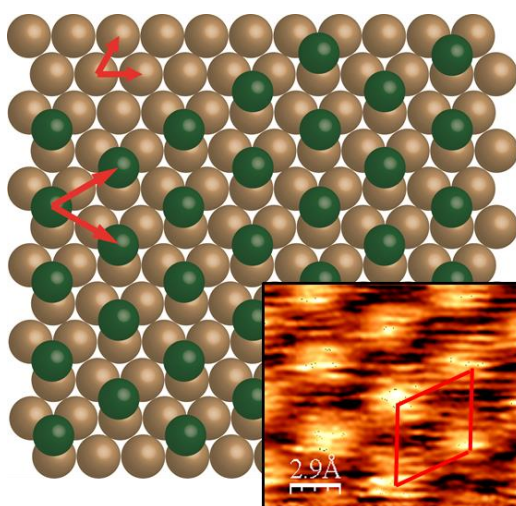


Figure 3.23: Graphical representation of the Cu(111) surface, bromine structural overlayer and corresponding lattice vectors with STM image showing atomic bromine.

3.8 Summary

Approximately 1 ML of HBTP self-assembles on the Au(111) at room temperature. XPS spectra show that debromination has not occurred. After annealing this surface to 150°C, the XPS spectra show that debromination has begun and reaches completion after annealing to 250°C. The molecules, observed through STM imaging, decompose after annealing to 350°C. The most favourable covalently bonded nano-networks are formed when HBTP is deposited on the Au(111) surface held at 200°C and exhibit a number of different bonding configurations. Uninterrupted covalently bonded chains up to 15nm in length are observed for this system and are randomly distributed on the surface. The network is thermally stable up to at least 250°C.

Dissociated bromine accounts for approximately 50% of the total bromine signal for HBTP deposited onto Ag(111) at room temperature. This leads to the formation of an intermediate state where the networks are coordinated by the dissociated bromine atoms which are observed between the self-assembled HBTP molecules. Further debromination occurs after annealing to 150°C and 250°C where covalently bonded networks are observed forming at 150°C and are completed at 250°C. Depositing HBTP onto Ag(111) held at elevated temperatures results in more debromination occurring when compared to RT deposition and subsequent annealing to the same temperatures. The most favourable ordered networks formed on the Ag(111) surface occur when HBTP is deposited at RT and annealed to 250°C or when HBTP is deposited onto Ag(111) held at 200°C.

When HBTP is deposited onto the RT Cu(111) surface, approximately 95% of bromine atoms have dissociated from the molecule. At this stage, it is possible that covalent bonding between HBTP molecules has occurred or an intermediate organo-metallic state has formed. After annealing to 250°C the XPS spectra show that debromination is complete. There are no significant differences between depositing HBTP on Cu(111) and subsequently annealing, as opposed to depositing onto Cu(111) held at elevated temperatures.

Dissociated bromine desorbs at higher temperatures on the Cu(111) surface when compared to Ag and Au. A cause for the disorder observed on the three metal surfaces is attributed to the six available reaction sites created after debromination has occurred. This leads to a conclusion that HBTP is not the most suitable candidate for the synthesis of surface supported covalently bonded networks.

Bromine atoms, after dissociating from HBTP, were found to assemble in a $(\sqrt{3}\times\sqrt{3})R(30^\circ)$ arrangement on the Ag(111) and Cu(111) surfaces after 250°C and 150°C anneals respectively. There was no evidence of such a reconstruction on the Au(111) surface due to bromine desorption at lower temperatures.

From these findings, the catalytic reactivity of the substrates under investigation has been established and follows $Au < Ag < Cu$. A greater insight into the reaction dynamics concerning the debromination of HBTP molecules on the three surfaces has been achieved. At RT, no debromination occurs on the Au(111) surface, partial debromination occurs on the Ag(111) surface and close to 100% debromination occurs on the Cu(111) surface.

3.9 References

- [1] Grill, L., Dyer, M., Lafferentz, L., Persson, M., Peters, M.V. & Hecht, S. 2007, "Nano-architectures by covalent assembly of molecular building blocks", *Nature Nanotechnology*, vol. 2, no. 11, pp. 687-691.
- [2] Gutzler, R., Walch, H., Eder, G., Kloft, S., Heckl, W.M. & Lackinger, M. 2009, "Surface mediated synthesis of 2D covalent organic frameworks: 1,3,5-tris(4-bromophenyl)benzene on graphite(001), Cu(111), and Ag(110)", *Chemical Communications*, , no. 29, pp. 4456-4458.
- [3] Gutzler, R., Cardenas, L., Lipton-Duffin, J., El Garah, M., Dinca, L.E., Szakacs, C.E., Fu, C., Gallagher, M., Vondracek, M., Rybachuk, M., Perepichka, D.F. & Rosei, F. 2014, "Ullmann-type coupling of brominated tetrathienoanthracene on copper and silver", *Nanoscale*, vol. 6, no. 5, pp. 2660-2668.
- [4] Krasnikov, S.A., Doyle, C.M., Sergeeva, N.N., Preobrajenski, A.B., Vinogradov, N.A., Sergeeva, Y.N., Zakharov, A.A., Senge, M.O. & Cafolla, A.A. 2011, "Formation of extended covalently bonded Ni porphyrin networks on the Au (111) surface", *Nano Research*, vol. 4, no. 4, pp. 376-384.
- [5] Otsuki, J. 2010, "STM studies on porphyrins", *Coordination Chemistry Reviews*, vol. 254, no. 19-20, pp. 2311-2341.
- [6] *Advanced Chemistry Development, Inc. (ACD/Labs)*.
- [7] Jiang, P., Deng, K., Fichou, D., Xie, S., Nion, A. & Wang, C. 2009, "STM Imaging ortho- and para-Fluorothiophenol Self-Assembled Monolayers on Au(111)", *Langmuir*, vol. 25, no. 9, pp. 5012-5017.
- [8] Nicoara, N., Roman, E., Gomez-Rodriguez, J.M., Martin-Gago, J.A. & Mendez, J. 2006, "Scanning tunneling and photoemission spectroscopies at the PTCDA/Au(111) interface", *Organic Electronics*, vol. 7, no. 5, pp. 287-294.
- [9] Lee, H.L. 2012, *Strategies for the formation of covalently bonded nano-networks on metal surfaces through amine reactions*.
- [10] Yamane, H., Kanai, K., Ouchi, Y., Ueno, N. & Seki, K. 2009, "Impact of interface geometric structure on organic-metal interface energetics and subsequent films electronic structure", *Journal of Electron Spectroscopy and Related Phenomena*, vol. 174, no. 1-3, pp. 28-34.
- [11] Di Giovannantonio, M., El Garah, M., Lipton-Duffin, J., Meunier, V., Cardenas, L., Revurat, Y.F., Cossaro, A., Verdini, A., Perepichka, D.F., Rosei, F. & Contini, G. 2013, "Insight into Organometallic Intermediate and Its Evolution to Covalent

Bonding in Surface-Confined Ullmann Polymerization", *Acs Nano*, vol. 7, no. 9, pp. 8190-8198.

[12]Stoltze, P. 1994, "Simulation of Surface-Defects", *Journal of Physics-Condensed Matter*, vol. 6, no. 45, pp. 9495-9517.

[13]Ullmann, F. 1904, "Ueber symmetrische biphenyl-derivate", *Justus Liebigs Annalen der Chemie*, vol. 332, no. 1-2, pp. 38-81.

[14]Koch, M. 2013, *Growth and Characterization of Single Molecular Wires on Metal Surfaces*.

[15]Jones, R.G. & Kadodwala, M. 1997, "Bromine adsorption on Cu(111)", *Surface Science*, vol. 370, no. 2-3, pp. L219-L225.

[16]Kittel, C. 2005, "Introduction to Solid State Physics 8th Edition".

Chapter 4

STM, PES and XAS Study of 10,10'-dibromo-9,9'-biantracene (DBBA) on Au(111), Ag(111) and Cu(111) Surfaces

4.1 Introduction

Graphene, first isolated in 2004 by Geim and Novosolov, consists of a single layer of carbon atoms arranged in a regular hexagonal array ^[1]. Due to its high charge carrier mobility, mechanical strength, flexibility and transparency, graphene is a very attractive material for applications in electronics, ultrafast photonics, photovoltaic cells, light emitting devices, touch screen technology and energy storage devices ^[2, 3, 4]. Graphene devices have the potential advantage of being smaller and transmitting data faster, while consuming less energy than the corresponding silicon based components in use today. For example, graphene-based transistors could run at speeds a hundred to a thousand times faster than silicon transistors. However, graphene has one significant disadvantage when compared with the silicon technology; it has no energy band-gap and therefore it cannot be used to make transistors with a sufficient on/off ratio for electronic applications. A considerable research effort has focused on this problem and has demonstrated that a significant energy band gap, inversely proportional to the width of the conducting channel, can be achieved by lateral confinement in graphene nanoribbons (GNR). However, a sufficiently large gap can only be achieved in extremely narrow graphene nanoribbons (typically <10 nm) and this poses a serious technical challenge. Strategies targeted at opening a band-gap in graphene include chemical modification ^[5, 6]; bilayer control ^[7] and unzipping carbon nanotubes ^[8]. Here we show that atomically precise armchair graphene nanoribbons (AGNRs) can be fabricated via thermally induced polymerization and dehydrogenation of the 10,10'-dibromo-9,9'-biantracene (DBBA) on metal surfaces. DBBA is a bromine functionalised organic molecule with chemical formula $C_{28}H_{16}Br_2$. Due to steric repulsion between the hydrogen atoms the two anthracene units are naturally tilted around the central connecting carbon bond as shown in Figure 4.1.

We present a comparative study of the bottom-up growth of 7-AGNRs from DBBA molecular precursors on Au(111), Ag(111) and Cu(111) using scanning tunnelling microscopy (STM), in combination with near-edge X-ray absorption fine structure (NEXAFS) and photoelectron spectroscopy (PES). We report on observed correlations between surface reactivity and growth dynamics of GNRs. Furthermore, we demonstrate that core level spectroscopies can be used as an effective tool for studying the formation of GRNs and complimenting the STM imaging process.

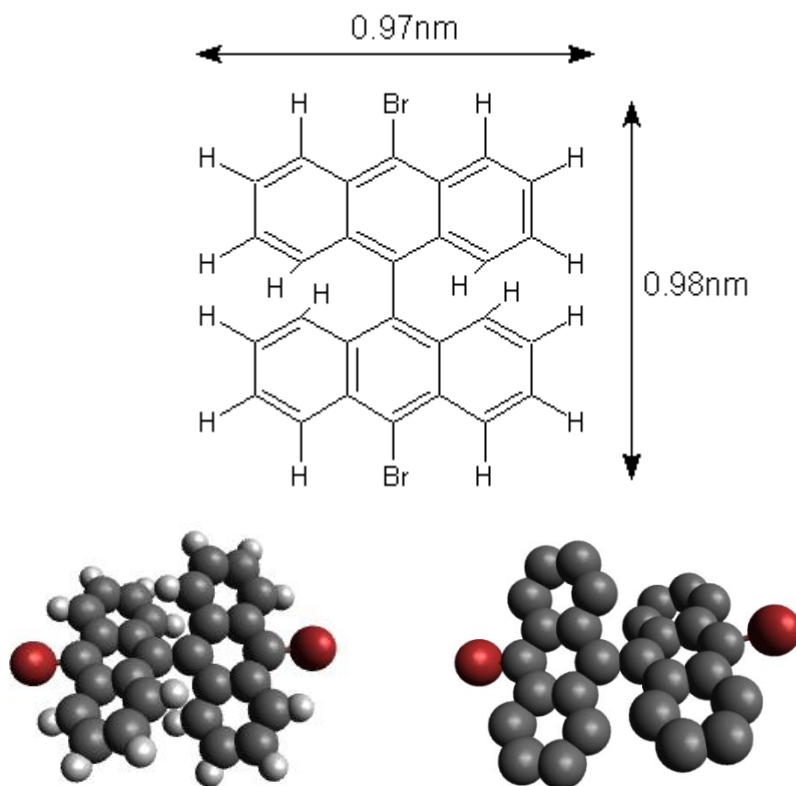
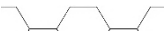
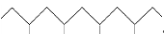


Figure 4.1: Chemical structure of DBBA with dimensions and graphical representation, with and without hydrogens.

Figure 4.2 shows a schematic representation of the chemical reactions which occur during the formation of the GNRs. The first reaction step, debromination, of the DBBA precursor molecule results in an activated molecule (radical) and initiates the formation of a polymerized oligomer chain, i.e. the bromine dissociates and the resulting bi-anthracene molecules can form single covalent bonds. Thermal activation causes dehydrogenation of

the polymerized chains and results in the formation of narrow (7 carbon atoms wide) armchair GNRs (7-AGNRs).

The growth mechanism of GNRs on Au(111) from DBBA precursors is understood, and consists of the initial formation of polyphenylene chains at 200°C followed by cyclodehydrogenation at 400°C [2]. However, the effect of substrate reactivity on the growth and structure of the GNRs remains open to investigation. At room temperature (RT) the DBBA molecules remain intact on Au(111), while on Cu(111) full surface-assisted dehalogenation takes place and chains start to form at RT and elevated temperatures. On Ag(111) the DBBA molecules are partially dehalogenated at RT, thus leading to distinctive and different features in the formation of the GNRs compared to the other two substrates under investigation. GNRs form on Au(111) at 400°C [2], while on the Ag(111) and Cu(111) surfaces the formation of GNRs occurs at 350°C and 250°C, respectively [9]. On Cu(111) the lateral orientation of GNRs appears to be governed by a strong ribbon-substrate interaction which is not observed for weakly-bonded GNRs on Au(111). Moreover, we demonstrate that on Cu(111) the presence of bromine throughout the GNR formation process does not disturb the growth of high-quality GNRs.

In this thesis we show that H-terminated 7-AGNRs can also be grown on an Ag(111) and Cu(111) substrate via a bottom-up approach by using DBBA molecules as a precursor. The ‘7’ refers to the number of carbon atoms across the GNR and the ‘A’ refers to the edge structure of the GNR, in this case, Armchair , as opposed to Zig-zag . Based on a comparison with the analogous process on the Au(111) surface, the effect of the substrate reactivity on the GNRs growth is demonstrated. The combination of STM and core-level spectroscopies proves to be highly informative and contributes considerably to an understanding of GNR formation and structure.

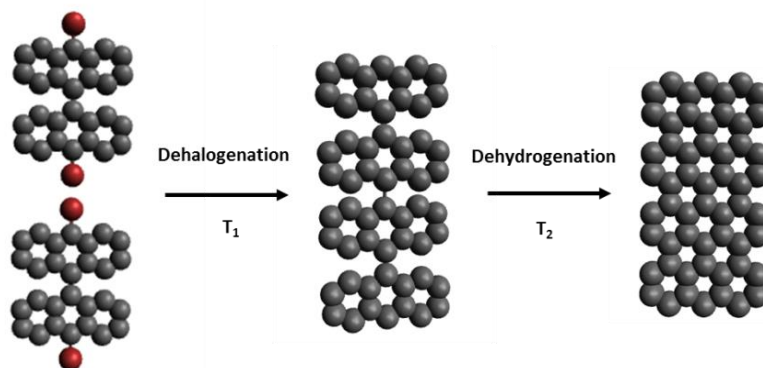


Figure 4.2: Reaction mechanisms showing the formation of 7-AGNRs from DBBA precursor molecules. The intermediate stage is that of a covalently bonded anthracene chain (hydrogen atoms not shown for clarity).

4.2 Formation of GNRs on the Au(111) Surface

0.65ML of DBBA was deposited, for 30 minutes from a Knudsen cell held at 150°C, onto the clean Au(111) surface which was then annealed to initiate the reactions described above. As previously discussed in Chapter 3, room temperature STM imaging of sub monolayer molecular coverages on the Au(111) surface is difficult due to the high molecular mobility and weak molecule-substrate interaction. In this case successful STM imaging of sub-monolayer coverage of DBBA on the Au(111) surface was only possible after thermal annealing to 200°C where the polyanthracene chains are formed as shown in Figure 4.3.

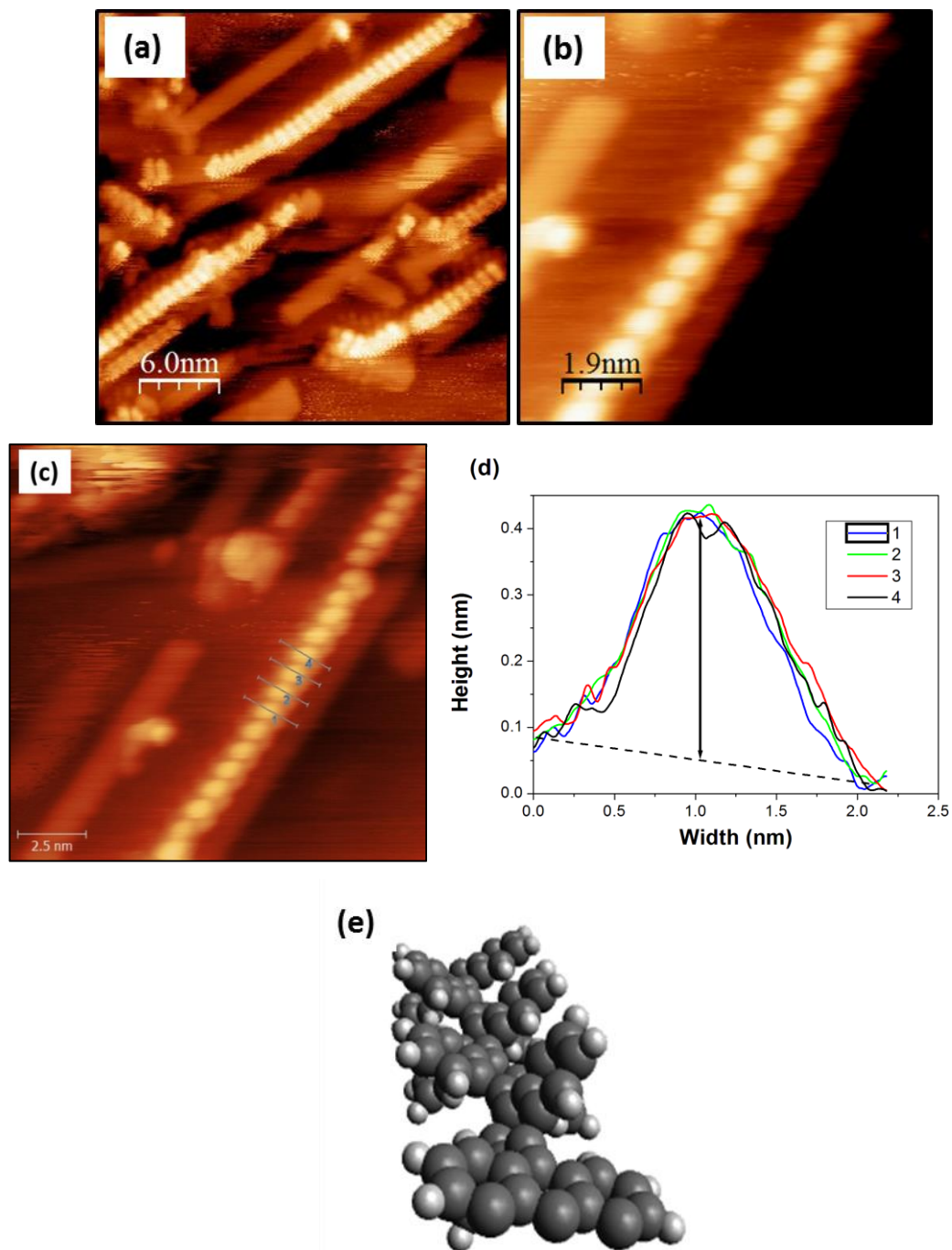


Figure 4.3: STM images of 0.65ML of DBBA deposited onto RT Au(111) and subsequently annealed to 200°C where (b) is a magnified image of the step edge observed in (a), ($V_b = -1.0V$, $I_t = 0.1nA$ and $V_b = -0.3V$, $I_t = 0.04nA$ respectively). (c) Line profiles on same image (d) apparent height of the chains and (e) a graphical representation of a chain showing anthracene tilt. Again, carbon atoms are represented in dark grey and hydrogens in light grey.

Chains of up to 20 nm in length are observed as bright protrusions. The protrusions have a centre to centre distance of 0.86 ± 0.05 nm which is in agreement with a bianthracene to bianthracene distance of 0.91 nm predicted by the simple model in which bromine atoms have dissociated and the molecules have polymerised. It is therefore proposed that at this stage bromine has dissociated from the DBBA molecules and covalently bonded polymerisation has taken place ^[2]. If the chains are lying flat they would have an apparent height of 0.17 ± 0.02 nm (as shown below after GNR formation). The apparent height of the chains here is 0.35 ± 0.02 nm as shown in line profiles in Figure 4.3 (d) thus confirming that the anthracene chains are tilted with respect to the Au(111) surface, Figure 4.3 (e). Steric hindrance between the hydrogen atoms of adjacent anthracene subunits induces rotation around the connecting carbon-carbon bond which leads to this tilting effect and the larger than expected apparent height. An angle of 33° between the anthracene plane and surface normal has been reported by Klues *et al.* ^[10]. This would equate to an alternating tilt elevation above the surface of 0.42 nm, comparable to the 0.35 nm observed here.

As shown below, intramolecular cyclodehydrogenation occurs when the system is annealed to 400°C , resulting in atomically precise 7-AGNRs with hydrogen terminated edges. Large scale and magnified STM images of the 7AGNRs and a model are shown in Figure 4.4.

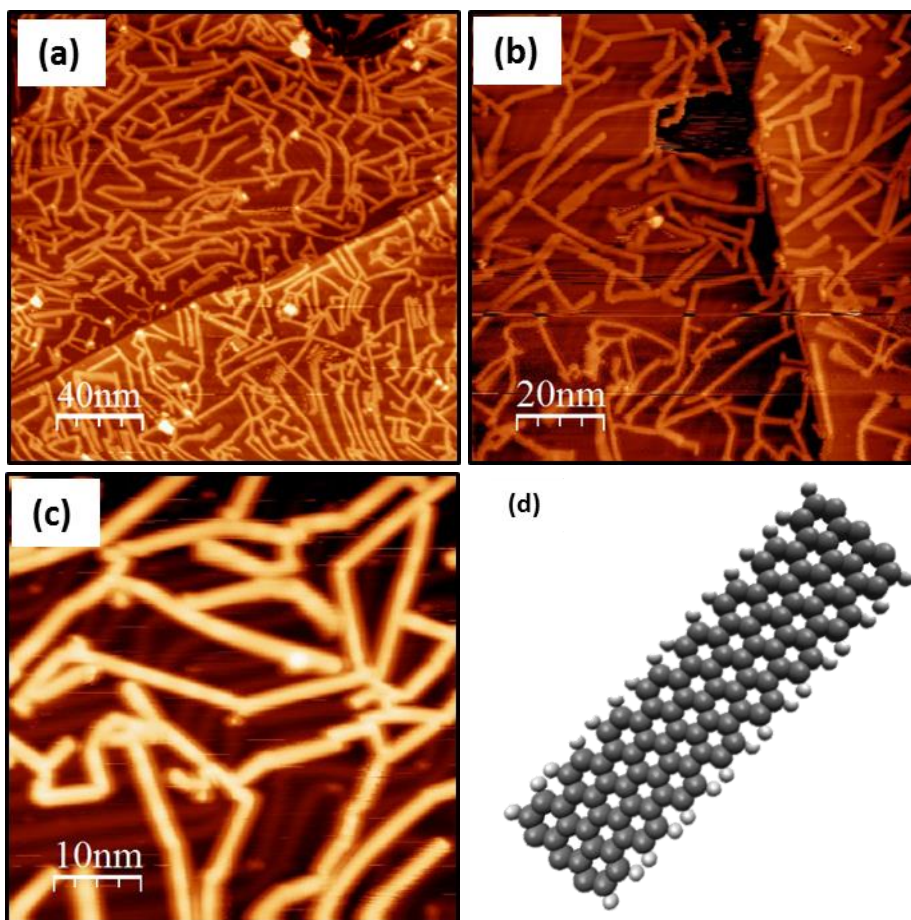


Figure 4.4: STM images of approximately 0.65ML of DBBA deposited onto RT Au(111) and then annealed to 400C, (a) large scale image, (b) and (c) further magnifications where the herringbone is still apparent (4.4 (c)), ($V_b = -1.37V$, $I_t = 0.1nA$), and (d) Graphical representation of an isolated 7-AGNR with hydrogen terminated edges (carbon atoms in dark grey, hydrogen atoms in light grey).

Figure 4.5 shows a histogram of the length distribution of the GNRs. The data in this figure are obtained by measuring the lengths of individual GNRs on a series of 100×100 nm STM images. Also shown in Figure 4.5 is a fit to the data using an ‘Extreme Peak Function’ in MicroCal Origin ^[11]. From this fit it is determined that the average chain length is 18 ± 1 nm, while chains with lengths in excess of 60 nm are observed.

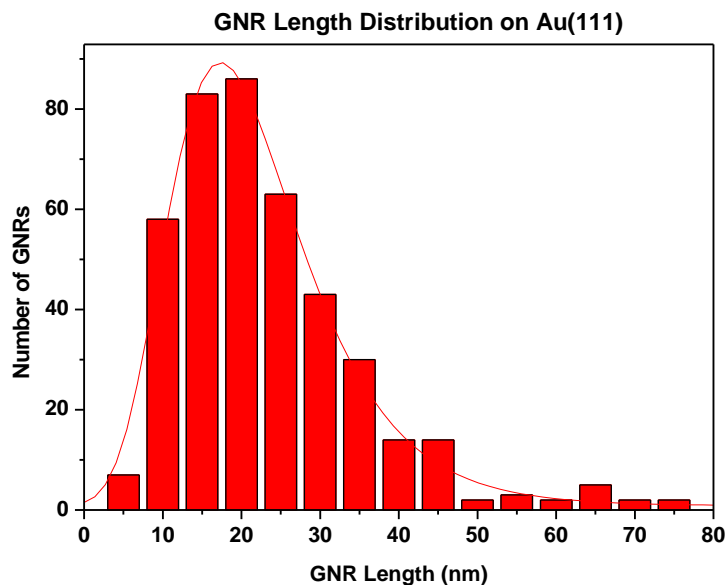


Figure 4.5: GNR length distribution when grown on the Au(111) substrate.

The Fast Fourier Transform (FFT) taken from Figure 4.4 (a) and shown in Figure 4.7 confirms the random orientation of the GNRs on the Au(111) surface. This suggests that there is little interaction between the GNRs and the underlying Au substrate. The multidirectional branching is most probably caused by cyclodehydrogenation between neighbouring GNRs, i.e. dehydrogenation can occur at the edges of the GNRs. Measurements of the widths of the GNRs averaging over multiple nanoribbons, show the average width to be 1.32 ± 0.05 nm. This is wider than expected since the corresponding molecular model predicts a width of 0.97 nm between hydrogen atoms on opposite sides of a DBBA molecule as shown in Figure 4.1. This larger measured width can be attributed to a resolution effect due to the finite size of the STM tip. The apparent height has approximately halved, from a value of 0.35 ± 0.02 nm for the chains to 172 ± 14 pm for the GNRs, Figure 4.6.

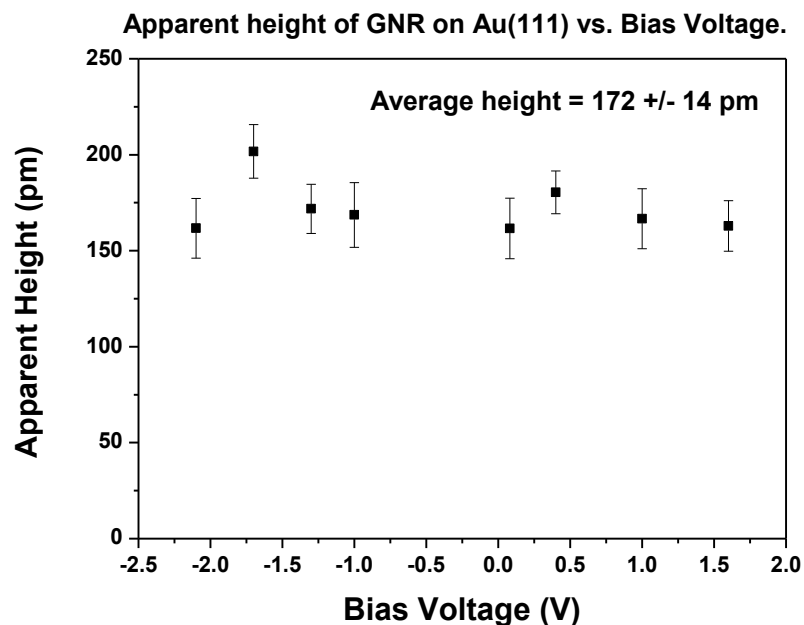


Figure 4.6: Apparent GNR height on the Au(111) surface at varying voltages. Discrepancies in errors are due to number of ribbons sampled per bias voltage investigated.

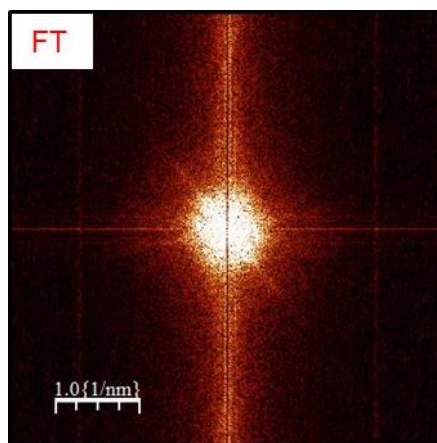


Figure 4.7: Fast Fourier Transform (FFT) of GNRs on Au(111) indicating possible preferential directional GNR growth (processed using the STM image in Figure 4.4 (a)).

In order to gain more understanding of the chemistry involved in GNR formation Br 3d PE spectra were recorded as a function of annealing temperature as shown in Figure 4.8.

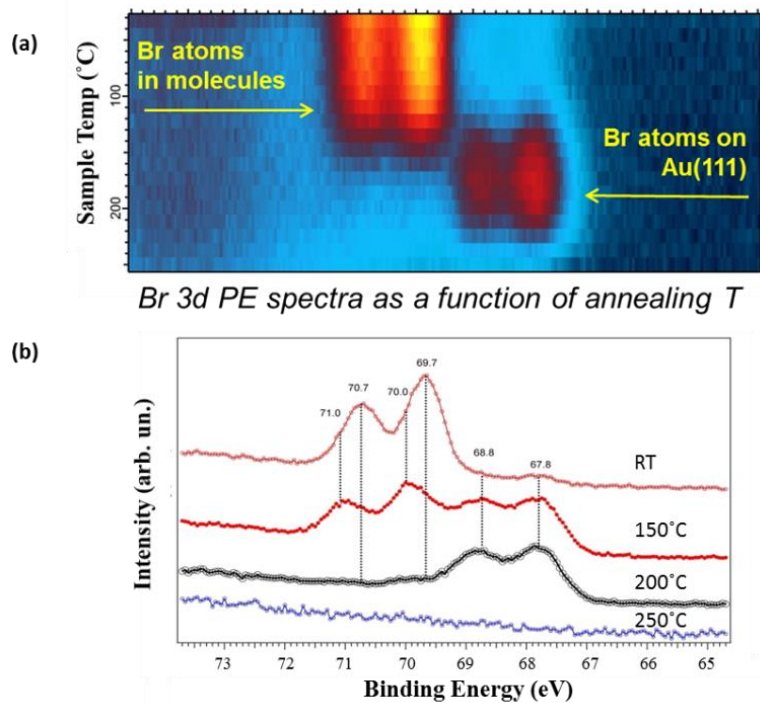


Figure 4.8: Evolution of the Br 3d PE spectra of DBBA/Au(111) as a function of sample temperature. $h\nu = 170\text{eV}$. (a) Intensity map of Br 3d signal from the Au(111) substrate as a function of temperature and (b) specific temperature PES.

The Br 3d PE spectra undergo significant changes upon annealing. Below 100°C the signal comprises two broad spin-orbit doublets with binding energies of the Br $3d_{5/2}$ at 70.0eV and 67.8eV . The separation between the spin-orbit split components is 1eV . The position of the 70.0eV line coincides with that of a thick layer of DBBA on Au(111) (not shown) and can therefore be attributed to Br atoms bonded to the DBBA molecule on the second layer. The shoulders which are present at higher binding energy of 70.0eV and 71.0eV can be attributed to molecular bromine which is on the first layer i.e. closest to the Au surface. Therefore, the position of the 67.8eV line is attributed to atomic bromine on the Au(111) surface indicating that debromination has initiated at RT. Upon annealing to 150°C , the peak at 69.7eV has decreased in intensity indicating that the second layer has desorbed. In contrast, the spin-orbit split component of the Br $3d_{5/2}$ peak with binding energy at 67.8eV increases as further debromination occurs i.e. more atomic bromine is present on the surface. The increase in this component is associated with the enhanced doublet (previously

shoulder) at 70.0eV. At 200°C the atomic bromine peak is still observed while the intensity of the molecular bromine doublet is negligible. Together with previously published reports [2], this confirms that molecular biradicals can form polymerised chains at 200°C on the Au(111) surface. This claim is enhanced by the STM images shown in Figure 4.4. All of the bromine species have desorbed from the surface after the sample is annealed to 250°C. The intensity of the Br 3d peak after the 200°C anneal is significantly less than that measured at RT. This can be explained by desorption of bromine from the surface after debromination from the DBBA molecule.

Figure 4.9 shows the C 1s PE spectra recorded at increasing anneal temperatures. At each stage of the annealing process, changes are observed which reflect the chemistry occurring on the surface.

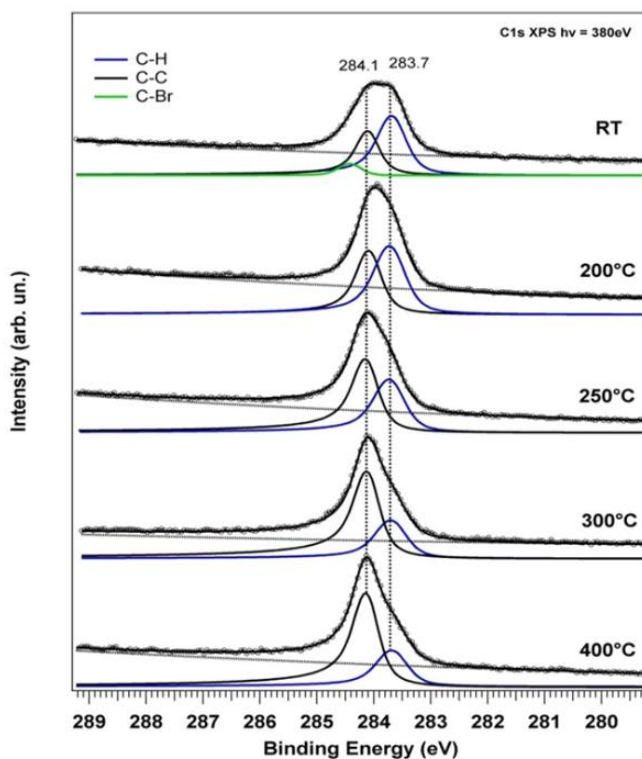


Figure 4.9: Evolution of the C 1s PE spectra of DBBA/Au(111) as a function of sample temperature. $h\nu = 380\text{eV}$.

There are three distinct chemical environments for the C atoms in the DBBA molecule as shown in Figure 4.1: there are 10 sp^2 coordinated carbon atoms with three neighbouring carbons [C-C], 16 carbons bonded to two adjacent carbon atoms and a hydrogen atom

[C-H] and 2 carbon atoms bonded to bromine [C-Br] . The C 1s spectra exhibit two significant peaks through all anneal stages with binding energies of 283.7eV and 284.1eV which correspond to the C-H and C-C contributions respectively. At RT an additional peak at high binding energy (284.4eV) is observed and is attributed to the two carbon atoms which are bonded to bromine. This component appears at high binding energy due to the bond with the more electronegative bromine atom. At RT, the C-H component dominates the spectrum (57%) as expected from the 16 : 10 : 2 ratio of C-H : C-C : C-Br in the DBBA molecular model. The C-C and C-Br environments contribute 35% (10 atoms) and 8% (2 atoms) respectively of the total signal, confirming the expected 16 : 10 : 2 ratio from the atomic model and confirming also that the molecules remain intact and brominated upon RT deposition. At 200°C, loss of the C-Br component is observed together with an increase in the intensity of the C-C component relative to that of the C-H component. New C-C anthracene linking bonds are formed resulting in a new ratio of 16 : 12 : 0 thus confirming that debromination has taken place and polyanthracene chains have formed. This is confirmed since 57% (16) of the signal is attributed to the unaltered C-H bonds but the contribution from the C-C bonds increases to 43% (12). Further annealing produces a decrease in the C-H intensity with a corresponding increase in the C-C component until at 400°C, the C-C intensity dominates and comprises 69% of the total signal, the remainder being attributed to the C-H bonds along the edges of the ribbons. This decrease in the intensity of the C-H component is a result of cyclodehydrogenation. A final C-H : C-C ratio of 9 : 19 is measured and GNR formation is complete. The expected ratio for a GNR from the molecular model is 8 : 20, in close agreement with the experimental findings. A summary of these ratios at each stage is given in Table 4.1. Taking the PE spectra for both bromine and carbon into consideration, it can be concluded that transformation of RT deposited DBBA molecules into molecular chains occurs at 200°C and H-terminated 7-AGNRs are formed at 400°C.

Au(111)			
	<u>C-C (%)</u>	<u>C-H (%)</u>	<u>C-Br (%)</u>
Molecule	35 (36)	57 (57)	8 (7)
Chain	43 (43)	57 (57)	0 (0)
7-AGNR	69 (71)	31 (29)	0 (0)

Table 4.1: Percentage intensities of the C 1s components during the evolution of DBBA molecules to GNRs on the Au(111) surface. Values in brackets are the expected values from the molecular model.

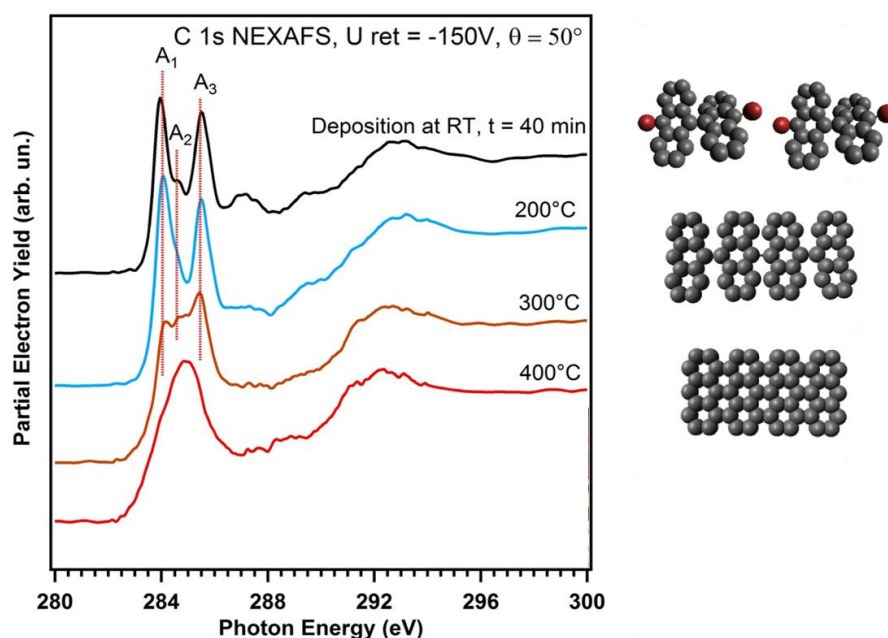


Figure 4.10: XAS spectra of DBBA on Au(111) showing successive anneal stages and schematic showing the chemical alterations when increasing the anneal temperature.

GNR formation on Au(111) was further characterised by XAS measurements as a function of annealing temperature, Figure 4.10. Annealing the Au(111) surface, from RT to 400°C, with approximately one monolayer of DBBA molecules adsorbed results in changes in the near edge fine structure region of the spectra. The changes observed indicate progressive alterations in the electronic structure and orientation of the molecules. The XAS spectra of the DBBA molecules adsorbed and annealed on the Au(111) surface exhibit features similar to those recorded from other polyanthracene molecules ^[10, 12, 13, 14, 15]. The π^* region

of the spectrum consists of three resonances $A_1 - A_3$. These features are caused by the C 1s to π^* transitions into the three lowest unoccupied DBBA molecular orbitals ^[10]. The same energy interval in NEXAFS spectra of a single anthracene molecule has only two resonance peaks A_1 and A_3 corresponding to the C 1s $\rightarrow \pi^*$ transitions into the two lowest unoccupied molecular orbitals ^[16]. Peak A_2 in the RT spectrum is attributed to the carbon atoms which are bonded to bromine atoms. This peak is observed to decrease upon annealing to 200°C. At this stage, the XA spectrum is almost identical to that of anthracene where a shift of A_2 towards A_1 has occurred ^[16]. This is expected due to debromination and subsequent polyanthracene chain formation. The spectrum at 300°C shows a broadening of the A_1 and A_3 peaks associated with a delocalisation of the electrons along the polymer chain. At 400°C debromination and cyclodehydrogenation are complete. The small component in the PES spectra at low binding energy is still attributed to carbon/hydrogen (C-H) bonds which are found along the edges of the GNRs. This broadening of all three carbon species into a single broad band and smaller C-H component indicates a delocalised π^* system indicative of planar GNR formation.

4.3 GNR Formation on the Ag(111) Surface

STM images shown in Figure 4.11 (a) and (c) shows the room temperature self-assembled arrangement of DBBA molecules on the Ag(111) surface. The Fourier transform of Figure 4.11 (a) (shown in Figure 4.11 (b)) shows the alignment of the DBBA molecules on the Ag(111) substrate with a periodicity of $1.30 \pm 0.10\text{nm}$.

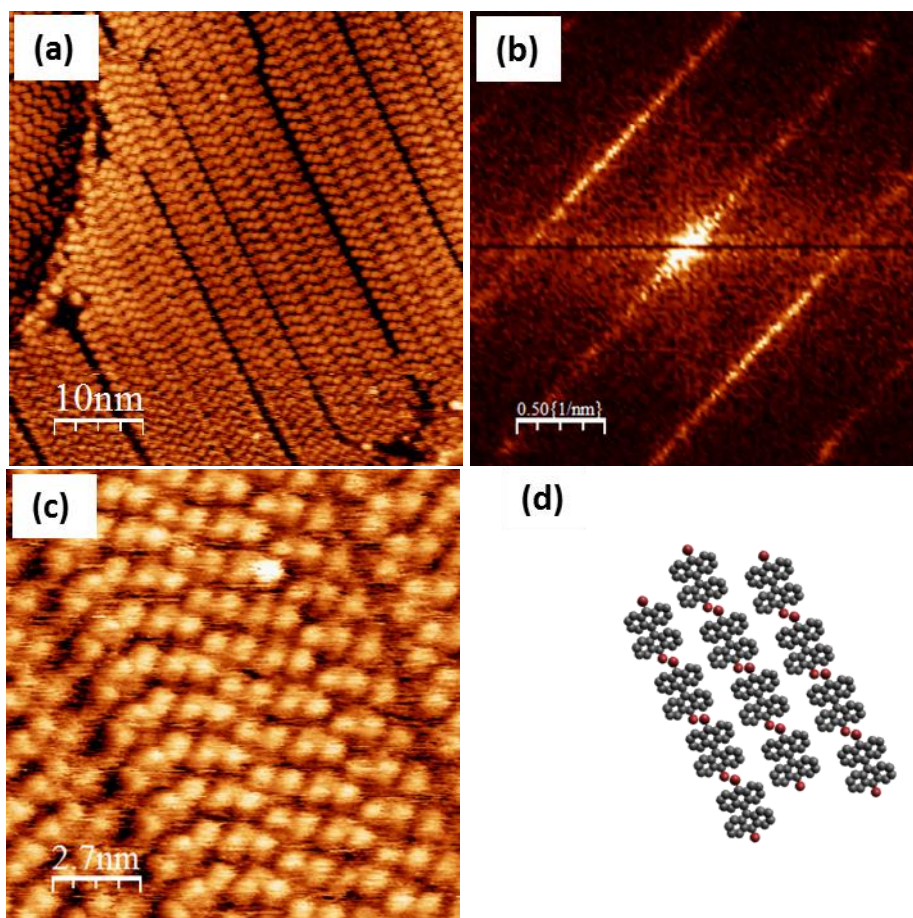


Figure 4.11: STM images (a) and (c) showing the alignment of DBBA chains on the RT Ag(111) surface ($V_b = -1.05\text{V}$, $I_t = 0.07\text{nA}$) and ($V_b = 1.07\text{V}$, $I_t = 0.08\text{nA}$) respectively, (b) shows the FFT which aids periodicity measurements and (d) is schematic of DBBA deposited onto the Ag(111) surface.

The DBBA molecules align in three directions on the Ag(111) substrate at 120° to each other where a single molecular row is $1.31 \pm 0.05\text{ nm}$ wide. The rows lie side by side with missing rows which are between 0.6 nm and 1.0 nm in width. These gaps could be caused

by dissociated bromine still present on the surface or to relieve strain in the molecular domains.

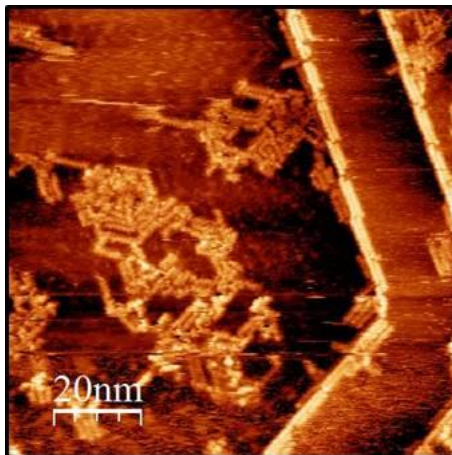


Figure 4.12: STM image of DBBA deposited onto the Ag(111) surface after annealing to 150°C, ($V_b = 2.05V$, $I_t = 0.02nA$)

Annealing to 150°C causes polyanthracene chains to form as shown in Figure 4.12. This temperature was chosen since the forthcoming bromine 3d and carbon 1s PES data (shown in Figures 4.15 and 4.16) indicate the formation of chains between 100°C and 200°C. The chains appear as islands, randomly orientated on the surface while longer chains are observed along the step edges. This is usually the case due to the higher catalytic activity of the silver adatoms at the step edges. The PES data, most notably from the C 1s spectra (Figure 4.16), indicates that GNR formation should occur between 300°C and 400°C. Figure 4.13 shows STM images of the surface after annealing to 370°C. GNRs are observed with no directional preference which is verified by the FFT image.

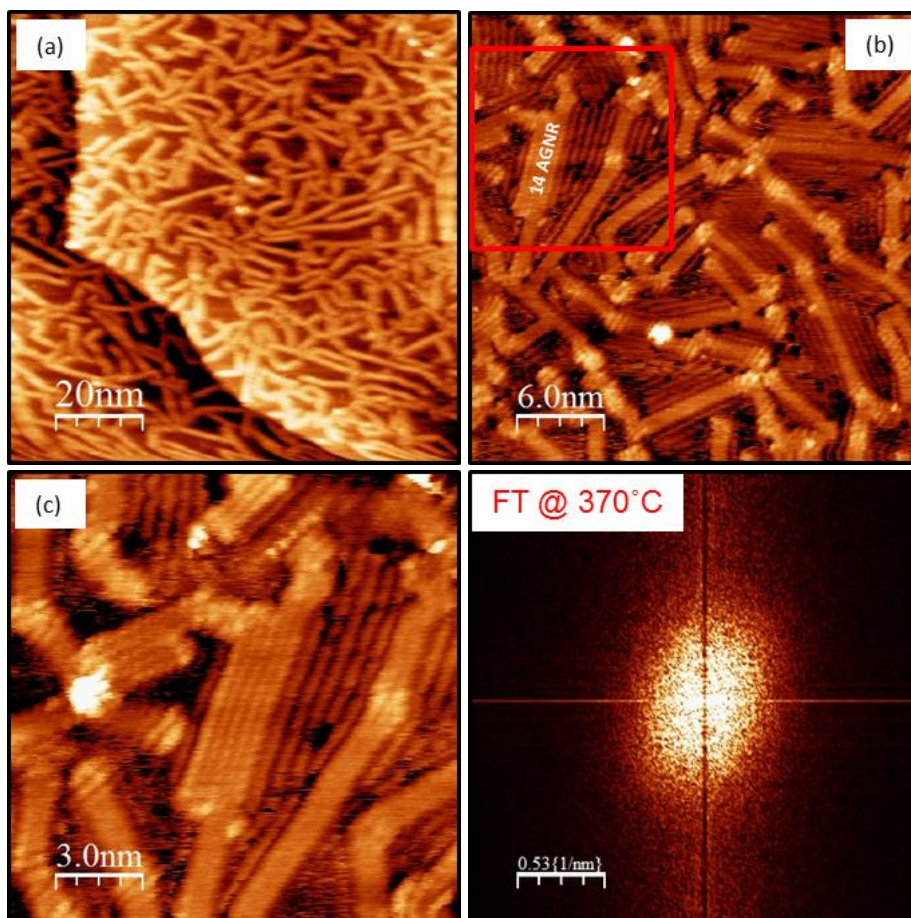


Figure 4.13: GNRs on the Ag(111) surface taken after annealing to 370°C. (a) large scale multi-directional GNRs, ($V_b = 1.23V$, $I_t = 0.10nA$), (b) high resolution image where a 14-AGNR is highlighted and Ag reconstruction is visible, ($V_b = -0.41V$, $I_t = 0.05nA$), (c) the magnified region from the red square in Figure 4.16 (b), ($V_b = -0.32V$, $I_t = 0.05nA$) and corresponding FFT at 370°C showing no preferential directional GNR growth.

Randomly orientated GNRs are distributed on the Ag(111) substrate with uninterrupted lengths of up to 20 nm. For most ribbons, line profiles provide an apparent GNR height of 90 ± 10 pm and width of 0.96 ± 0.02 nm. However occasionally ribbons with widths of 2.11 ± 0.02 nm are observed. This occurs in dense areas of GNR formation and results from cross dehydrogenation between adjacent single 7-AGNRs, resulting in 14-AGNRs, highlighted in Figure 4.13 (b) and magnified in (c). The width of a 14-AGNR, determined from the molecular model shown in Figure 4.14, is 1.87 nm which is in agreement with the STM measurements mentioned above (2.11 ± 0.05 nm). As before, the finite tip size must be considered when measuring these values. The row-like features observed between the GNRs could be a 2×1 reconstruction of the Ag(111) surface with a periodicity of

0.57 ± 0.05 nm in agreement with the expected periodicity of 0.578 nm for the Ag(111)-(2 × 1) reconstruction. A similar reconstruction of the substrate was observed previously for nano-networks formed on the Au(111) and Cu(111) surfaces where the alignment of the reconstructed atomic domains are aligned at 60° relative to each other^[17, 18]. No such alignment is observed for the structure here, where the direction of the atomic rows appears to be dictated by the orientation of the GNRs. A possible explanation is that the presence of the GNRs induces a surface relaxation of the silver atoms to relieve strain imposed by the molecules. Brighter areas of the GNRs are observed at the termination points and at certain junctions in relation to the body of the ribbons, implying a higher charge density in these regions. This is in agreement with STM images of GNRs on the Au(111) surface and also with DFT calculations reported in the literature^[2, 19]. It is possible that the growth of GNRs on the Ag(111) induces surface electrons to be confined between ribbons creating these features observed even whilst scanning at RT (expected at lower temperatures). It would be expected that scanning these regions under different bias conditions would alter the periodicity of the rippling and provide a more conclusive answer. Without this additional data, both possibilities are plausible.

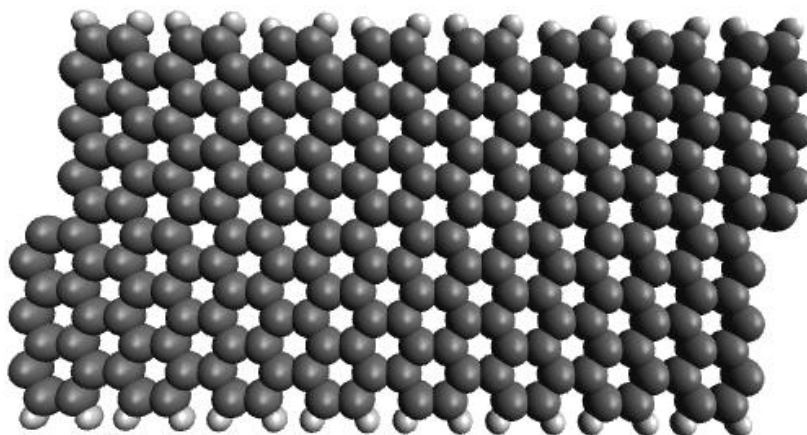


Figure 4.14: Graphical representation of a 14-AGNR formed through cross dehydrogenation between adjacent 7-AGNRs. Carbons are shown in dark grey and hydrogen atoms, in light grey, are still present at the edges of the 14-GNR.

Figure 4.15 shows the temperature dependent Br 3d PES spectra data measured after deposition of 0.6ML of DBBA on the Ag(111)-(1 × 1) surface held at room temperature and subsequently annealed to 400°C. At RT two doublets are present. The high binding

energy doublet ($3d_{5/2} = 70.6\text{eV}$) and low binding energy doublet ($3d_{5/2} = 68.3\text{eV}$) and are attributed to molecular bromine and dissociated bromine respectively. The doublets have a spin orbit splitting of 1.0eV . As with HBTP on Ag(111), partial debromination has taken place at RT with approximately 50% of the Br atoms dissociated from the DBBA molecule. Annealing to 100°C dissociates additional bromine from the molecule on to the surface. At 200°C the bromine is totally dissociated from the molecule. After a 400°C anneal the bromine is completely desorbed from the Ag(111) surface.

Since the formation of DBBA chains and subsequent GNR creation on the Au(111) substrate occurs at 200°C and 400°C respectively, it is expected that these processes should occur more readily on the Ag(111) surface due to its greater reactivity.

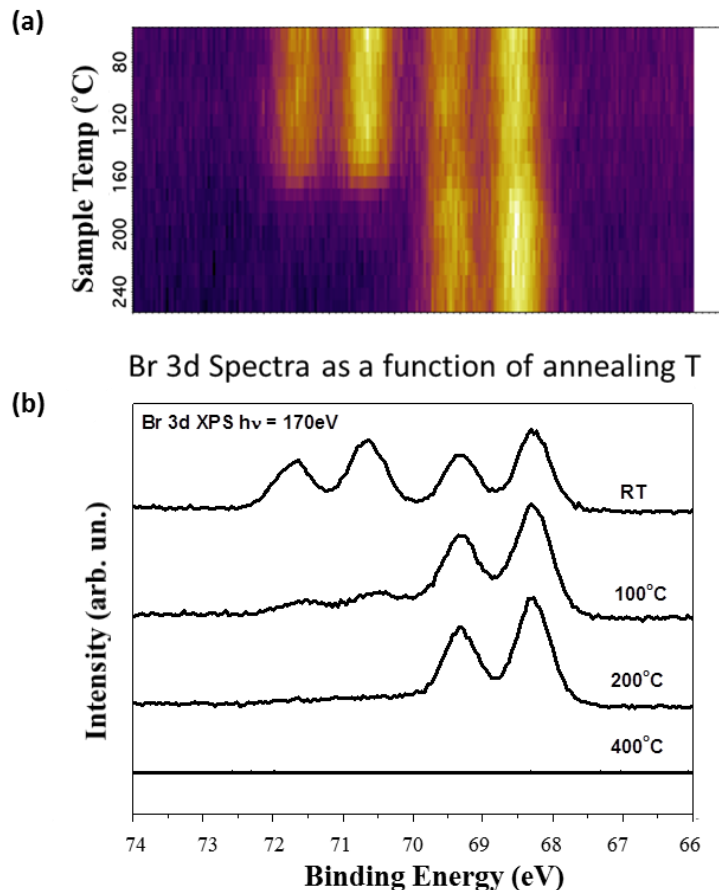


Figure 4.15: Evolution of the Br 3d PE spectra of DBBA/Ag(111) as a function of increasing sample temperature. $h\nu = 170\text{eV}$. (a) Intensity map of Br 3d signal from the Ag(111) substrate as a function of temperature and (b) PES taken at specific temperatures.

Similar to the DBBA/Au(111) analysis, the high binding energy doublet is assigned to molecular bromine (~50% of the total signal intensity) while the low binding energy doublet here (~50% of the total signal intensity) is assigned to atomic bromine on the Ag surface which has dissociated from the molecule. Therefore, it is proposed that one bromine atom per molecule has dissociated from the molecule but remains on the Ag(111) surface when DBBA is deposited at RT. It is possible that the molecule is adsorbed via one of the bromine atoms but the reason for this is not fully understood and requires DFT calculations for additional insight. The Br 3d spectra indicate that polyphenylene chains form between RT and 100°C due to debromination and radical addition. At the 100°C anneal stage, 84% of bromine has transferred from the molecule to the surface, indicating that neighbouring molecules possessing this free radical may be able to link together in a covalent fashion. At 200°C 100% of bromine is dissociated from the molecule and upon annealing to 400°C desorption of the Br from the surface is complete.

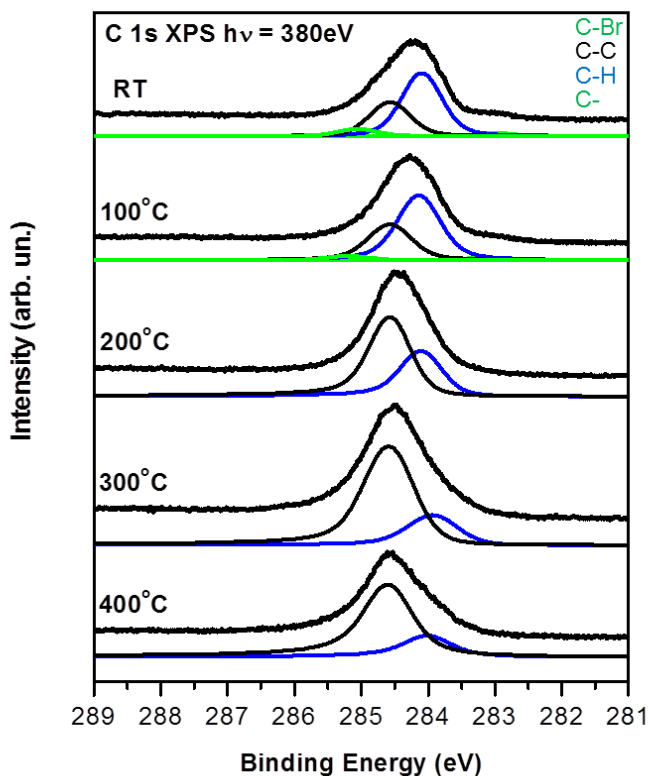


Figure 4.16: Evolution of the C 1s PE spectra of DBBA/Ag(111) as a function of increasing sample temperature. $h\nu = 380\text{eV}$.

Figure 4.16 shows a series of C 1s PE spectra for DBBA deposited onto Ag(111) and subsequently annealed. Comparing the room temperature C 1s spectra from DBBA on the Ag(111) surface with the corresponding PE spectrum for the Au(111) surface reveals two small components at binding energies of 285.1eV and 283.0eV. These are attributed to the C-Br and carbon radical species respectively. This is further evidence that partial debromination has occurred at RT. At 100°C additional debromination occurs as a decrease in intensity is observed in the bromine constituent in the C 1s spectra. At 200°C both the carbon radical and carbon bromine components have disappeared. Again analysing the 100°C and 200°C spectra, there is a decrease in the C-H component (284.1eV) and a corresponding increase in the C-C component (284.6eV). This indicates that polymer chains are formed between these anneal stages. As the C 1s spectra develops further to 300°C and then 400°C, cyclodehydrogenation becomes apparent by another transfer of intensity in PES components from C-H bonds to C-C bonds where GNR formation has begun at 300°C and completes at 400°C. Measured intensities of the C-H : C-C : C-Br : C* components in the RT spectrum are in the ratio of 59% : 32% : 5% : 4% which agrees closely with expected ratio of 16 : 10 : 1 : 1, assuming partial debromination has occurred. At 200°C, all C-Br and carbon radical components are gone and if a polymer chain exists at this stage, the expected C-H : C-C ratio should be 16 : 12. Experimental data provides a ratio of 62% : 38% (17 : 11). When cyclodehydrogenation occurs an experimental ratio of 23% : 77% (6 : 22) is measured which is in disagreement with the expected ratio of 8 C-H bonds to 20 C-C bonds, i.e. graphene nanoribbons. This discrepancy in calculated ratios can be explained by the formation of 14-AGNRs (see Figure 4.13 (b) and (c)). This loss of hydrogen occurs due the cross dehydrogenation process between adjacent 7-AGNRs discussed previously. A summary of these ratios can be found in Table 4.2.

Ag(111)			
	<u>C-C (%)</u>	<u>C-H (%)</u>	<u>C-Br (%)</u>
Molecule*	32 (36)	59 (57)	9 (7)
Chain	37 (43)	63 (57)	0 (0)
7/14-AGNR	77 (71)	23 (29)	0 (0)

*Table 4.2: Percentage intensities of the C 1s components during the evolution of DBBA molecules to GNRs. Values in brackets indicate expected values. * Partially debrominated molecules.*

A series of C K-edge x-ray absorption spectra for DBBA on Ag(111) are shown in Figure 4.17. The spectra show similar behaviour to the GNRs on the Au(111). The π^* region of the spectrum consists of three resonances $A_1 - A_3$ associated with the C 1s to π^* transitions into the three lowest unoccupied DBBA molecular orbitals ^[10]. Peak A_2 in the RT spectrum is attributed to the carbon atoms which are bonded to bromine atoms. The A_2 peak in the Ag(111) spectrum is weaker than the equivalent peak in the Au(111) surface. A broadening of the peaks is observed at 100°C where the A_2 peak shifts to a lower binding energy, beginning to merge with A_1 . By 300°C the spectra show further broadening, indicating that cyclodehydrogenation is taking place and the molecules are developing into a planar configuration with respect to the Ag(111) surface. At 400°C the evolution to GNRs is complete. The XAS and STM data shown previously, together with the Br 3d and C 1s PE spectra analysis, show that polymer chains of anthracene form between 100°C and 200°C, (as opposed to 200°C on the Au(111) surface), and GNRs form between 300°C and 400°C on the Ag(111) surface, (as opposed to 400°C on the Au(111) surface).

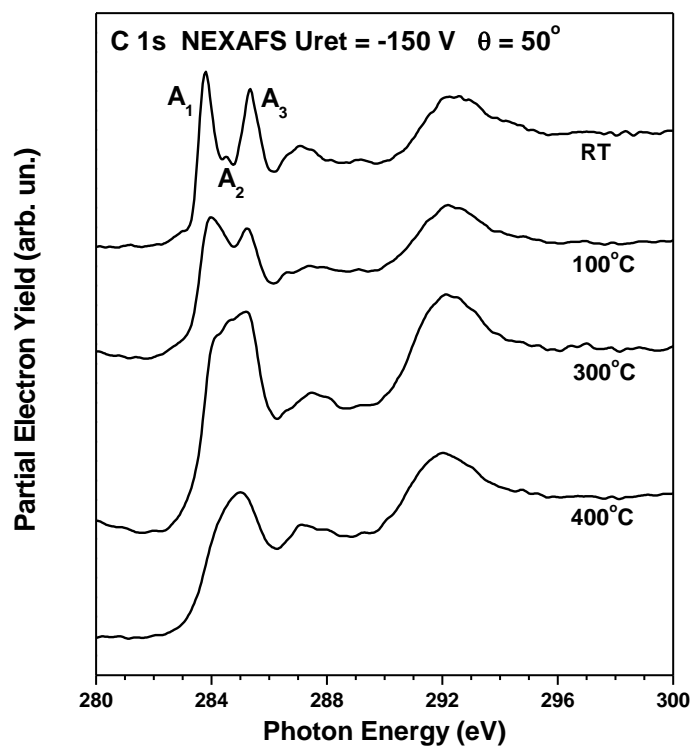


Figure 4.17: XAS spectra of DBBA on Au(111) showing successive anneal stages.

4.4 Formation of GNRs on the Cu(111) Surface

Approximately 0.8ML of DBBA was deposited onto the clean Cu(111) surface at room temperature and subsequently annealed at increasing temperatures. The STM image shown in Figure 4.18 shows the formation of polyanthracene chains on the Cu(111) surface.

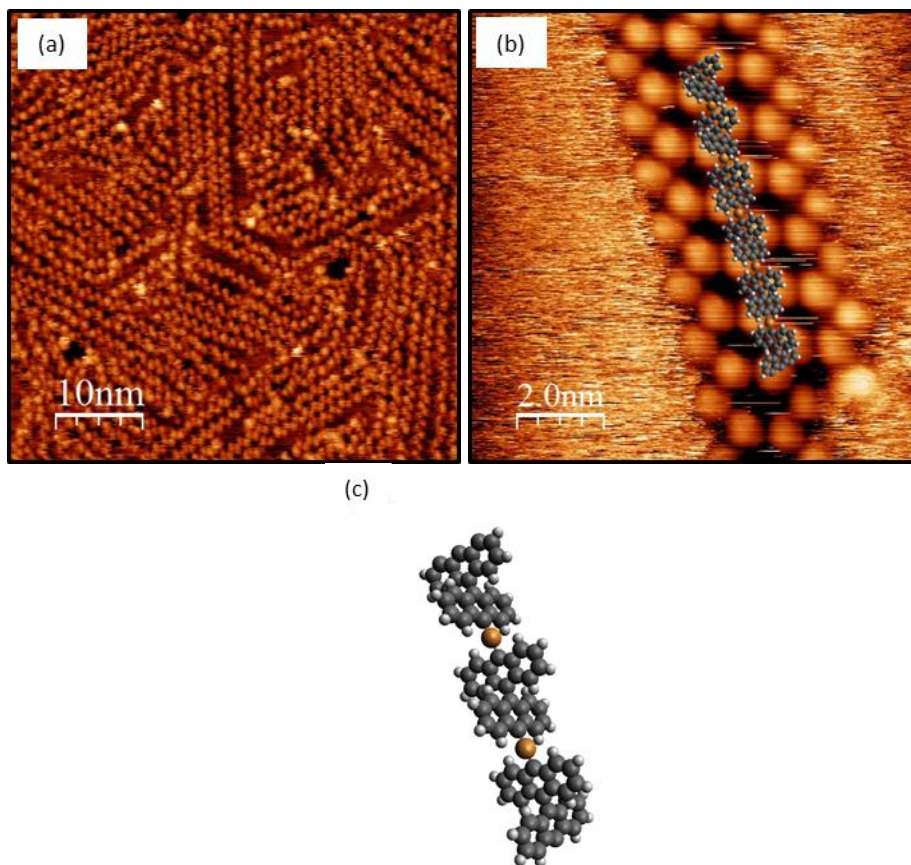


Figure 4.18: High density and magnified areas ((a) and (b) respectively) of DBBA molecular chains deposited at RT with graphic showing how the chains align in (b) ($V_b = -1.0V$, $I_t = 0.1nA$) and ($V_b = 0.23V$, $I_t = 0.02nA$). An enhanced graphical representation of these chains exhibiting the tilt due to steric hindrance and copper atoms between DBBA molecules is shown in (c).

Polymer chains are observed after depositing onto the Cu(111) surface at RT as shown in Figure 4.18 (a). Bright lobes are visible at both sides of the chain axis in a zig-zag pattern, clearly indicating an alternating out of plane tilt of adjacent anthracene subunits, Figure 4.18 (b) and (c). The apparent height of these lobes is 0.18 ± 0.02 nm. The distance between the centres of neighbouring rows is 1.45 ± 0.05 nm which is larger than expected

but hydrogen repulsion along the chain edges can account for this larger separation. The carbon-carbon bonding observed between chains of polymerised DBBA on the Au(111) surface resulted in a centre to centre distance of 0.86 ± 0.05 nm which agrees with the model value of 0.91 nm. Here on the Cu(111) surface, measurements of 1.20 ± 0.10 nm were made between neighbouring DBBA units, which is 32% larger than the expected value from the atomic model if a C-C bond acts as the link. This would suggest that the free radicals formed after debromination, interact with copper adatoms to form a stable intermediate organo-metallic phase which can induce a lateral geometrical distortion in the chains (see graphic in Figure 4.18 (b) and for clarity in Figure 4.18 (c))^[20, 21, 22, 23, 24]. The atomic model predicts a centre to centre DBBA distance of 1.11 nm if a copper adatom inter molecular connection is in place. Therefore, this enlarged distance between DBBA subunits in the chains on Cu, when compared to Au, can be attributed to the formation of a C-Cu-C bond. Direct STM evidence of this organo-metallic bonding is observed when DBBA is deposited on the Cu(110) surface (see Chapter 5) and when DBDPP is deposited on the Cu(111) surface (see Chapter 6). This bonding configuration is enlarged once more in Figure 4.19 where hydrogen atoms have been omitted for clarity. These tilted chains with C-Cu-C bonding configuration probably align in the main Cu(111) crystallographic directions (Figure 4.21) as FFT and STM analysis suggests. The uninterrupted linear polymerised chains exhibit lengths of up to 25 nm and kinked/curved chains are observed up to 50 nm long.

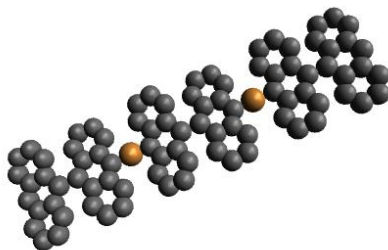


Figure 4.19: Graphical representation of organo-metallic bonding between sequential DBBA units. Carbon atoms are grey, copper atoms metallic in colour and hydrogen atoms are omitted for clarity.

These curves can be attributed to rotation between anthracene subunits around the proposed C-Cu-C bond. Figure 4.20 (a) shows a large scale STM image which highlights the directionality of chain formation.

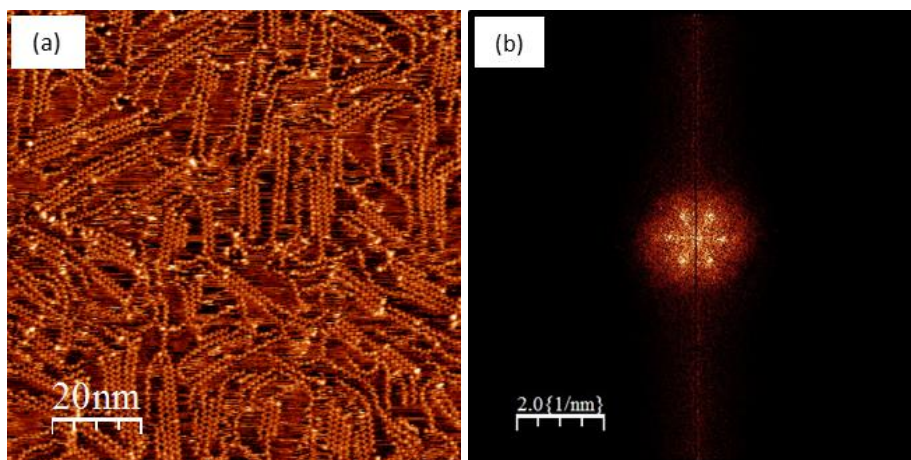


Figure 4.20: (a) Large scale image of covalently bonded anthracene chains formed from deposition of DBBA on the Cu(111) substrate held at RT ($V_b = -0.61V$, $I_t = 0.09nA$). (b) FFT taken from Figure 4.20 (a) of the chains on Cu(111) indicating three preferential growth directions.

The chains exhibit the brightest contrast at the ends of the polymers which is probably due to a copper termination or strong interaction with the substrate. The FFT of the STM image in Figure 4.20 (a), shown in Figure 4.20 (b) confirms that there are three preferential growth directions at 120° to each other. The chain growth probably align in the principle crystallographic directions of the Cu(111) surface as shown in Figure 4.21.

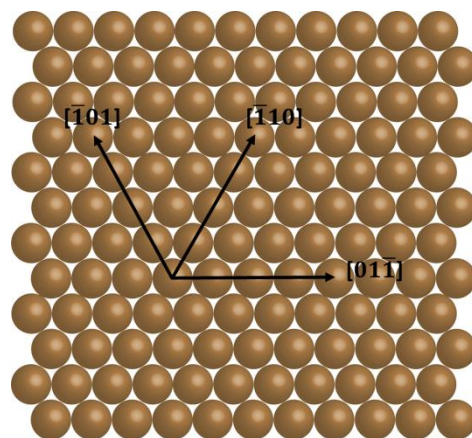


Figure 4.21: Principal crystallographic directions of the Cu(111) surface and the directions of anthracene chains.

Annealing to 200°C causes a cyclodehydrogenation reaction, i.e. internal molecular dehydrogenation, and the formation of 7-AGNRs which are parallel to the Cu substrate, Figure 4.22. The average width the GNRs is 1.35 ± 0.05 nm. Again, the difference between this measured value and the predicted model width of 0.97 nm is attributed to the finite tip size and hydrogen terminated edges. The average length of the GNRs is 12.5 ± 1.0 nm which suggests that the longer chains observed in Figure 4.18 (a) and Figure 4.20 (a) are broken during the cyclodehydrogenation and GNR formation processes. The GNRs grow side by side in parallel rows, typically three or four together. Centre to centre separation between neighbouring ribbons is 1.42 ± 0.02 nm. It is interesting that these 7-AGNRs in close proximity to each other do not dehydrogenate along adjacent edges forming 14-AGNRs as seen on the Ag(111) surface. This difference is probably due to the preferential alignment of the polyanthracene chains and subsequently the GNRs on the Cu(111) surface, as opposed to the random alignment observed on the Ag(111) surface when GNRs are formed.

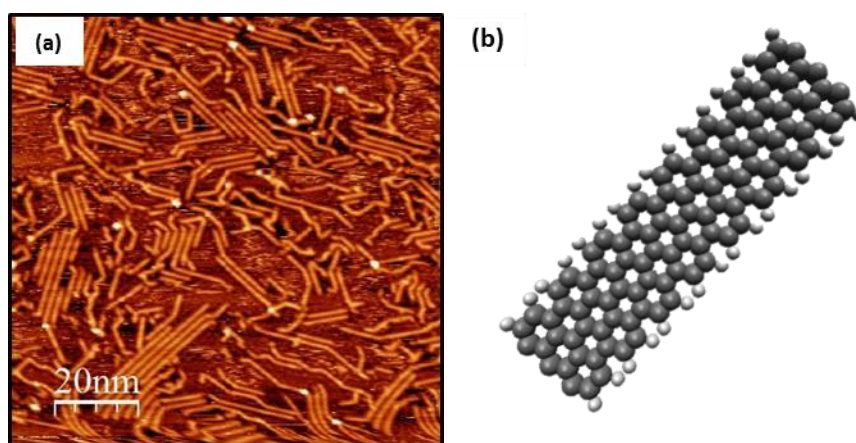


Figure 4.22: (a) STM image of the GNRs formed on the Cu(111) surface after thermal activation to 200°C, ($V_b = 1.48V$, $I_t = 0.04nA$) and (b) a graphical representation of a 7-AGNR with hydrogen terminated edges.

Measurements of the GNR heights were taken from STM images recorded at different tip-sample bias conditions are shown in Figure 4.23. The apparent height of the GNRs is 70 ± 11 pm due to the relaxation of the anthracene tilt in the previously formed chains. The

loss of hydrogen atoms during the cyclodehydrogenation reaction eliminates the steric hindrance between anthracene units in the polyanthracene chains.

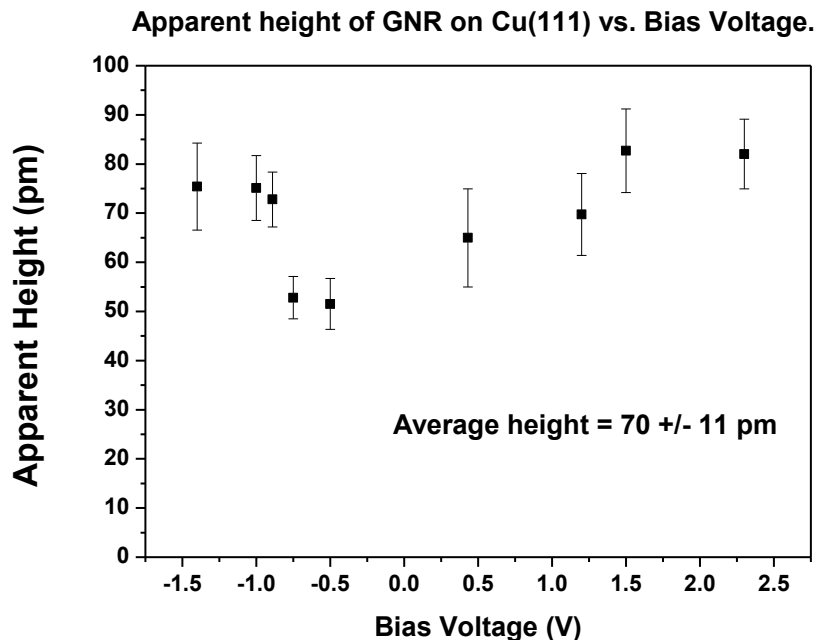


Figure 4.23: Apparent GNR height on the Cu(111) surface at varying voltages.

Most of the GNRs formed are between 10 nm and 20 nm in length and the longest chain observed was 60 ± 5 nm. Figure 4.24 shows the distribution of GNR length on the Cu(111) surface with a fit to the data using an ‘Extreme Peak Function’ in MicroCal Origin^[11].

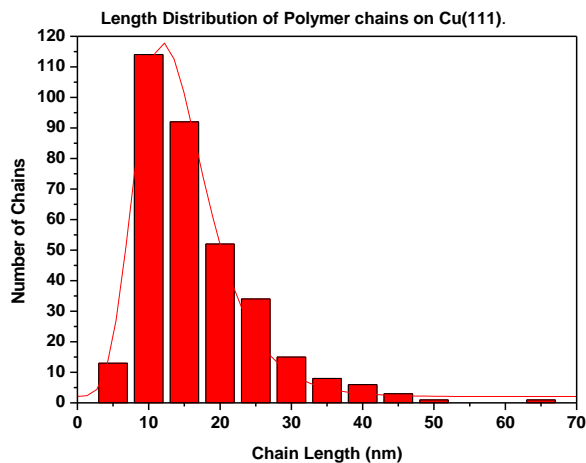


Figure 4.24: GNR distribution on the Cu(111) surface.

While the polymer chains grow along three directions, the GNRs are orientated along six directions as shown in the Fourier Transform in Figure 4.25 (b). The most likely directional preferences are highlighted in the model presented in Figure 4.26.

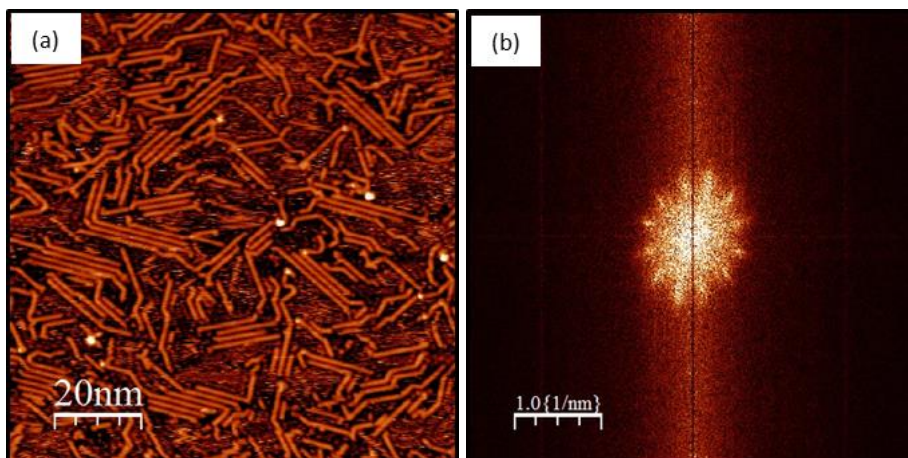


Figure 4.25: (a) Large scale image of GNRs formed from deposition of DBBA on the Cu(111) substrate at RT and subsequently annealed to 200°C, ($V_b = 1.48\text{V}$, $I_t = 0.04\text{nA}$). (b) FFT taken from Figure 4.25 (a) of GNRs on Cu(111) indicating six preferential growth directions.

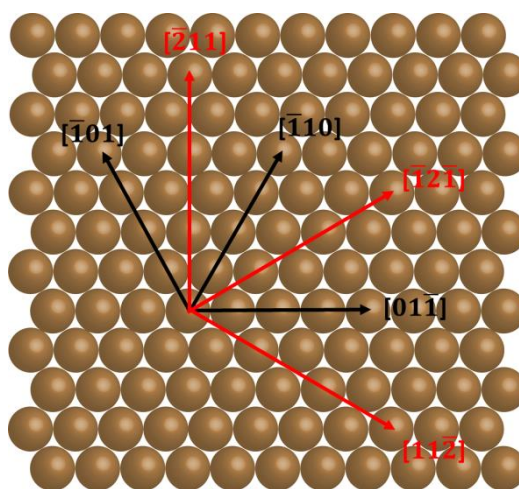


Figure 4.26: Principal and additional crystallographic directions of the Cu(111) surface and the directions of GNRs.

The growth dynamics of GNRs on Cu(111) are studied by PE spectra of bromine and carbon core levels. The Br 3d spectra shown in Figure 4.27 were recorded as a function of annealing temperature. The Br 3d line consists of a single spin-orbit split component

throughout the entire temperature range and has disappeared by 550 °C. The absence of a significant evolution of the Br 3d spectral shape upon annealing and the fact that only one spin-orbit split doublet exists suggests that this component is due to atomic Br adsorbed on Cu(111) surface. The binding energy of the Br 3d_{5/2} component is 68.5 eV; this is shifted by 0.7 eV and 0.2 eV to higher binding energy relative to the Br atoms on Au(111) and Ag(111) surfaces respectively. This is in agreement with previous studies [20].

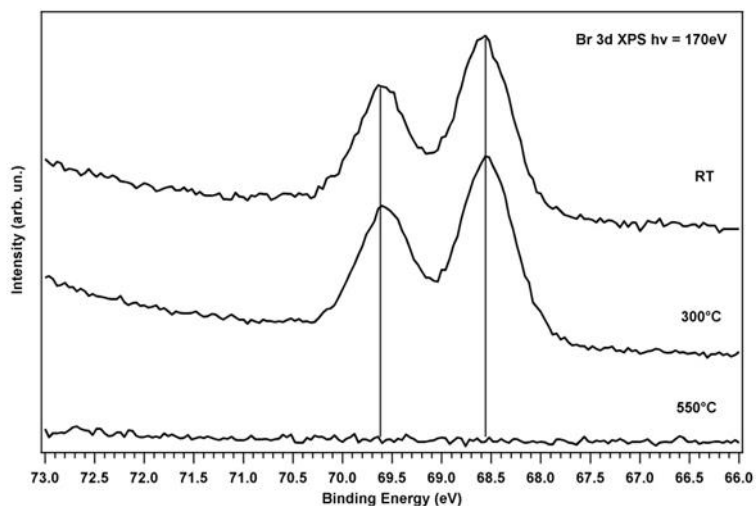


Figure 4.27: Br 3d PE spectra of DBBA/Cu(111) as a function of increasing sample temperature.

This shift in binding energies is attributed to a stronger Br-Cu interaction compared to bromine on the Au or Ag surfaces. The greater reactivity of copper at RT enables DBBA to debrominate upon adsorption hence creating free radicals which, in turn, leads to the formation of polymer chains.

Figure 4.28 shows the evolution of the C 1s synchrotron PE spectra from DBBA and its derivatives as the system is annealed from RT to 400°C and then to 750°C. At temperatures lower than or equal to 400°C the peak fitting analysis was performed similar to the case of Au. Again, three groups of atoms are considered at RT: carbons in C(C₃) and C(C₂H) sites, and unlike Au(111), the two carbon atoms which have lost their Br neighbours C(C₂) sites. Consequently, the C 1s PE line for the debrominated molecules is fitted with three components. The binding energy of the sp² component in graphene on Cu(111) has been

chosen as a reference for the energy position of the peak corresponding to carbon in the (C(C₃)) sites, C₂ (284.5 eV).

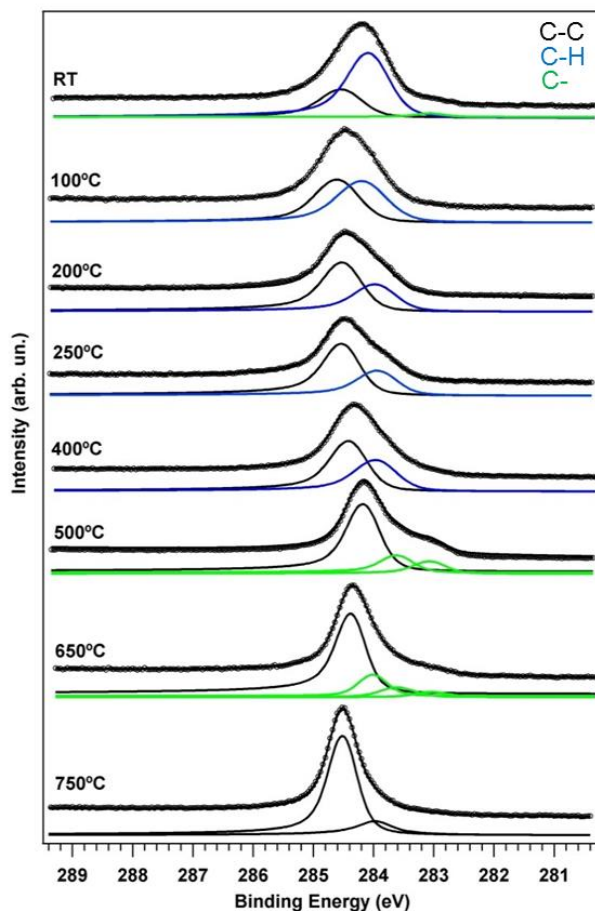


Figure 4.28: Evolution of the C 1s PE spectra of DBBA/Cu(111) as a function of increasing sample temperature.

The energy separation of 0.4 eV between C₁ and C₂ in DBBA on Au(111) has been used to set the position of the C₁ component (284.1 eV), while component C₃ (C(C₂) sites) is located at the low-energy side of the spectrum (283.0 eV). This pronounced change in the position of C₃ (in comparison with DBBA on Au) is caused by an excess of electron density on the two C atoms which have lost their Br neighbours. The dangling bonds formed on these C atoms after debromination are likely to interact with the valence states of active Cu atoms forming C–Cu bonds. The evolution of the C 1s PE spectrum upon

annealing to 100°C, when polymer chains are formed, and further to 250°C, when 7-AGNRs are formed, is similar to the case of GNR formation on Au(111). The relative intensities of the components, listed in Table 4.3, are in close agreement with the model structures suggested for each annealing step. Some deviations from the values predicted by the model are most likely due to the interaction with the Cu(111) substrate. Annealing to 500°C causes a notable change in the spectrum reflecting a decomposition of the GNRs and the formation of a disordered phase. At this temperature only dehydrogenated carbon-containing species remain on the surface. The appearance of a broad low-energy shoulder (fitted with two green components) results from the carbon atoms with reduced coordination (various edge atoms) probably interacting with the Cu(111) substrate. This strong interaction is also responsible for the low-energy shift of the dominant C₂ component. At 650°C the carbon atoms start to aggregate leading to a reduction in the amount of the edge C atoms, until eventually graphene islands, confirmed via STM, are formed at around 750°C. Percentage ratios of the evolving chemical changes, from RT to GNR formation, can be found in Table 4.3.

Cu(111)			
	<u>C-C (%)</u>	<u>C-H (%)</u>	<u>C-Br (%)</u>
Molecule**	30 (36)	67 (57)	3 (7)
Chain	48 (43)	52 (57)	0 (0)
7-AGNR	65 (71)	35 (29)	0 (0)

*Table 4.3: Percentage intensities of the C 1s components during the evolution of DBBA molecules to GNRs on the Cu(111) surface. Values in brackets indicate the expected values. **Debrominated molecules.*

Between 250°C (GNR formation) and 400°C there is no significant change in the C 1s PE spectrum which indicates a strong and stable GNR structure between these temperatures. Annealing from 400°C to 500°C causes a broadening of the line-shapes and a shift to lower binding energy of the C-C component. From this data, it can be proposed that new carbon species have formed, additional C-H bonds have been created and different C-C bonds are now present on the Cu(111) surface. This major change in the chemical environment which

the carbon atoms experience can be further understood from the STM data and graph shown in Figure 4.29, which was recorded after the surface was annealed to 420°C and shows that decomposition of the GNRs has taken place. The decomposed GNRs form small islands varying in height. Trenches are observed which lead into these islands and exhibit nanoline-like structures, albeit as depressions rather than protrusions. Analysis of these features allows calculations to be made resulting in depth and width measurements of 0.14 ± 0.01 nm and 2.00 ± 0.05 nm respectively. The small islands of copper and organic material have heights between 0.14 ± 0.02 nm and 0.25 ± 0.02 nm. It is proposed that as the GNRs decompose the underlying Cu atoms are extracted from the surface leaving the trenches. The extracted Cu atoms can diffuse on the surface at RT and coalesce to form small copper islands. These islands are surrounded by decomposed fragments of the DBBA molecules.

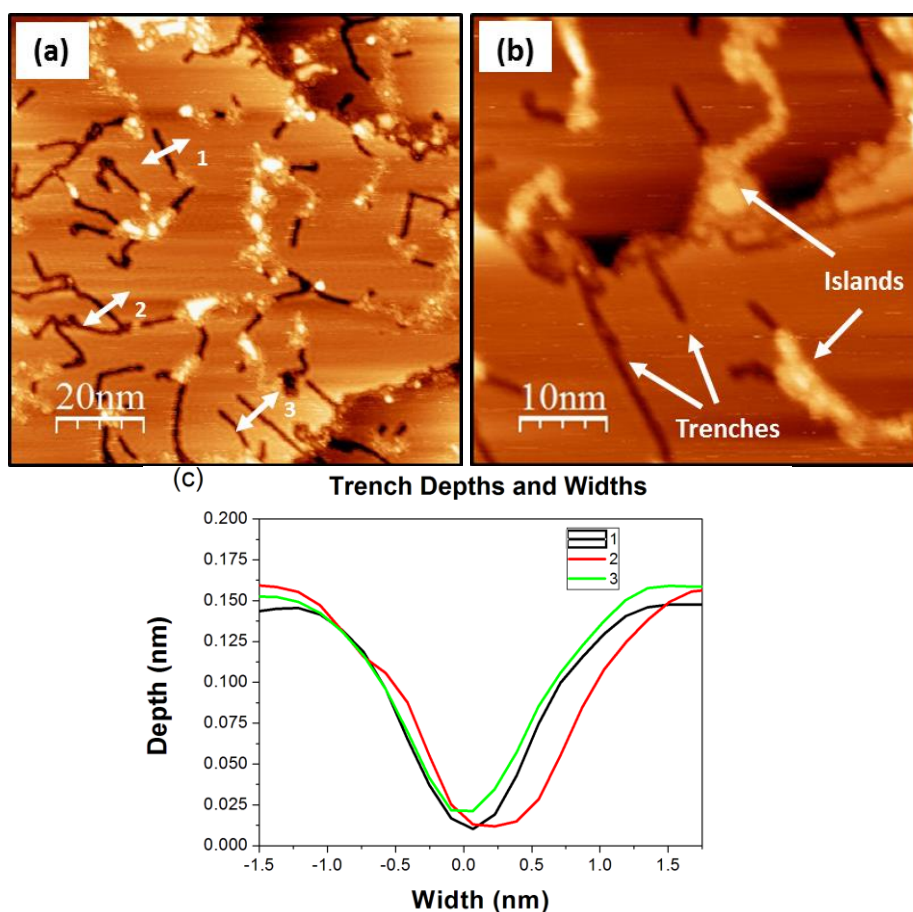


Figure 4.29: STM images of GNRs after annealing to 420°C. (a) Islands of decomposed organic material and trenches are present ($V_b = -1.61V$, $I_t = 0.04nA$), (b) a magnified images highlighting these features, ($V_b = -1.42V$, $I_t = 0.04nA$) and (c) apparent depth and width of decomposed GNR trenches from Figure 4.29 (a).

Annealing to 650°C sees the high intensity peak revert back to its initial binding energy of 284.5eV ($C(C_3)$) while the low binding energy components shift slightly to higher energies and decrease in intensity. This would indicate that C-C bonds are reforming into a chemical environment as observed during the GNR stage ($C(C_3)$), i.e. benzene type structures. A final anneal at 750°C produces a PES signal indicative of graphene^[25]. After this final anneal there exists two spectral components: the dominant component at 284.5eV, due to carbon atoms in the sp^2 configuration ($C(C_3)$), and the other at 284.0eV which can be assigned to carbon atoms at the edges of the graphene islands or defects through the lattice^[26].

Figure 4.30 shows a series of STM images after annealing DBBA on Cu(111) to 700°C, where islands of material are observed which cover the entire surface, Figure 4.30 (a). These islands are larger than those observed at the GNR decomposition stage 400°C anneal and exhibit lateral dimension ranging from approximately 3×3 nm to 20×20 nm and have apparent heights of 0.40 ± 0.05 nm above the underlying Cu substrate. Magnification of these images shown in Figures 4.30 (c) and (d) shows hexagonal features which are indicative of graphene while Figure 4.30 (b) shows a moiré pattern on the islands. The moiré pattern is observed in three directions which lay 120° relative to each other and have a periodicity of 0.49 ± 0.05 nm which implies that the direction of the pattern is dictated by the copper substrate.

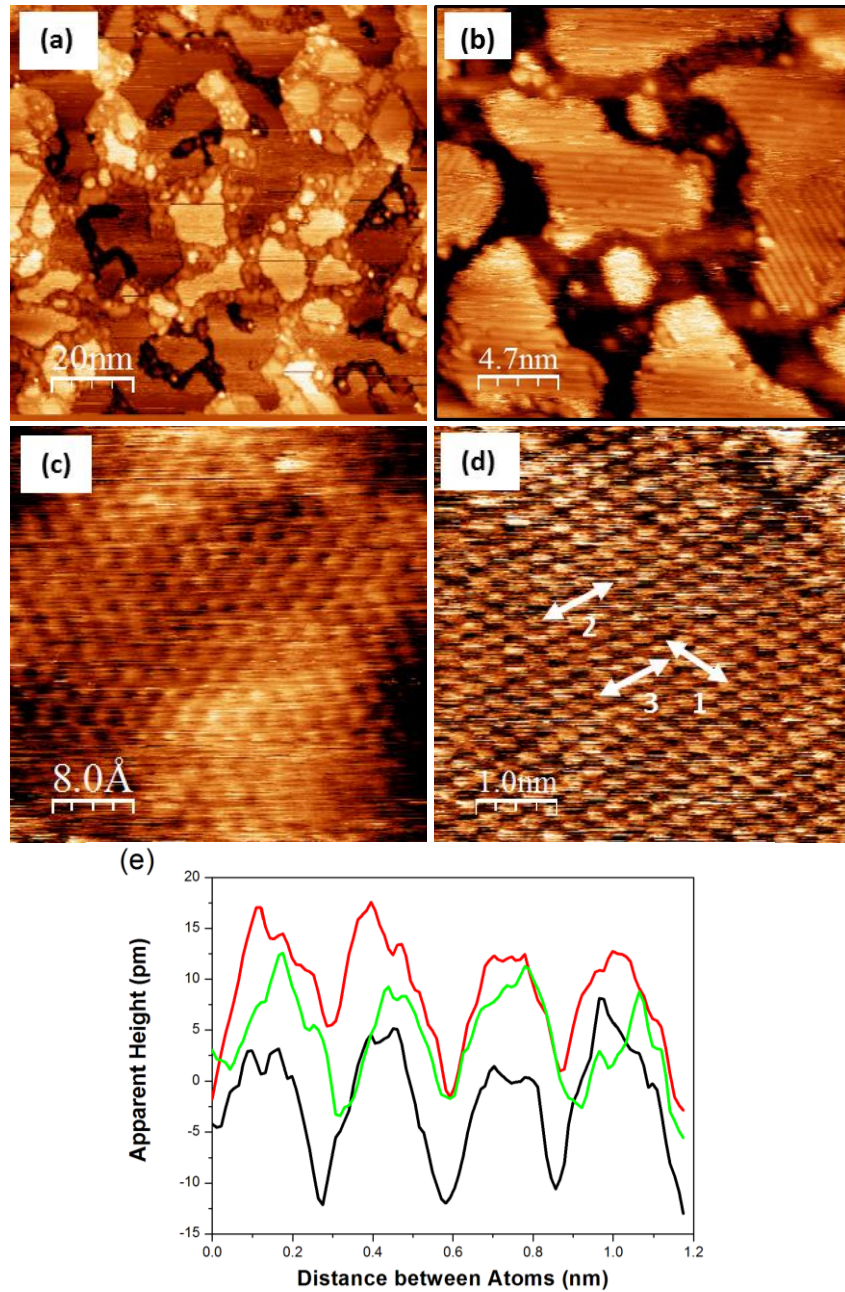


Figure 4.30: Graphene islands on Cu(111). Successive magnifications. (a) ($V_b = -0.20V$, $I_t = 2.74nA$), (b) ($V_b = 0.28V$, $I_t = 1.27nA$), (c) ($V_b = 1.4V$, $I_t = 0.04nA$), (d) ($V_b = 0.01V$, $I_t = 2.28nA$) and (e) line profiles 1 (black), 2 (red) and 3 (green) from Figure 4.30 (d).

These STM images show that graphene forms after annealing to 700°C on the Cu(111) surface where evidence of a moiré pattern is visible (see Figure 4.30 (b)) due to an incommensurability of lattice constants between the graphene and underlying substrate (0.256 nm). The lattice constant of graphene is 0.246 nm which agrees with the value of

0.27 ± 0.03 nm measured from multiple line scans and averaging of the features observed in Figure 4.30 (d). Typical line profiles are shown in Figure 4.30 (e).

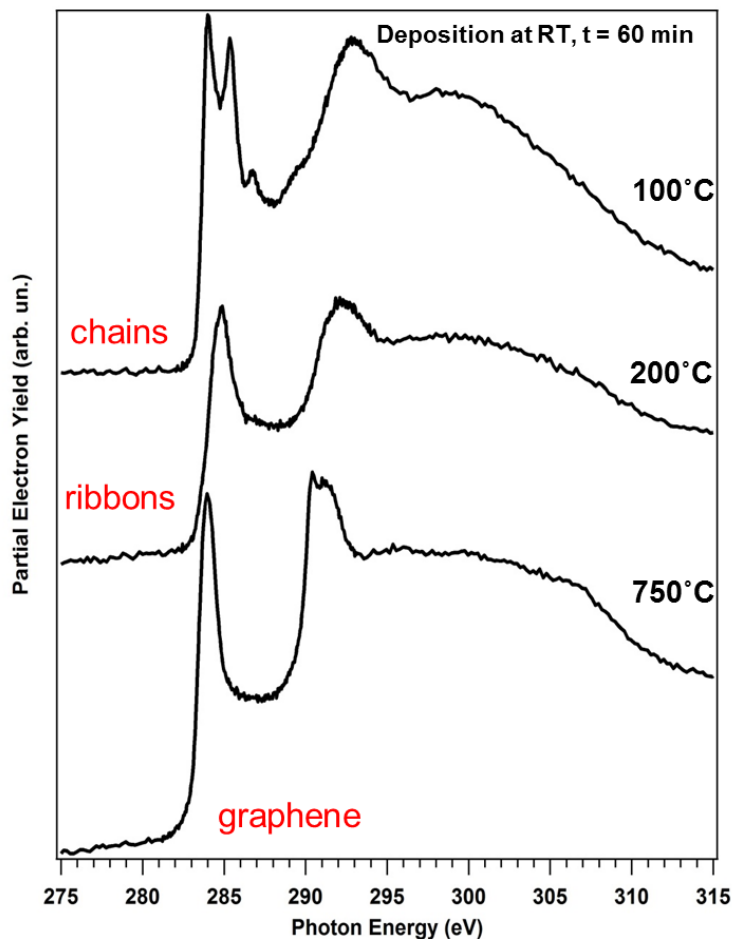


Figure 4.31: C K-edge NEXAFS spectra of DBBA on Cu(111) at 50° incidence angle taken after annealing to 100°C , 200°C and then 750°C .

A series of C K-edge XAS spectra for DBBA on Cu(111) are shown in Figure 4.31. The behaviour of the spectrum taken at an angle of 50° is similar to that observed on the Au(111) and Ag(111) surfaces. It should be noted that here, the spectrum after a 100°C anneal is identical to the RT spectrum (not shown). At this stage the spectrum differs from that of the Au(111) surface as the A_2 peak has already begun to merge with the A_1 peak (the Au spectra in Figure 4.13 has three resolvable peaks). The spectrum here resembles that of polymer chains of DBBA. This is due to the more reactive Cu(111) surface allowing the

initial reaction (debromination) to occur more readily, in agreement with the Br 3d PE spectra (debromination begins at RT and completes by 100°C). Thus, the XA spectra and DBBA molecules on Cu(111) at 100°C is similar to the polymer chains on Au(111) and Ag(111) at 200°C and 150°C respectively. There are other observed similarities between the spectra of Cu(111) at 250°C and Au(111) at 400°C (and also Ag(111) between 300°C and 400°C) where peaks A_1 , A_2 and A_3 have converged into a single broad feature. This feature would suggest that the absorbed material is now lying in-plane with the substrate and implies that ribbons have formed in all cases. At the GNR formation stage (200°C) on the Cu(111) surface, cyclodehydrogenation has taken place within the polymer chains enabling the ribbons to lie in-plane with the substrate. Annealing the Cu(111) surface further, to 750°C, the broad π^* signal present after annealing to 200°C sharpens significantly and observable features in the σ^* region become apparent. This spectral structure is characteristic of graphene weakly bound to the substrate and is similar to that of bulk graphite^[16].

4.5 Summary

In this chapter, DBBA was used to successfully grow GNRs on the Au(111), Ag(111) and Cu(111) surfaces. After deposition at RT, Br 3d PES measurements indicate that no debromination, ~50% debromination and ~95% debromination occurs on the Au, Ag and Cu surfaces respectively. This debromination allows polymer chains to grow at 200°C, 150° and RT on Au, Ag and Cu respectively. Furthermore, due to steric hindrance between neighbouring anthracene units, there is a tilt in the DBBA molecule which is verified by XAS measurements. The chains are observed to grow in random directions on the Au(111) and Ag(111) surfaces whereas a definite directional preference is evident on the Cu(111) surface. These preferred growth directions were confirmed by FFT analysis of the STM images, showing three chain orientations in the [-101], [-110] and [01-1] directions of the Cu(111) surface. Further analysis of the chains on the Cu(111) surface reveals evidence that an organo-metallic bonding has occurred between the DBBA units.

Cyclodehydrogenation and subsequent GNR formation are observed at 400°C, 370° and 200°C on Au, Ag and Cu respectively. This is confirmed through C 1s PES spectra which indicate a transfer of intensity from C-H bonds to C-C bonds, indicative of

dehydrogenation and new C-C bonds forming. XAS measurements show that GNRs on all three surfaces are planar and lying parallel to the surface. The apparent heights of the GNRs on the surfaces are shown in Figure 4.38 providing an indirect insight into the GNR/substrate interaction. GNRs on gold are furthest from the surface at 170 ± 14 pm while GNRs on copper are closest at 70 ± 11 pm. These heights were independent of the bias voltage used. Interesting features are observed on the Ag surface; 14-AGNRs and either a 2×1 surface reconstruction or a confined charge density effect. The 14-AGNRs occurs due to cross dehydrogenation between two 7-AGNRs which explains the additional transfer of intensity from the C-H peaks to the C-C peak intensity. The most ordered GNRs are observed on the Cu(111) surface. The GNRs align in six preferred directions as indicated by FFT analysis and observed via STM images.

On the Cu(111) surface, GNRs decompose after annealing to 420°C resulting in small structural islands and nanoline like trenches. Annealing further to 700°C , results in the formation of graphene domains with dimensions of up to 20×20 nm. Moiré patterns decorate these domains with a common periodicity of 0.49 ± 0.05 nm and angular separation of 120° to each other. Upon magnification of the domains, the graphene structure is observed. Figure 4.32 shows the average apparent height of the GNRs on the three chosen substrates which indicates that the copper surface is most reactive, followed by silver, then gold. Finally, a table showing how DBBA appears on each surface, at various anneal temperatures, is shown in Table 4.4.

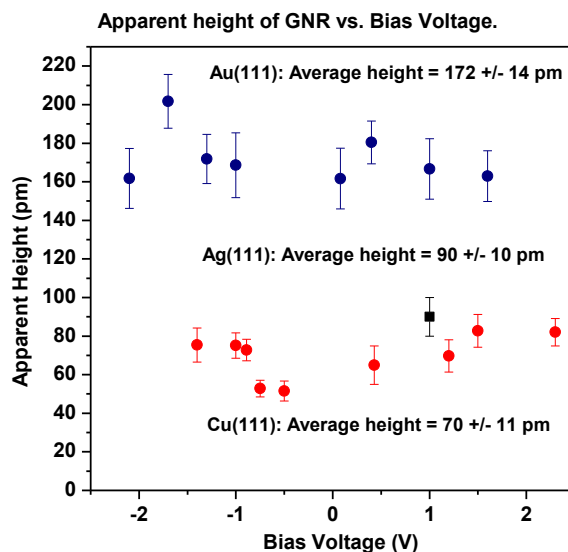


Figure 4.32: Graph showing the apparent heights of GNRs on the (111) surfaces at different bias conditions. The error bars differ due to the number of GNRs sampled per bias voltage. Only one data point is present for Ag(111).

Temp (°C)	<u>Au</u>	<u>Ag</u>	<u>Cu</u>
23°C (RT)	Molecule	Molecule	Molecule/Chain
50°C	Molecule	Molecule	Chain
100°C	Molecule	Molecule/Chain	Chain
150°C	Molecule/Chain	Chain	Chain
200°C	Chain	Chain	Chain/GNR
250°C	Chain	Chain	GNR
300°C	Chain	Chain/GNR*	GNR
350°C	Chain/GNR	GNR*	GNR
400°C	GNR	GNR*	GNR
700°C - 750°C	N/A	N/A	Graphene

Table 4.4: DBBA representation on the different surfaces at different temperatures. *7 and 14-AGNRs.

4.6 References

- [1] Geim, A.K. 2009, "Graphene: Status and Prospects", *Science*, vol. 324, no. 5934, pp. 1530-1534.
- [2] Cai, J., Ruffieux, P., Jaafar, R., Bieri, M., Braun, T., Blankenburg, S., Muoth, M., Seitsonen, A.P., Saleh, M., Feng, X., Muellen, K. & Fasel, R. 2010, "Atomically precise bottom-up fabrication of graphene nanoribbons", *Nature*, vol. 466, no. 7305, pp. 470-473.
- [3] Ruffieux, P., Cai, J., Plumb, N.C., Patthey, L., Prezzi, D., Ferretti, A., Molinari, E., Feng, X., Muellen, K., Pignedoli, C.A. & Fasel, R. 2012, "Electronic Structure of Atomically Precise Graphene Nanoribbons", *Acs Nano*, vol. 6, no. 8, pp. 6930-6935.
- [4] Blankenburg, S., Cai, J., Fasel, R., Feng, X., Muellen, K., Passerone, D., Pignedoli, C., Ruffieux, P., Mullen, K. & Pignedoli, C.A. *Segmented graphene nanoribbon useful for generating heterojunctions and heterostructures, comprises at least two different graphene segments covalently linked to each other.*
- [5] Bangert, U., Gass, M., Bleloch, A.L. & Nair, R.R. 2010, "Atomic scale graphene landscapes - natural, dosed and doped", *Electron Microscopy and Analysis Group Conference 2009 (Emag 2009)*, vol. 241, pp. 012098.
- [6] Bangert, U., Pan, C.T., Nair, R.R. & Gass, M.H. 2010, "Structure of hydrogen-dosed graphene deduced from low electron energy loss characteristics and density functional calculations", *Applied Physics Letters*, vol. 97, no. 25, pp. 253118.
- [7] Ohta, T., Bostwick, A., Seyller, T., Horn, K. & Rotenberg, E. 2006, "Controlling the electronic structure of bilayer graphene", *Science*, vol. 313, no. 5789, pp. 951-954.
- [8] Kosynkin, D.V., Higginbotham, A.L., Sinitskii, A., Lomeda, J.R., Dimiev, A., Price, B.K. & Tour, J.M. 2009, "Longitudinal unzipping of carbon nanotubes to form graphene nanoribbons", *Nature*, vol. 458, no. 7240, pp. 872-U5.
- [9] Simonov, K.A., Vinogradov, N.A., Vinogradov, A.S., Generalov, A.V., Zagrebina, E.M., Martensson, N., Cafolla, A.A., Carpy, T., Cunniffe, J.P. & Preobrajenski, A.B. 2014, "Effect of Substrate Chemistry on the Bottom-Up Fabrication of Graphene Nanoribbons: Combined Core-Level Spectroscopy and STM Study", *Journal of Physical Chemistry C*, vol. 118, no. 23, pp. 12532-12540.
- [10] Klues, M., Hermann, K. & Witte, G. 2014, "Analysis of the near-edge X-ray-absorption fine-structure of anthracene: A combined theoretical and experimental study", *Journal of Chemical Physics*, vol. 140, no. 1, pp. UNSP 014302.
- [11] *Origin (OriginLab, Northampton, MA)*

- [12]Liu, A.C. & Friend, C.M. 1988, "The Structure and Reactivity of Chemisorbed Aromatics - Spectroscopic Studies of Benzene on Mo(110)", *Journal of Chemical Physics*, vol. 89, no. 7, pp. 4396-4405.
- [13]Yang, M.X., Xi, M., Yuan, H.J., Bent, B.E., Stevens, P. & White, J.M. 1995, "Nexafs Studies of Halobenzenes and Phenyl Groups on Cu(111)", *Surface Science*, vol. 341, no. 1-2, pp. 9-18.
- [14]Alagia, M., Baldacchini, C., Betti, M.G., Bussolotti, F., Carravetta, V., Ekstrom, U., Mariani, C. & Stranges, S. 2005, "Core-shell photoabsorption and photoelectron spectra of gas-phase pentacene: Experiment and theory", *Journal of Chemical Physics*, vol. 122, no. 12, pp. 124305.
- [15]Rocco, M.L.M., Frank, K.H., Yannoulis, P. & Koch, E.E. 1990, "Unoccupied Electronic-Structure of Phthalocyanine Films", *Journal of Chemical Physics*, vol. 93, no. 9, pp. 6859-6864.
- [16]Stöhr, J. 1992, *NEXAFS spectroscopy*, Springer.
- [17]Doyle, C. 2013, *An investigation of the structural and electronic properties of covalently bonded molecular networks on metal surfaces formed through debromination reactions*.
- [18]Lee, H.L. 2012, *Strategies for the formation of covalently bonded nano-networks on metal surfaces through amine reactions*.
- [19]Owens, F.J. 2014, "Pentacene and poly-pentacene as graphene nanoribbons", *Solid State Communications*, vol. 185, pp. 58-61.
- [20]Di Giovannantonio, M., El Garah, M., Lipton-Duffin, J., Meunier, V., Cardenas, L., Revurat, Y.F., Cossaro, A., Verdini, A., Perepichka, D.F., Rosei, F. & Contini, G. 2013, "Insight into Organometallic Intermediate and Its Evolution to Covalent Bonding in Surface-Confined Ullmann Polymerization", *Acs Nano*, vol. 7, no. 9, pp. 8190-8198.
- [21]Fan, Q., Wang, C., Han, Y., Zhu, J., Kuttner, J., Hilt, G. & Gottfried, J.M. 2014, "Surface-Assisted Formation, Assembly, and Dynamics of Planar Organometallic Macrocycles and Zigzag Shaped Polymer Chains with C-Cu-C Bonds", *Acs Nano*, vol. 8, no. 1, pp. 709-718.
- [22]Gutzler, R., Cardenas, L., Lipton-Duffin, J., El Garah, M., Dinca, L.E., Szakacs, C.E., Fu, C., Gallagher, M., Vondracek, M., Rybachuk, M., Perepichka, D.F. & Rosei, F. 2014, "Ullmann-type coupling of brominated tetrathienoanthracene on copper and silver", *Nanoscale*, vol. 6, no. 5, pp. 2660-2668.

- [23] Hanke, F., Haq, S., Raval, R. & Persson, M. 2011, "Heat-to-Connect: Surface Commensurability Directs Organometallic One-Dimensional Self-Assembly", *Acs Nano*, vol. 5, no. 11, pp. 9093-9103.
- [24] Haq, S., Hanke, F., Dyer, M.S., Persson, M., Iavicoli, P., Amabilino, D.B. & Raval, R. 2011, "Clean Coupling of Unfunctionalized Porphyrins at Surfaces To Give Highly Oriented Organometallic Oligomers", *Journal of the American Chemical Society*, vol. 133, no. 31, pp. 12031-12039.
- [25] Zhang, W., Nefedov, A., Naboka, M., Cao, L. & Woell, C. 2012, "Molecular orientation of terephthalic acid assembly on epitaxial graphene: NEXAFS and XPS study", *Physical Chemistry Chemical Physics*, vol. 14, no. 29, pp. 10125-10131.
- [26] Lacovig, P., Pozzo, M., Alfe, D., Vilmercati, P., Baraldi, A. & Lizzit, S. 2009, "Growth of Dome-Shaped Carbon Nanoislands on Ir(111): The Intermediate between Carbide Clusters and Quasi-Free-Standing Graphene (vol 103, 166101, 2009)", *Physical Review Letters*, vol. 103, no. 17, pp. 179904.

Chapter 5

STM study of DBBA on the Cu(110) Surface

5.1 Introduction

Following on from the study of DBBA molecules on Au(111), Ag(111) and Cu(111), this chapter investigates the deposition of DBBA on the Cu(110) surface at room temperature and subsequent annealing stages which ultimately result in the formation of large graphene domains.

5.2 Submonolayer Coverage of DBBA on the Cu(110) Surface

After deposition of $\sim 0.65\text{ML}$ of DBBA on the Cu(110) surface at room temperature, chains similar to those formed on the Cu(111) surface are formed as shown in Figure 5.1. The polyanthracene chains show similar physical characteristics to those observed on Cu(111) with bright alternating protrusions along the chains showing that the anthracene units remain tilted relative to each other.

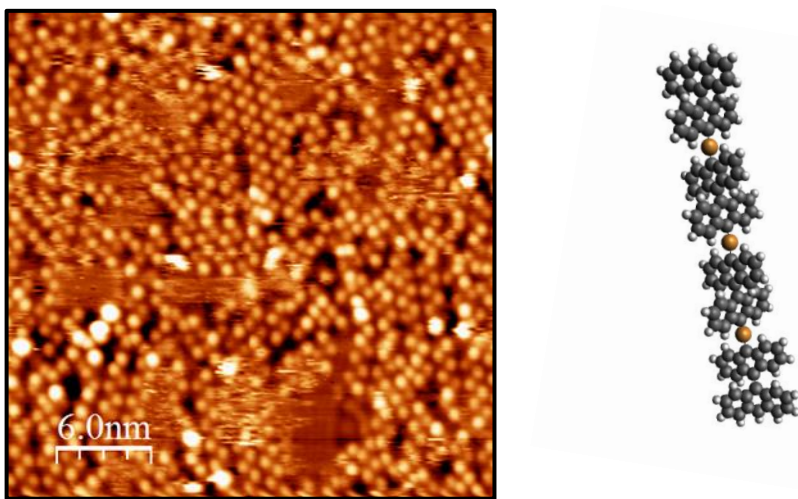


Figure 5.1: STM image showing RT deposited DBBA on the Cu(110) surface and corresponding schematic of the molecular arrangement, ($V_b = 1.2\text{V}$, $I_t = 0.07\text{nA}$).

This up/down tilt along the chain can again be attributed to the steric hindrance caused by hydrogen repulsion between neighbouring anthracene subunits ^[1]. The lateral width of the chains is 1.33 ± 0.05 nm while the distance between the bright protrusions is 1.21 ± 0.05 nm which by comparison with results for DBBA on the Cu(111) surfaces, implies that an organo-metallic bonds are formed (C-Cu-C bond) where the molecules are separated by an intervening copper atom ^[2]. The longest uninterrupted chains observed are approximately 10 nm. Debromination has occurred enabling DBBA molecules to form by radical addition of an intermolecular copper atom. Annealing the Cu(110) surface to 215°C results in an ordering of the debrominated DBBA molecules along the [001] crystallographic direction as shown in Figure 5.2 (a). Figure 5.2 (b) shows a magnified image of the molecules with the unit cell superimposed. The oblique unit cell has dimensions 1.57×1.41 nm and angle between lattice vectors of $62^\circ \pm 4^\circ$ and contains 3 atoms, most probably 2 bromine atoms and 1 copper atom as shown. The bromine atoms are coloured red and the copper atom (2 half atoms in the unit cell) coloured gold.

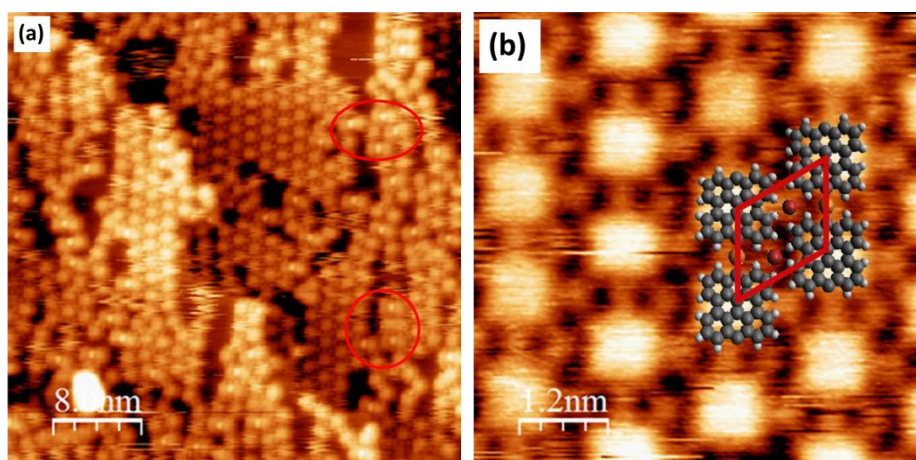


Figure 5.2: STM images of (a) large scale arrangement of DBBA molecules showing evidence of dimers (red circles), ($V_b = 1.33V$, $I_t = 0.03nA$) and (b) magnified region highlighting DBBA molecules, the unit cell and bromine/copper atoms, ($V_b = 1.33V$, $I_t = 0.33nA$).

The copper adatoms engaging in the C-Cu-C organo metallic bonding and the proposed bromine atoms appear $20\text{pm} \pm 1 \text{ pm}$ above the underlying substrate.

After annealing to 215°C the DBBA molecules have a square appearance with lateral dimensions of 0.97 ± 0.03 nm and height of 35 ± 3 pm; this implies that intra-molecular

cyclodehydrogenation has taken place. The four inner hydrogens have dissociated and two new carbon-carbon bonds have formed and the molecules are no longer tilted. The majority of molecules are aligned along the [001] direction of the Cu(110) substrate. An intermediate organometallic complex has formed which explains the bright central atom between DBBA molecules. The centre to centre distance between DBBA units in this arrangement is measured as 1.28 ± 0.05 nm which closely agrees with those found in Figure 5.1 and theoretical distance of 1.11 nm if an organo-metallic complex is formed [3, 4, 5, 6, 7, 8]. In some areas, dimers are observed (see red circled areas in Figure 5.2 (a)), which appear with bright atoms between molecules in adjacent rows. They exhibit widths of 2.14 ± 0.1 nm. It is possible that cyclodehydrogenation has taken place as the measured distance is in close agreement to the predicted distance of 1.87 nm. This covalent bonding between two DBBA molecules occurs at 90° to the direction of the organo-metallic DBBA chains. Another possible explanation is shown in Figure 5.3 where two molecules form 3 C-Cu-C bonds perpendicular to the direction of the molecular chains.

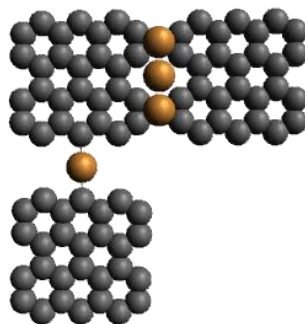


Figure 5.3: Schematic representation of an organo-metallic link (C-Cu-C bond) between DBBA molecules in a chain and also, how a dimer could form between rows.

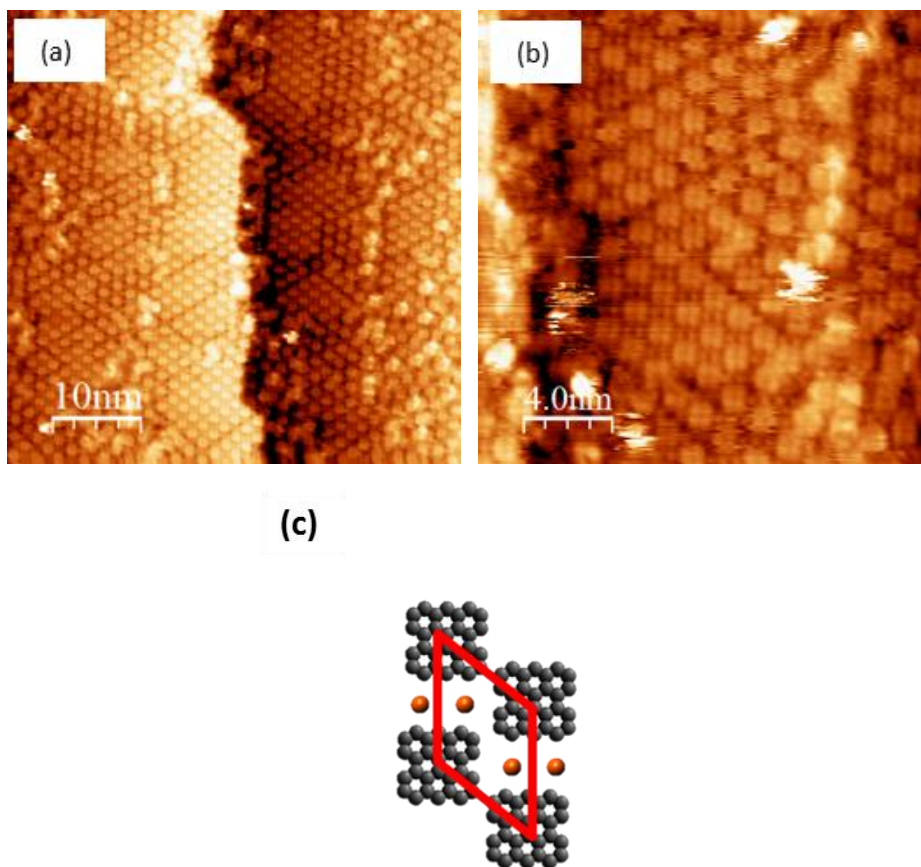


Figure 5.4: STM images showing the different packing of DBBA molecules and most common unit cell is shown in the schematic. (a) and (b) ($V_b = 0.53\text{V}$, $I_t = 0.06\text{nA}$). Unit cell model shown in (c).

Annealing to 235°C results in a change in the orientation of the DBBA molecules in a chain. The oblique packing described above is still observed but there are two packing densities. The less densely packed unit cell has dimensions $1.60 \times 1.67\text{ nm}$ while the more densely packed structure has a unit cell with dimensions $1.47 \times 1.61\text{ nm}$. In this more densely packed DBBA region, two atoms (as opposed to the single Cu atom as a result of annealing to 215°C) are visible between neighbouring units in a chain. Furthermore, as presented in Figure 5.4 (c), the unit cell now exhibits two surface atoms instead of the three observed previously in Figure 5.2 (b). It is not possible to determine accurately whether

these atoms are bromine or copper and without supplementary experimental data, e.g. XPS, this cannot be confirmed.

Figure 5.5 shows STM images recorded after deposition of DBBA molecules onto the Cu(110) substrate held at 115°C.

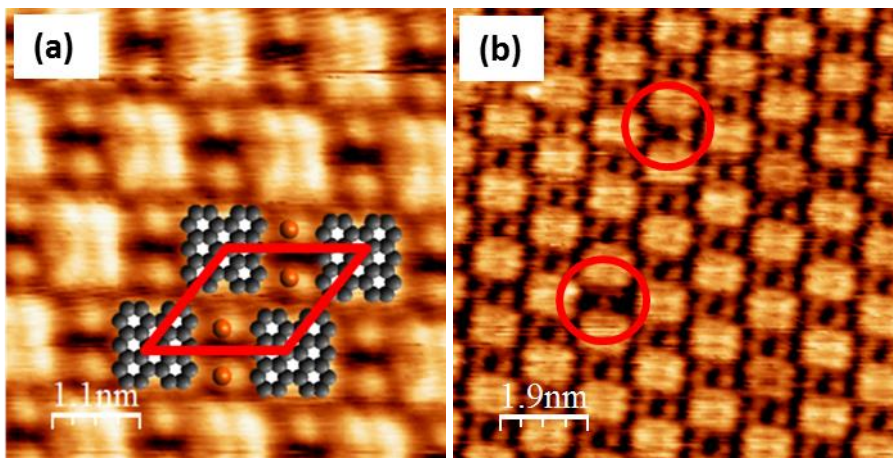


Figure 5.5: High resolution images of DBBA on Cu(110) held at 115°C. (a) Schematic superimposed onto the STM image showing copper atoms inhibit the direct interaction between adjacent DBBA molecules, ($V_b = 0.37V$, $I_t = 0.31nA$) and (b) missing copper atoms circled in red, ($V_b = -0.04V$, $I_t = 0.63nA$).

The DBBA molecules are self-assembled with greater long range ordering as compared to the deposition onto the RT surface with subsequent annealing. The unit cell shown in Figure 5.5 (a), $1.65 \times 1.37 \pm 0.05$ nm, is comprised of one DBBA molecule and two bright atoms. A schematic is superimposed on the image to show the unit cell and the proposed atoms in orange. The DBBA molecules appear rectangular and flat with dimensions 1.08×0.85 nm ± 0.09 nm suggesting cyclodehydrogenation has occurred. The closest distance between bright circular atoms is 0.57 ± 0.05 nm and each atom has a diameter of 0.24 ± 0.02 nm. Considering the van der Waals diameter of bromine (0.39 nm) and copper (0.24 nm) and also the separation of copper rows on the (110) surface, these bright inter molecular atoms can be assigned to copper adatoms, possibly from the [-110] crystallographic surface direction or mobile step atoms^[9]. Figure 5.5 (b) also shows missing copper adatoms (circled in red). The copper adatoms observed align in the [-110] direction of the Cu(110) crystal and the alignment of the DBBA molecules follows the [001] direction as described previously and shown in Figure 5.6. It is unlikely that the

organo-metallic C-Cu-C bonds have formed here due to the increased separation between molecules of $1.65 \pm 0.05 \text{ nm}^{[10]}$. The molecular and atomic arrangement is more likely to conform to the schematic diagram presented in Figure 5.6 where the copper adatoms are shown in yellow and not bonded to the DBBA molecules.

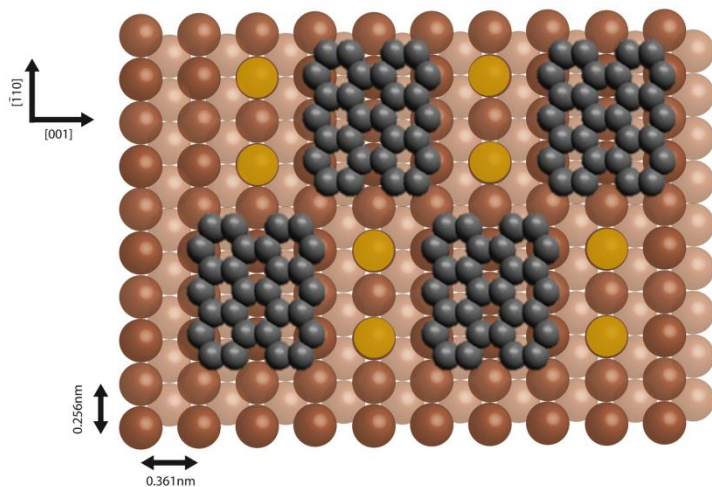


Figure 5.6: Schematic showing the proposed orientation of DBBA molecules on the Cu(110) surface.

Annealing to 250°C results in no significant change in the surface as shown in Figure 5.7 (a) with the same unit cell described above. The DBBA molecules however, appear squarer with dimensions $0.86 \times 0.93 \text{ nm} \pm 0.05 \text{ nm}$, suggesting that intra molecular dehydrogenation has occurred. Figure 5.7 (b) shows an area of the Cu(110) surface where the copper rows are visible under the DBBA molecules. The Cu(110) rows are clear and evidence of a DDBA molecule is highlighted with a white arrow confirming the direction of molecular alignment.

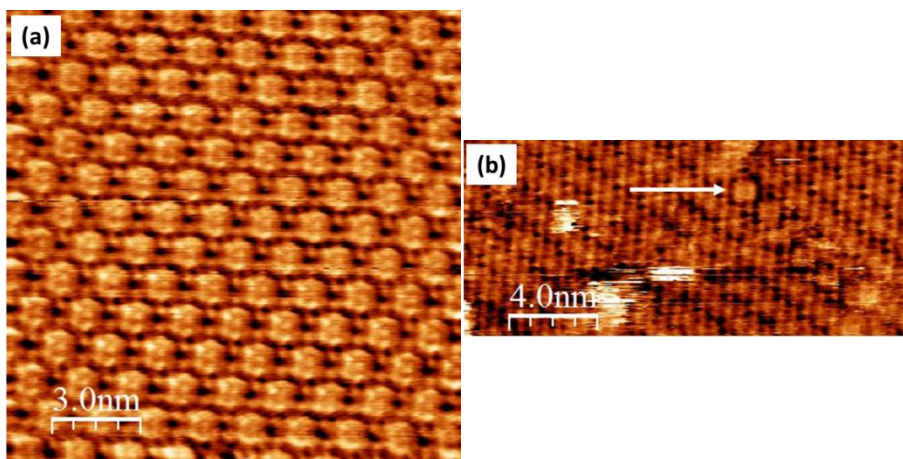


Figure 5.7: STM images of (a) densely packed region of DBBA molecules exhibiting similar structures seen after depositing onto Cu(110) held at 115 °C, ($V_b = -0.4\text{V}$, $I_t = 1.55\text{nA}$) and (b) shows a solitary DBBA molecules highlighted by the white arrow clearly indicating the rows of the underlying substrate, ($V_b = 0.72\text{V}$, $I_t = 0.58\text{nA}$).

The packing of the molecules remains unchanged upon annealing to 300 °C and there is no evidence for covalent bonding between the molecules

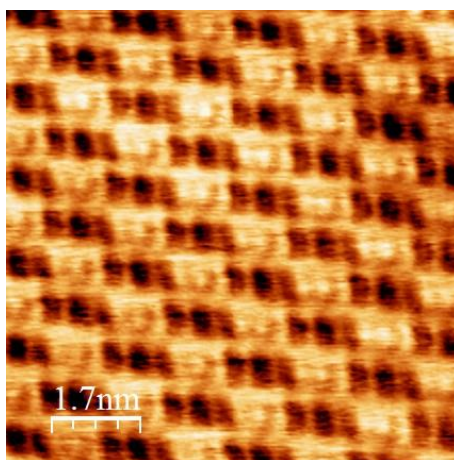


Figure 5.8: STM image after annealing the surface to 300 °C, ($V_b = 0.58\text{V}$, $I_t = 1.14\text{nA}$).

5.3 Decomposition of DBBA molecules on the Cu(110) Surface

When this surface is further annealed to 400°C, decomposition of the DBBA molecules is observed as shown in Figure 5.9.

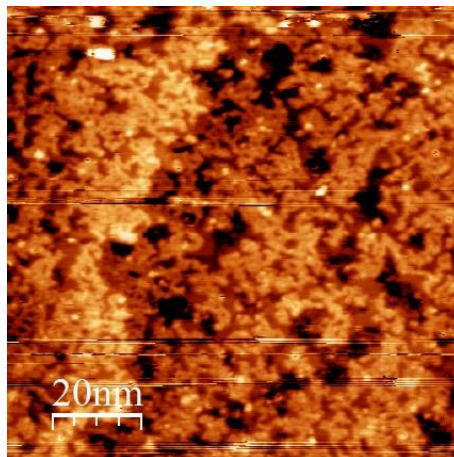


Figure 5.9: Large scale STM image showing decomposed DBBA molecules, ($V_b = 0.1V$, $I_t = 0.1nA$).

At the decomposition stage, it is expected that any remaining bromine desorbs from the surface leaving behind predominantly disordered fragments of organic material. Annealing to 550°C it results in further disruption of the surface and the formation of islands.

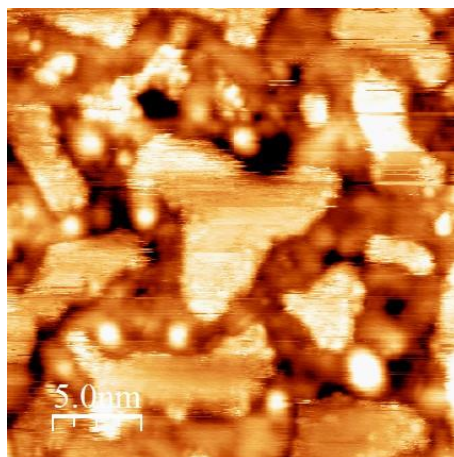


Figure 5.10: Domains of previously decomposed material are observed in this STM image which occurs after a surface anneal to 550°C, ($V_b = 0.79V$, $I_t = 0.06nA$).

After annealing at 650°C the islands are more clearly defined in Figure 5.11 (a) with structures on top which are visible upon magnification as shown in Figure 5.11 (b) and (c). The islands vary in size up to 10 x 10 nm and exhibit atomic like structure. The bright periodic atoms appear as protrusions and are separated with unit cell dimensions $0.43 \times 0.29 \text{ nm} \pm 0.02 \text{ nm}$. This is no evidence for a Cu(110) reconstruction or graphene formation. Therefore, at this stage, it is possible that carbide has formed. Further investigation is required to confirm this hypothesis.

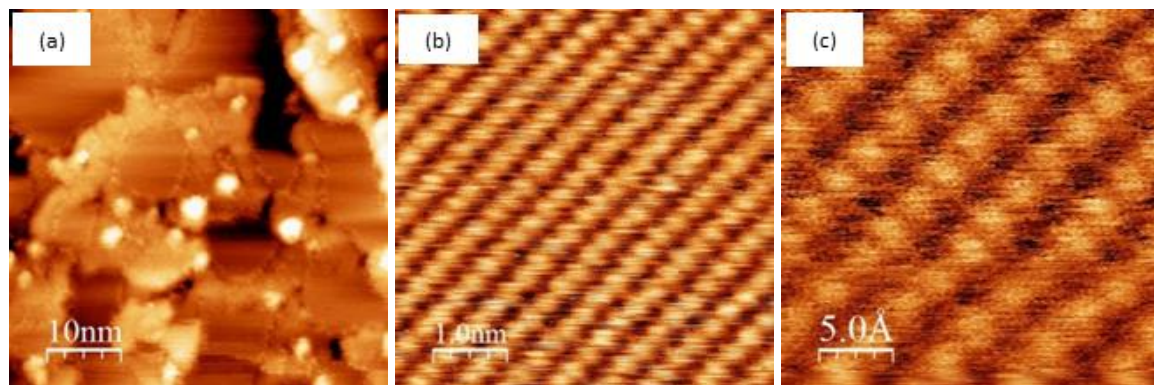


Figure 5.11: STM image of (a) island formation, ($V_b = -1.0\text{V}$, $I_t = 0.1\text{nA}$), (b) and (c) successive magnification of an island, ($V_b = 0.25\text{V}$, $I_t = 1.52\text{nA}$).

5.4 Graphene Formation from DBBA Precursors on the Cu(110) Surface.

Annealing to in excess of 700°C , results in the formation of graphene domains. Figure 5.12 shows evidence of this after annealing to 750°C . The Cu(110) surface became decorated with distinct graphene domains ($\sim 0.5\text{ML}$) which are spread randomly across the entire surface. In some cases the graphene has grown over step edges as shown by the red oval in Figure 5.12 (a). Differing orientations of the graphene, aligned by the substrate are observed, and emphasised at domain boundaries. Due to the low carbon solubility in copper, carbon nucleates in the formation of these graphene domains which can chemically ‘stitch’ together to form larger sheets (red oval in Figure 5.12 (b))^[11, 12].

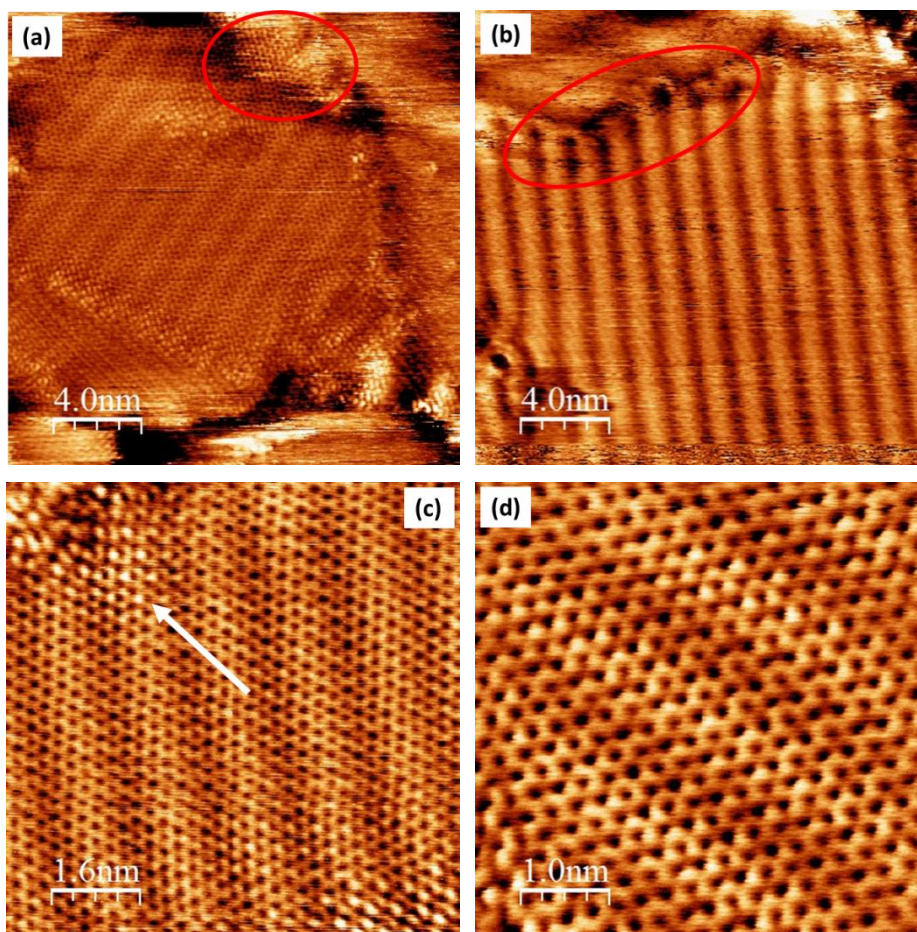


Figure 5.12: STM images showing (a) graphene boundaries and ‘climbing’ a step edge (red oval), ($V_b = 0.002\text{V}$, $I_t = 3.0\text{nA}$), (b) graphene boundary exhibiting the ‘stitching’ effect between adjacent domains, ($V_b = 1.42\text{V}$, $I_t = 0.08\text{nA}$), (c) graphene lattice breakdown at the ‘stitches’, ($V_b = 0.002\text{V}$, $I_t = 3.0\text{nA}$) and (d) a magnified image of graphene, ($V_b = 0.002\text{V}$, $I_t = 3.0\text{nA}$).

The magnified STM image in Figure 5.12 (c) shows the breakdown of the graphene lattice at boundaries between domains. This leads to a breakdown in the pristine graphene lattice and leads to imperfections, probably due to the growth dynamics when two islands meet. At these boundaries the detailed atomic structure cannot be identified. Figure 5.12 (d) shows the perfectly ordered graphene lattice which remains stable up to 800 °C. Figure 5.13 shows a FFT (taken using Figure 5.12 (d)) of graphene formed at 750°C and exhibits periodicities of 1.36 ± 0.05 nm, 0.39 ± 0.06 nm and 0.24 ± 0.05 nm. The latter periodicity is indicative of graphene (lattice parameter of graphene is 0.246nm) whereas the others can be attributed to the moiré superstructures observed throughout graphene domains^[13, 14, 15]. A moiré pattern is observed at this stage, similar to those observed on the Cu(111) surface. However, the periodicity here is 1.47 ± 0.05 nm. The lattice vectors of the Cu(110) surface are 0.256 nm and 0.361 nm while the lattice constant for graphene is 0.246 nm and it is this lattice mismatch which is the cause of the observed moiré structure throughout the graphene domains^[16]. The size of the periodicity generally depends on the orientation of the graphene in relation to the surface, the bias conditions between tip and sample, and also to the scanning direction of the STM tip.

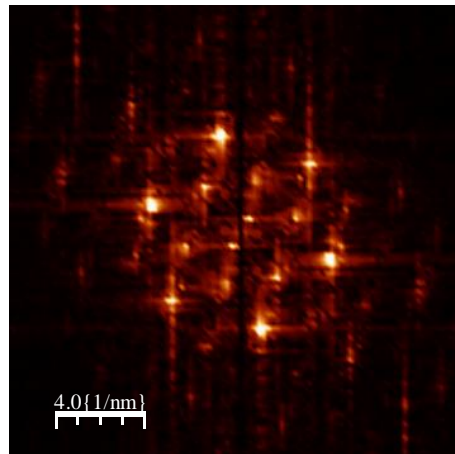


Figure 5.13: FFT of graphene image in Figure 5.12 (d) exhibiting three distinct periodicities.

A selection of images after annealing to 800°C show islands, boundaries, moiré patterns and graphene domains are shown in Figure 5.14. Figure 5.14 (a) shows large graphene domains with dimensions up to 60×40 nm. The domain boundaries are chemically

‘stitched’ together as seen in Figure 5.12 (b). The most common moiré pattern periodicities observed over all images are 1.33 ± 0.05 nm and 0.38 ± 0.08 nm as measured from FFT analysis. Figure 5.14 (b) and (d) show a large defect free graphene domain and magnified region respectively where the graphene hexagonal structure is observed throughout. Finally, Figure 5.14 (c) shows two graphene domains separated by an unresolved boundary and exhibit a moiré pattern with period of 1.30 ± 0.05 nm, orientated $138 \pm 3^\circ$ to each other.

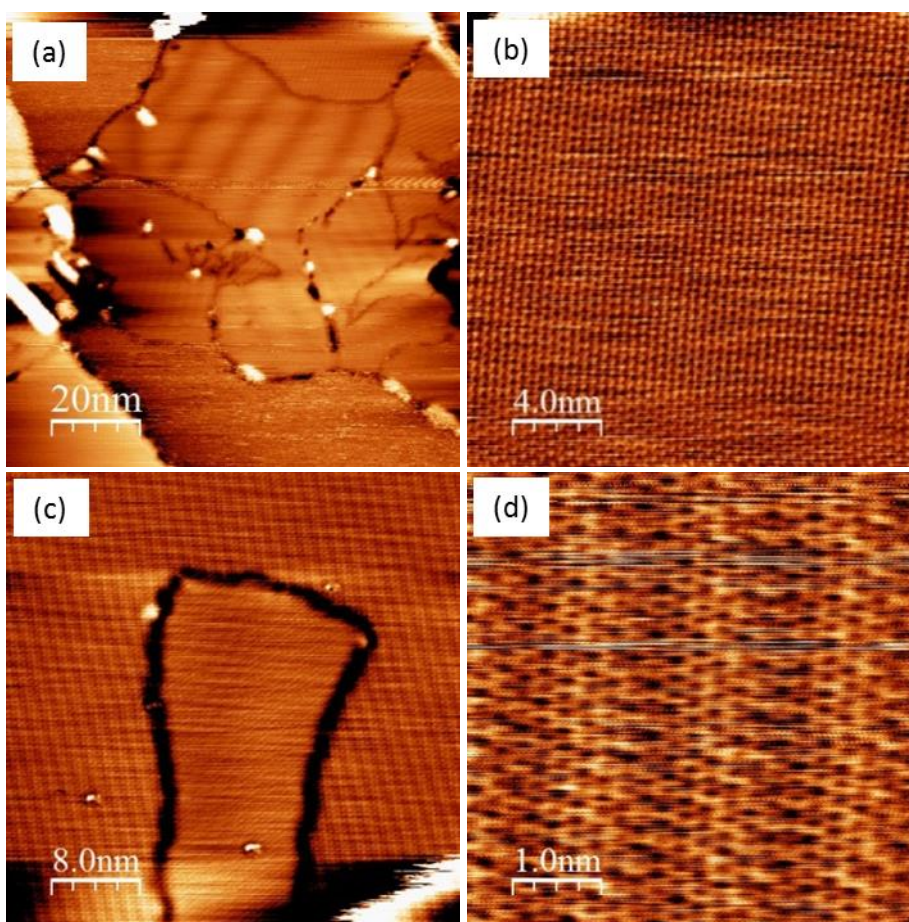


Figure 5.14: STM images after annealing the Cu(110) surface to 800°C. (a) Large scale image showing multiple graphene domains and boundaries, ($V_b = 1.0V$, $I_t = 1.0nA$), (b) magnified domain showing a relatively large defect free region, ($V_b = -0.04V$, $I_t = 30nA$), (c) a boundary defining the different orientations of a periodically equal Moiré pattern, ($V_b = 1.42V$, $I_t = 1.0nA$) and (d) magnified region of graphene showing the hexagonal graphene and moiré pattern ($V_b = -0.02V$, $I_t = 10nA$).

5.5 Summary

The main objective of this chapter was to investigate DBBA molecules on the Cu(110) surface. The molecules debrominate at RT and form chains similar to those on the Cu(111) surface. In this case, the chain growth is governed by the substrate which aligns the chains in the [001] direction as opposed to the multi directional chain growth on the Cu(111) surface. It has been shown that the most likely bonding arrangement at RT is an organo-metallic one (C-Cu-C) due to the molecular separation of 1.21 ± 0.05 nm. Annealing to 215°C alters the bianthracene units from tilted chains to flat lying, dehydrogenated molecules with a square appearance. The inter-molecular copper bonding is still present and bromine is observed between molecules. Molecular dimers orthogonal to the main growth direction are also observed. After a 235°C anneal, two different packing arrangements are observed which depends on the molecular density in these regions. In most cases, the molecules appear to be separated by two copper atoms which are preventing direct covalent bonding between DBBA molecules. It is shown in Figure 5.6 that a row of copper atoms along the [-110] direction separate each molecule in the chain and become involved in the C-Cu-C organo-metallic bonding. Between decomposition at 400°C and subsequently annealing to 800°C, it is possible that copper carbide initially forms before large domains of graphene become apparent upon reaching 750°C. Domains up to 60×40 nm are observed which are on occasions chemically ‘stitched’ at their boundaries where the graphene lattice breaks down. Moiré patterns with varying periodicities appear throughout the Cu(110)/graphene due to the lattice mismatch with the underlying Cu(110) surface.

5.6 References

- [1] Masonjones, M., Lafleur, A. & Sarofim, A. 1995, "Biarene formation during pyrolysis of a mixture of anthracene and naphthalene", *Combustion Science and Technology*, vol. 109, no. 1-6, pp. 273-285.
- [2] El Garah, M., MacLeod, J.M. & Rosei, F. 2013, "Covalently bonded networks through surface-confined polymerization", *Surface Science*, vol. 613, pp. 6-14.
- [3] Park, J., Kim, K.Y., Chung, K., Yoon, J.K., Kim, H., Han, S. & Kahng, S. 2011, "Interchain Interactions Mediated by Br Adsorbates in Arrays of Metal-Organic Hybrid Chains on Ag(111)", *Journal of Physical Chemistry C*, vol. 115, no. 30, pp. 14834-14838.
- [4] Walch, H., Dienstmaier, J., Eder, G., Gutzler, R., Schloegl, S., Sirtl, T., Das, K., Schmittel, M. & Lackinger, M. 2011, "Extended Two-Dimensional Metal-Organic Frameworks Based on Thiolate-Copper Coordination Bonds", *Journal of the American Chemical Society*, vol. 133, no. 20, pp. 7909-7915.
- [5] Di Giovannantonio, M., El Garah, M., Lipton-Duffin, J., Meunier, V., Cardenas, L., Revurat, Y.F., Cossaro, A., Verdini, A., Perepichka, D.F., Rosei, F. & Contini, G. 2013, "Insight into Organometallic Intermediate and Its Evolution to Covalent Bonding in Surface-Confined Ullmann Polymerization", *Acs Nano*, vol. 7, no. 9, pp. 8190-8198.
- [6] Fan, Q., Wang, C., Han, Y., Zhu, J., Kuttner, J., Hilt, G. & Gottfried, J.M. 2014, "Surface-Assisted Formation, Assembly, and Dynamics of Planar Organometallic Macrocycles and Zigzag Shaped Polymer Chains with C-Cu-C Bonds", *Acs Nano*, vol. 8, no. 1, pp. 709-718.
- [7] Gonzalez-Moreno, R., Sanchez-Sanchez, C., Trelka, M., Otero, R., Cossaro, A., Verdini, A., Floreano, L., Ruiz-Bermejo, M., Garcia-Lekue, A., Martin-Gago, J.A. & Rogero, C. 2011, "Following the Metalation Process of Protoporphyrin IX with Metal Substrate Atoms at Room Temperature", *Journal of Physical Chemistry C*, vol. 115, no. 14, pp. 6849-6854.
- [8] Hanke, F., Haq, S., Raval, R. & Persson, M. 2011, "Heat-to-Connect: Surface Commensurability Directs Organometallic One-Dimensional Self-Assembly", *Acs Nano*, vol. 5, no. 11, pp. 9093-9103.
- [9] Bondi, A. 1964, "van der Waals volumes and radii", *The Journal of physical chemistry*, vol. 68, no. 3, pp. 441-451.

- [10] Allen, F.H., Kennard, O., Watson, D.G., Brammer, L., Orpen, A.G. & Taylor, R. 1987, "Tables of bond lengths determined by X-ray and neutron diffraction. Part 1. Bond lengths in organic compounds", *J.Chem.Soc., Perkin Trans.2*, , no. 12, pp. S1-S19.
- [11] Li, X., Cai, W., An, J., Kim, S., Nah, J., Yang, D., Piner, R., Velamakanni, A., Jung, I., Tutuc, E., Banerjee, S.K., Colombo, L. & Ruoff, R.S. 2009, "Large-area synthesis of high-quality and uniform graphene films on copper foils", *Science (New York, N.Y.)*, vol. 324, no. 5932, pp. 1312-1314.
- [12] Gao, L., Guest, J.R. & Guisinger, N.P. 2010, "Epitaxial Graphene on Cu(111)", *Nano Letters*, vol. 10, no. 9, pp. 3512-3516.
- [13] Cho, J., Gao, L., Tian, J., Cao, H., Wu, W., Yu, Q., Yitamben, E.N., Fisher, B., Guest, J.R. & Chen, Y.P. 2011, "Atomic-scale investigation of graphene grown on Cu foil and the effects of thermal annealing", *ACS nano*, vol. 5, no. 5, pp. 3607-3613.
- [14] Malard, L., Pimenta, M., Dresselhaus, G. & Dresselhaus, M. 2009, "Raman spectroscopy in graphene", *Physics Reports*, vol. 473, no. 5, pp. 51-87.
- [15] Merino, P., Švec, M., Pinardi, A.L., Otero, G. & Martín-Gago, J.A. 2011, "Strain-driven moiré superstructures of epitaxial graphene on transition metal surfaces", *ACS nano*, vol. 5, no. 7, pp. 5627-5634.
- [16] Nünthel, R., Lindner, J., Pouloupoulos, P. & Baberschke, K. 2004, "The influence of substrate preoxidation on the growth of Ni on Cu (110)", *Surface Science*, vol. 566, pp. 100-104.

Chapter 6

An STM Study of Dibromodiphenyl Porphyrin (DBrDPP) on the Cu(110) surface

6.1 Introduction

Previous chapters have described the formation of covalently bonded networks by debromination reactions involving HBTP and DBBA organic molecules with six and two bromine atoms respectively. These molecules form nano-networks and nano-lines respectively via radical addition following debromination. The same reaction strategies can be employed with porphyrin molecules to form covalent porphyrin networks on surfaces. Grill *et al.* have shown that iodine and bromine functionalised porphyrins undergo thermal activation which leads to covalently bonded nano-line formation after dehalogenation. Lipton-Duffin *et al.* have successfully grown polyphenylene chains on the Cu(110) surface by dehalogenation of 1,4-diiodobenzene and 1,3-diiodobenzene where the Cu surface acts as a template, providing catalytic sites to dissociate iodine. This creates a radical and hence a pathway for covalent bonding to occur ^[1]. Hanke *et al.* observed copper surface atoms partaking in the reaction process between adjacent non functionalised Cu-porphyrins after debromination in a C-Cu-C bonding arrangement. Further studies of porphyrins extend to observations of a Ni-Cu exchange in the macrocycle core of DBrDPP ^[2] while Diller *et al.* have reported on the adsorption and self-metalation of a prototypic tetrapyrrole free base porphyrin on the Cu(111) surface ^[3].

This chapter investigates the stages from room temperature deposition to chemically stable, covalently bonded networks using Ni(II) 5,15-dibromo-10,20-diphenyl porphyrin (DBrDPP), the structure of which is presented in Figure 6.1. The study here extends to the Cu(110) surface which has a higher reactivity than the (110) surfaces of silver or gold ^[4] and is chosen in the hope that the (110) surface should encourage the linear growth of porphyrin chains.

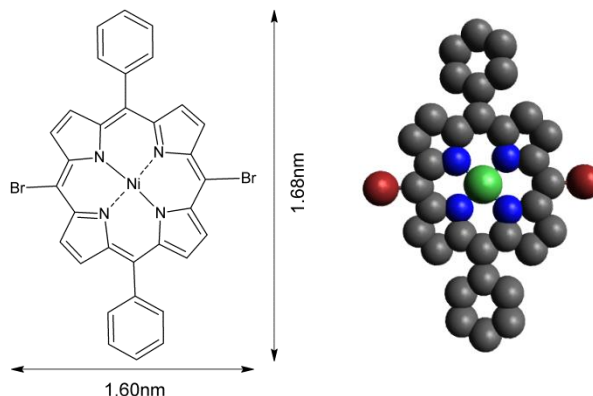


Figure 6.1: Structure of DBrDPP, dimensions determined from Chems sketch. Hydrogen atoms are not shown. Ball and stick arrangement for DBrDPP.

6.2 STM Study of DBrDPP on the Cu(110) Surface at Low Coverage

RT deposition of ~ 0.1 ML of DBrDPP on the Cu(110) surface, using the same procedures as discussed and used throughout these experiments, resulted in molecular mobility which in turn, made it impossible to obtain molecular resolvable STM images. For this reason, the surface was annealed to 100°C and typical STM images are shown in Figure 6.2.

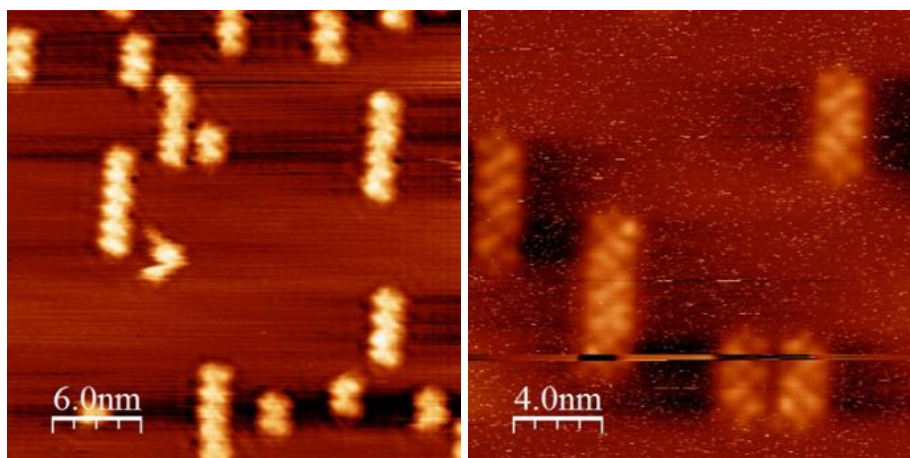


Figure 6.2: STM images of 0.1 ML of DBrDPP deposited on RT Cu(110) at different bias. ($V_b = 0.39\text{V}$, $I_t = 1.82\text{nA}$) and ($V_b = 0.69\text{V}$, $I_t = 0.054\text{nA}$).

Bromine has dissociated from the molecule enabling porphyrin chains to grow via new bonding sites (free radicals) of the molecule. These regular nanolines grow in one direction

and are up to 14 molecular units long. The centre to centre distance along the nanolines is 1.09 ± 0.05 nm, (calculated using line profile and averaging methods), in agreement with an expected distance of 1.08 nm if copper adatoms are involved in the bonding. This type of C-Cu-C bonding has been reported previously; Raval *et.al.* reported on the covalent self-assembly process for porphyrin molecules on Cu(110) where the surface plays a pivotal role. An organo-metallic C-Cu-C coupling is observed between porphyrins and alignment and preferential growth along the [001] direction ^[5]. The nanolines here are predominantly straight and parallel to one another with an occasional off-set or kink, caused by position of the copper atoms in the proposed C-Cu-C bridging bond(s) between adjacent porphyrins. This small proportion of irregular bonding within the linked nanolines suggests that a number of alternative bonding configurations are available to the porphyrins depending on their interaction and alignment during the reaction phase after debromination has occurred. The phenyl rings are orientated parallel to each other and appear as bright lobes along the edges of the chains. It is unclear from the STM images shown in Figure 6.2 how many copper adatoms are taking part in the reaction. Evidence of molecular movement is observed during STM image acquisition where a porphyrin molecule is seen migrating towards a previously established and stable chain. This could be explained via the electric field interaction between the solitary molecule and tip enabling movement. Three STM images in Figure 6.3 show this movement and final alignment with the chain.

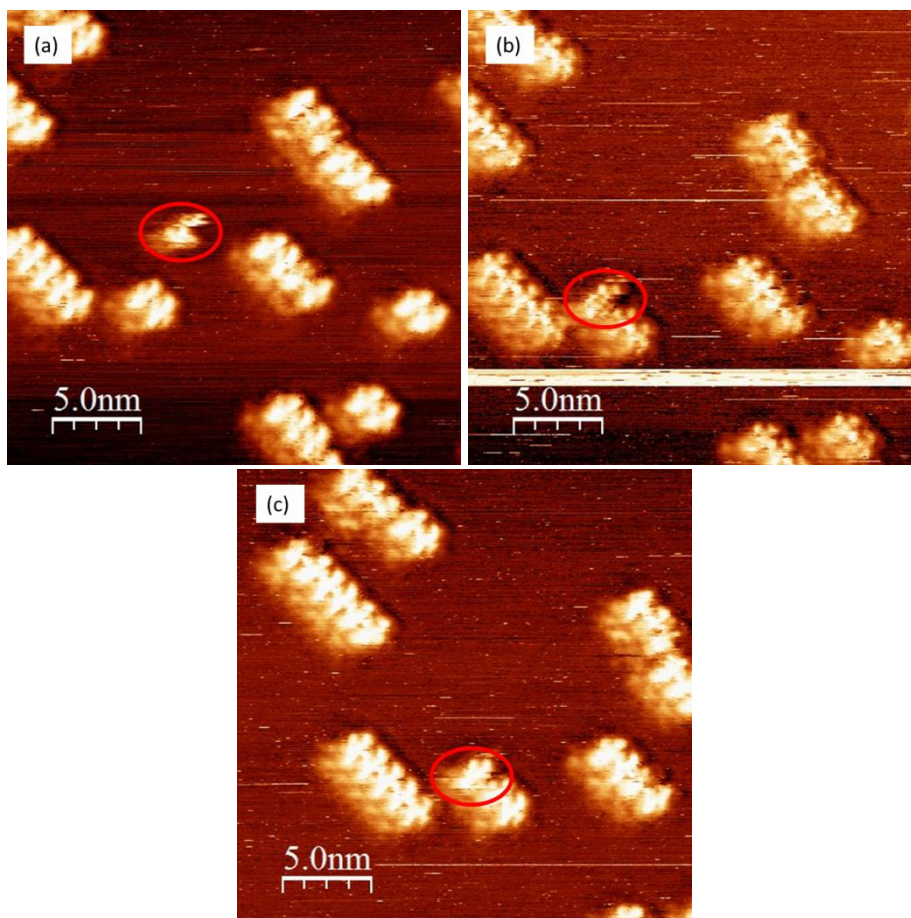


Figure 6.3: STM images of the same 25×25 nm area taken within a 5 minute period of each other showing a single porphyrin molecule migrating towards and bonding to an already established chain, (a) ($V_b = 0.07V$, $I_t = 0.05nA$), (b) ($V_b = 0.03V$, $I_t = 0.05nA$) and (c) ($V_b = -0.03V$, $I_t = 0.05nA$). Note the STM tip change in the lower quadrant of (b) and extreme bottom of (c).

Higher resolution images of the porphyrin chains were obtained after annealing to $200^\circ C$ and are shown in Figure 6.4 (a) and (d). The images show a range of lengths of up to 15nm (not shown). The Cu(110) rows are visible in Figure 6.4 (b) which confirms an alignment of the linear networks in the [001] direction. The molecules show a bright central protrusion and their phenyl rings lie along the edges of the chains, pointing in the [-1,10] direction as indicated. In most cases, a copper atom is observed centrally between the porphyrins in each chain. However, the slight offset and different position of the last porphyrin in the chain in Figure 6.4 (b), and last two porphyrins in Figure 6.4 (e) (highlighted with a red arrow in both), indicate a different C-Cu-C bonding. The bonding of

the chain in Figure 6.4 (b) and (e) are shown schematically in Figure 6.4 (c) and Figure 6.4 (f) respectively. It appears that porphyrins in these chains exhibit the loss of bromine and hydrogen atoms between DBrDPP molecules as centre-to-centre distances indicate that they have been replaced by copper adatoms. This type of bonding has previously been observed by Haq *et al.* and Hanke *et al.* ^[5, 6]. Figure 6.4 also shows two molecular models with the proposed arrangement of the porphyrin molecules and Cu atoms in the DBrDPP chains.

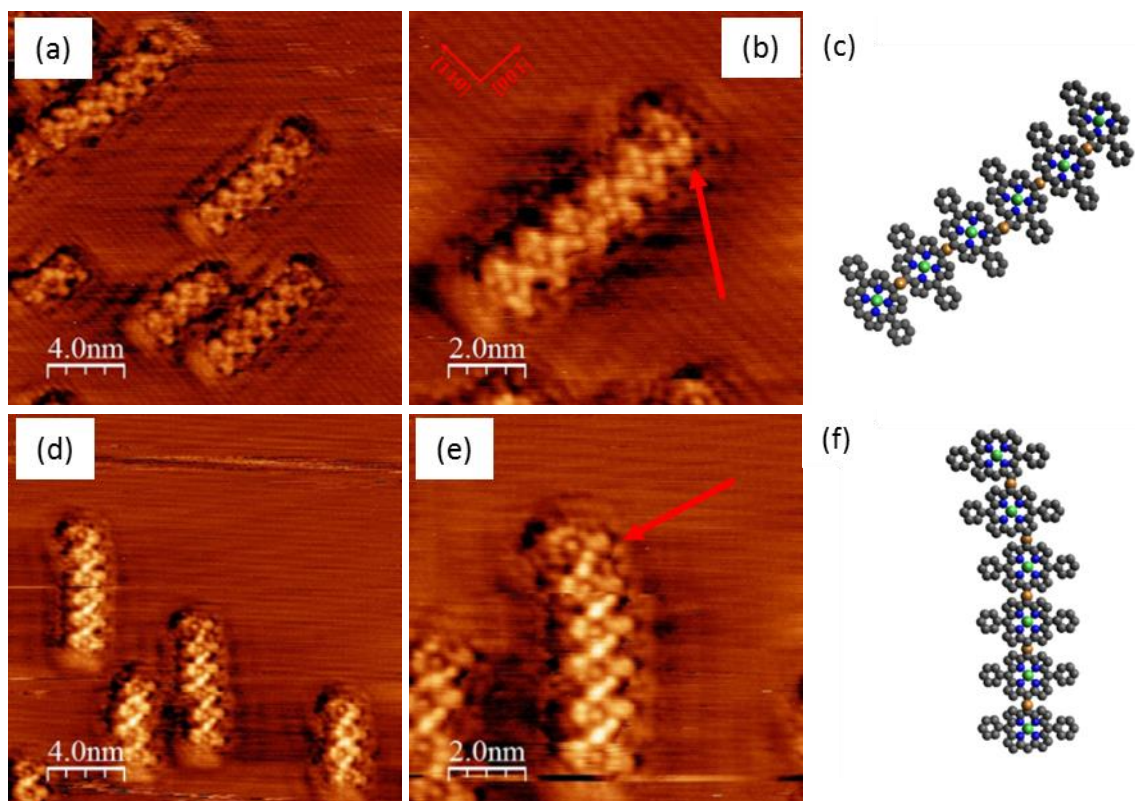


Figure 6.4: STM images and schematics of the DBrDPP chains and organo-metallic bonding. (b) is a magnified image of (a) ($V_b = 1.19\text{V}$, $I_t = 0.27\text{nA}$) where a DBrDPP molecule is offset from the chain, the bonding arrangement is shown in (c). (e) is a magnified image of (d) ($V_b = 1.19\text{V}$, $I_t = 0.27\text{nA}$) where a DBrDPP molecule is offset from the chain and a tip change occurs near the bottom of the image. The bonding arrangement is shown in (f).

The centre to centre distance measured from Figure 6.4 (b) and confirmed using measurements from Figure 6.4 (e) is 1.11 ± 0.05 nm in agreement with the 100°C anneal stage. Again this is attributed to copper adatoms forming an organo-metallic bond with DBrDPP and subsequent chain formation as described above. Without complimentary

information such as PES it cannot be said with certainty that the central lobe is nickel or copper. However, previous studies suggest that a Ni-Cu ion exchange occurs at these temperatures on copper surfaces ^[2, 3, 7]. Doyle *et al.* observed the Ni ions in the DBrDPP macrocycle core react with the Cu(111) surface at RT and are replaced by copper atoms from the surface.

Annealing to 250°C reveals similar nanolines but with significant change in the appearance of the macrocycle centre. These results are shown in Figure 6.5 where some central cores appear as bright protrusions (white arrows in Figure 6.5 (b)) while others exhibit a depression (red arrows in Figure 6.5 (b)). There are three possible explanations for this phenomenon: (i) the bonding between adjacent porphyrin molecules distorts the geometry of the macrocycle due to an alteration in the electron density of the central core, which then appears as a depression; (ii) the central nickel atom has been displaced from the core and it is possible that hydrogen atoms protonate and stabilise the porphyrin; (iii) Ni/Cu ion exchange has occurred and the porphyrin molecules now have a copper metallised centre. Similar reports have been published by Doyle *et al.* and Röckert *et al.* of macrocycle metalation via porphyrin and copper substrate interaction ^[2, 8]. The former observed the previously mentioned Ni-Cu exchange for DBrDPP and also for Ni(II) (5,10,15,20-tetrakis-(4-bromophenyl)porphyrinato) (NiTBrPP) on the Cu(111) surface. Röckert *et.al.* reported on the self-metalation of 2H-tetraphenylporphyrin (2HTPP) with copper on Cu(111) at ~130°C ^[8].

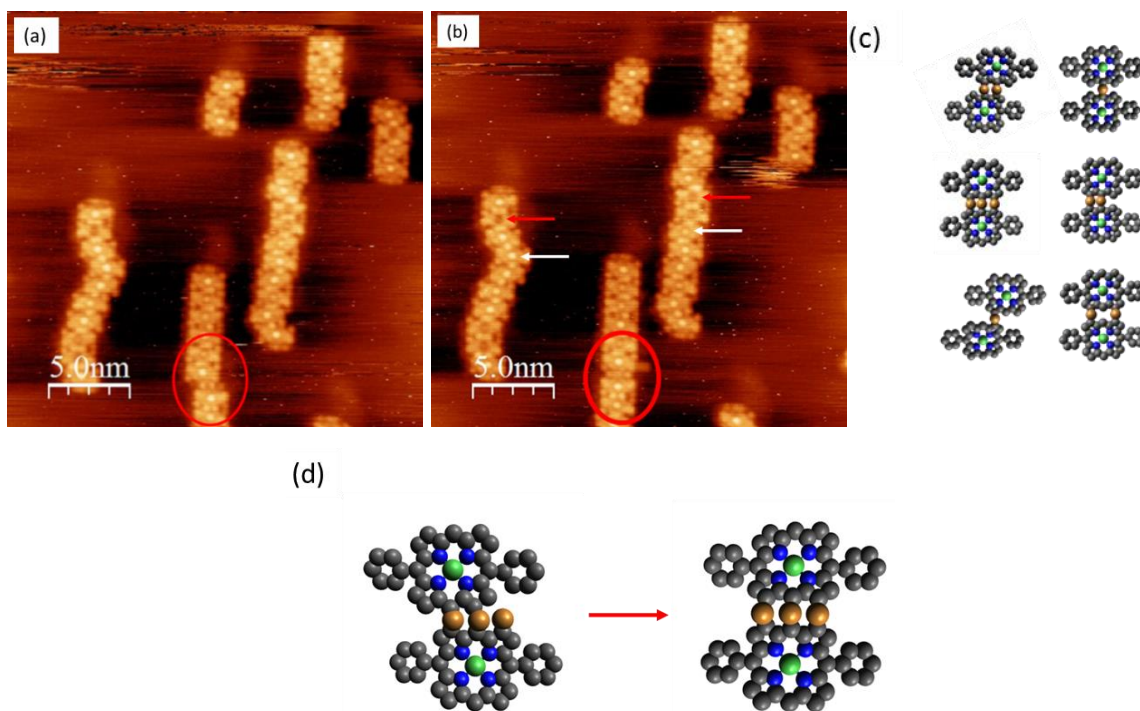


Figure 6.5: STM images (a) ($V_b = -0.91V$, $I_t = 0.39nA$) and (b) ($V_b = -0.83V$, $I_t = 0.45nA$) showing chain alignment, (c) all possible C-Cu-C organo-metallic bonding preferences and (d) a schematic showing the movement of DBrDPP circled in the STM images.

An offset chain is visible, circled in red in Figure 6.5 (a). Scanning the same area, after approximately 5 minutes, shows that this kink is no longer present (see Figure 6.5 (b)) and the porphyrins are aligned. This sliding effect along the copper rows confirms the molecular diffusion seen previously in Figure 6.3 but this time at higher resolution, where the copper adatoms are visible during this alignment of two chains. The mobility of the DBrDPP molecules is direct evidence that the observed structures are protopolymers, as this kind of free moving molecule would not occur if the porphyrins were covalently bonded.

At this stage, from our understanding of previous results i.e. DBBA on Cu(110), intra molecular cyclodehydrogenation would be expected to have taken place between neighbouring DBrDPP subunits. However, the expected cyclodehydrogenation is prevented by the intervening copper atoms. Evidence of this is the 1.18 ± 0.02 nm measured distance between molecules, a larger distance than that expected if carbon-carbon bonds had formed between the porphyrin molecules. This is further evidence of a C-Cu-C phase. Observations

of a depression in the centre of the macrocycle in some of the porphyrins in the chains, leads to the hypothesis that a partial copper-nickel exchange has occurred at this temperature, as previously reported by Doyle *et al.* ^[2]. At this stage ~20% of porphyrins molecules show a central depression and these molecules are associated with Cu metalation. Doyle *et al.* reported that this exchange occurs at RT and after annealing to ~160°C, 20% of nickel atoms were displaced by copper atoms.

Figure 6.6 shows an STM image after annealing to 300°C where further changes have occurred in the structure of the molecular rows. The most significant change observed is that all the porphyrins appear to have dark depressions in the centre of the macrocycle. Previous studies indicate that the Ni-Cu macrocycle core exchange occurs below 300°C which would imply that the bias conditions of the STM tip relative to the surface create this dark depression effect.

The chains remain intact where lengths of up to 10 nm are observed, comparable to those found after annealing to 250°C.

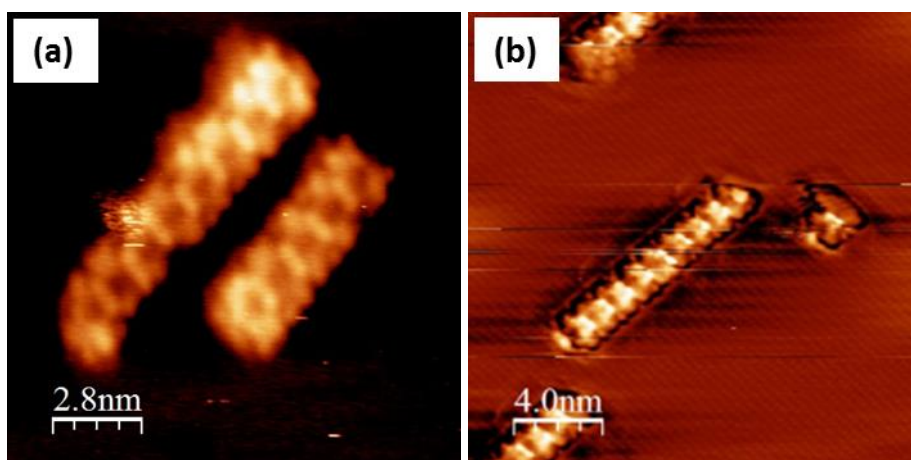


Figure 6.6: STM images of a post 300°C anneal of DBrDPP on the Cu(110) surface (a) exhibits the ‘vacant’ macrocycle core, ($V_b = -1.31V$, $I_t = 0.08nA$) and (b) 10 nm chains are still observed, ($V_b = -0.44V$, $I_t = 0.30nA$).

Furthermore, the average distance between the centres of the porphyrins at this stage is 1.13 ± 0.02 nm, which suggests that no direct covalent bonding between the porphyrin molecules has taken place and copper adatoms are still playing a role in the stabilisation of the chains and prevention of cyclodehydrogenation.

Figure 6.7 shows the surface after annealing to 350°C. The organo-metallic chains have started to decompose although the original linear structures are still visible along the step edges, highlighted by the red arrow. Intact porphyrins are still identifiable and are highlighted by a white arrow in Figure 6.7.

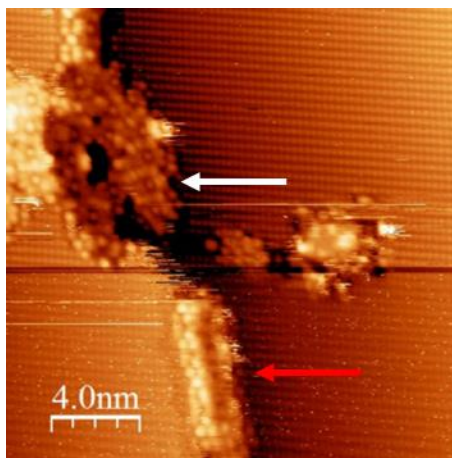


Figure 6.7: STM image of the initial stages of DBrDPP nanoline decomposition (red arrow) and intact porphyrins (white arrow), ($V_b = -1.71V$, $I_t = 1.07nA$).

6.3 STM Study of DBrDPP on the Cu(110) Surface at High Coverage

After deposition of $\sim 0.9ML$ of DBrDPP at RT and subsequent annealing to 105°C, the structures presented in Figure 6.8 were observed. The porphyrins align predominantly along the [001] crystalline direction. The closest centre to centre distances at this stage are 1.23 ± 0.05 nm. This can be attributed to a C-Cu-C bonding between the porphyrin molecules, in close agreement to previously reported organo-metallic bonding on copper surfaces^[5, 6, 9]. It is possible that bromine is interfering with the network formation as it is known from previous experiments that it dissociates in the temperature range RT - 100°C but does not desorb from copper surfaces until temperatures in excess of 300°C are reached.

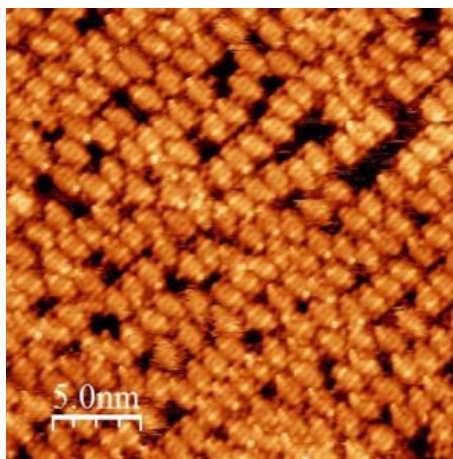


Figure 6.8: STM image after annealing to 105°C from RT deposited DBBA molecules, ($V_b = -1.45V$, $I_t = 1.50nA$).

There are two bromine atoms per molecule so it would be possible to say that some of these bright intermolecular lobes are the dissociated bromine atoms. The majority of these intermolecular bright lobes are assigned to copper adatoms which diffuse over the surface creating a larger than expected separation between the DBrDPP molecules.

When the molecules are tightly packed they exhibit a centre to centre distance of 1.23 ± 0.05 nm which would suggest that this distance would cover three copper [001] rows in the underlying substrate. Furthermore, a central copper adatom acts as the linking bond between adjacent porphyrins. Line profile measurements taken from numerous porphyrin chains provide an average distance between rows of 1.58 ± 0.08 nm. This is in close agreement to the width between phenyl groups from the predicted model (1.68 nm) as shown in Figure 6.1. This measurement would imply that an individual DBrDPP molecule covers six copper substrate atoms in the [-110] direction from phenyl ring to phenyl ring. A schematic of this molecular arrangement is shown in Figure 6.9.

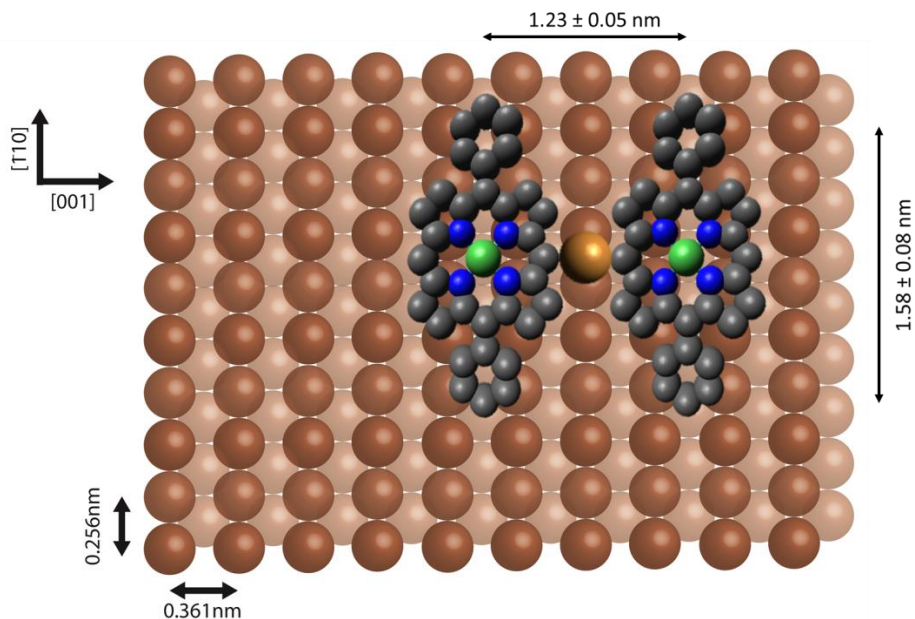


Figure 6.9: Schematic diagram showing the arrangement of two DBrDPP molecules on the Cu(110) surface. In this case, a single C-Cu-C bond has formed.

Annealing this surface to 255°C results in an improved alignment of the molecules along the [001] direction of the Cu(111) surface as observed in Figure 6.10 (a). Larger centre to centre distances, averaging to 1.49 ± 0.02 nm, are observed between the molecules (see three red dots) suggesting that adjacent porphyrins are not bonded. In most cases where the porphyrin subunits align perfectly, between one and three copper adatom(s) separate the porphyrins and it appears that bonding between carbon from the macrocycle and copper atoms has occurred in certain cases (see red circle in Figure 6.10 (b)). The average centre to centre distance in these cases is 1.18 ± 0.05 nm indicating that the DBrDPP molecules are packing more tightly together.

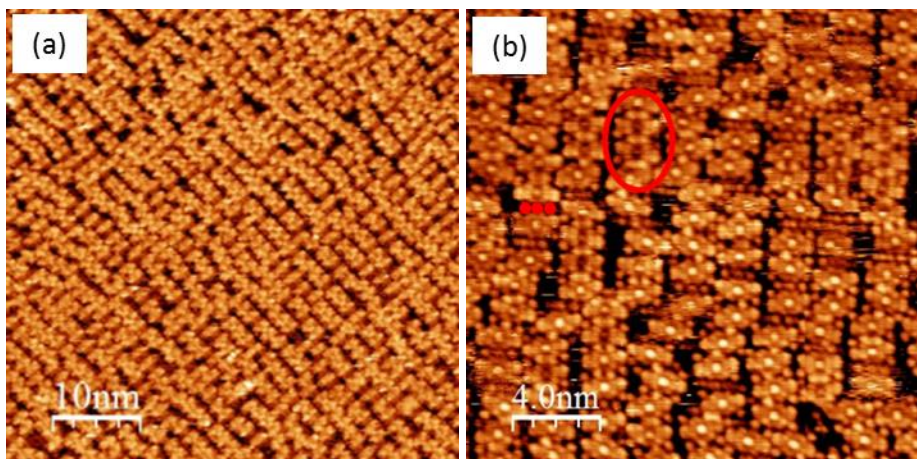


Figure 6.10: STM images post 255°C anneal showing (a) a more ordered alignment of the molecules in the [001] direction, ($V_b = 0.74V$, $I_t = 1.06nA$) and (b) the different bonding where 3 copper atoms create a larger molecular separation (red dots) and where C-Cu-C bonds enable closer centre to centre distances to be observed, ($V_b = -1.37V$, $I_t = 1.03nA$).

The closest centre-to-centre distance is 1.07 ± 0.02 nm and in these cases it appears that intermolecular bonding has occurred, however, this bonding is indicative of a C-Cu-C organo-metallic arrangement rather than a C-C direct porphyrin to porphyrin bonding. This is in close agreement with previously documented centre to centre distances between Zn(II) diphenyl porphyrins on Cu(110) of 1.08 nm reported by Haq *et al.* [5].

There are a few instances where a nickel-copper ion exchange (in the centre of the porphyrin) has occurred as highlighted in the red circle in Figure 6.10 (b). This exchange coincides with the formation of C-Cu-C bonds between adjacent molecules as opposed to the three copper spacing atoms (red dots in Figure 6.10 (b)) which create a larger separation between DBrDPP units. When these spacer adatoms are present, it is proposed that no metallic exchange has occurred. This observation was also observed at low coverages (Figure 6.5 and Figure 6.6). Approximately 80% of the DBrDPP molecules are separated by copper atoms and the remainder have bonded in the organo-metallic arrangement. It appears that the macrocycle is enlarged for those molecules which exhibit the organo-metallic bonding but this is most likely a tip effect or possibly due to metalation altering the electron density of the macrocycle.

Annealing to 300°C results in approximately 95% of porphyrin molecules engaging in the organo-metallic bonding and 100% have undergone a nickel-copper exchange. This

exchange and bonding is observed in Figure 6.11 and confirmed from previously reported literature [2, 3, 5, 6, 9, 10, 11].

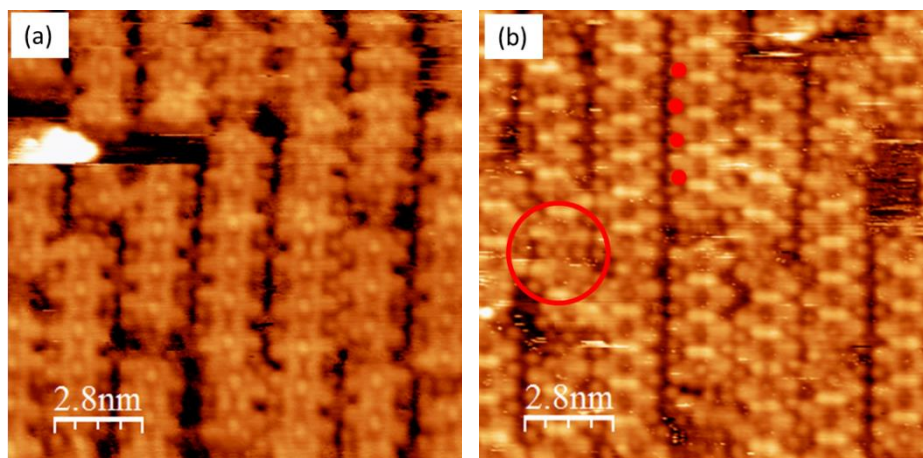


Figure 6.11: STM images after annealing to 300°C exhibiting differences in the macrocycle core (a) ($V_b = -2.18V$, $I_t = 1.68nA$) and (b) ($V_b = 0.06V$, $I_t = 1.32nA$)

Figure 6.11 shows the contrast change in the copper centre of the molecules when the STM tip/sample bias is altered from negative to positive ((a) to (b)). The copper centre appears in every DBrDPP core in Figure 6.11 (a) and appears vacant in Figure 6.11 (b). This is due to the positive and negative bias conditions which differ between the images.

The average centre to centre distance along the rows is 1.23 ± 0.02 nm while the distance between adjacent rows is 2.26 ± 0.02 nm (WSxM line profile calculations). The most common distance between DBrDPP molecules exhibiting the C-Cu-C bonding arrangement is 1.09 ± 0.02 nm. Furthermore, copper atoms are now observed between adjacent rows appearing as bright spots between the phenyl rings and are highlighted as red dots in Figure 6.11 (b). These are copper adatoms aligned along the [-110] direction and are separated by 1.09 ± 0.02 nm indicating that the porphyrins cover four copper atoms in the [001] direction and not three as stated previously. This more accurate molecular arrangement is shown in Figure 6.12.

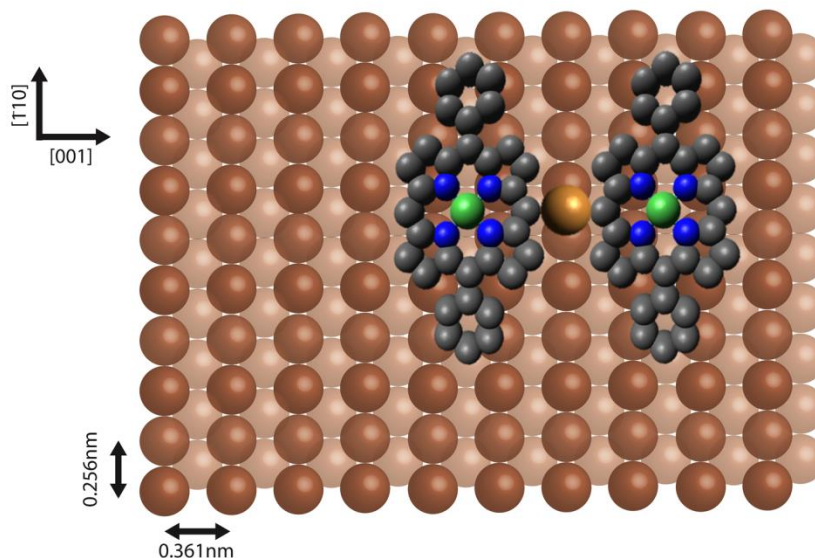


Figure 6.12: Schematic diagram showing a more accurate arrangement of two DBrDPP molecules on the Cu(110) surface. In this case, a single C-Cu-C bond has formed.

Figure 6.13 shows STM images of the same surface after annealing to 350°C where chains are still observed (a), (b) and (c). The distance between adjacent rows is 1.71 ± 0.02 nm and topographically, the phenyl rings appear 60 ± 2 pm above the surface, indicating a non-planar twisting or tilting. It is possible that partial dehydrogenation has occurred between phenyl rings allowing them to form cross row covalent bonds. The copper atoms within the macrocycle appear approximately 50 ± 2 pm above the surface and topographically, appear to be more elevated than the macrocycle itself. This could be attributed to an electron density effect rather than a topographical one.

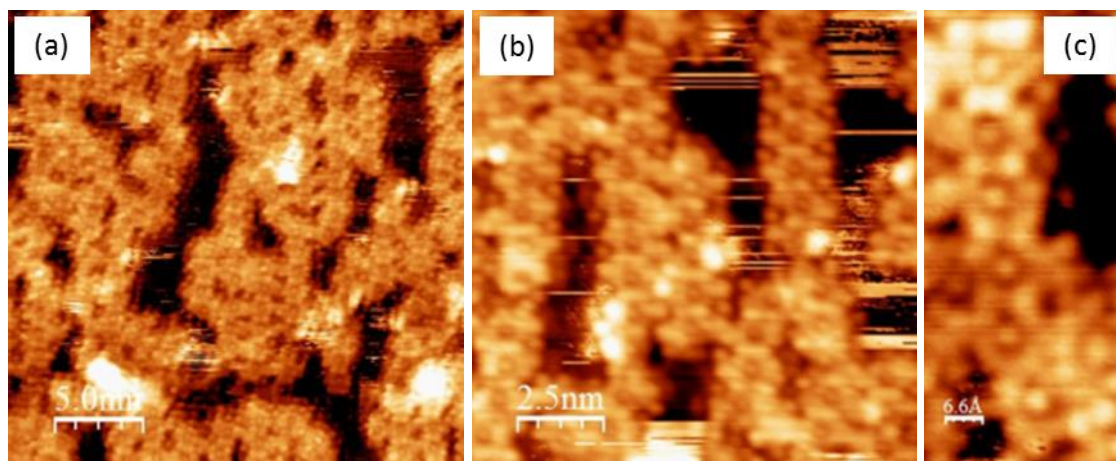


Figure 6.13: STM images after annealing to 350°C. (a) and (b), large scale and magnified images respectively, ($V_b = -0.62\text{V}$, $I_t = 1.68\text{nA}$) and ($V_b = 1.00\text{V}$, $I_t = 1.47\text{nA}$) and (c) Further magnification of a chain, ($V_b = -1.93\text{V}$, $I_t = 2.20\text{nA}$).

Annealing to 400°C results in no discernable change in the linear chains as shown in Figure 6.14. The linearly ordered structures are visible albeit at poor STM imaging resolution.

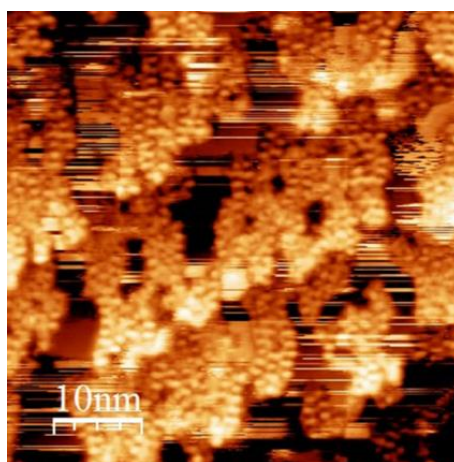


Figure 6.14: STM image post 400°C anneal. Rows of molecules are still present on the Cu(110) surface, ($V_b = 0.87\text{V}$, $I_t = 0.02\text{nA}$).

After annealing to 500°C islands of decomposed porphyrin material, 80 ± 2 pm in height, become prominent and there is no longer evidence of the previously seen chains. Moreover, there is no evidence for the trenches which were observed for the DBBA/Cu(110) at these temperatures. This leads to a need for further investigation to ascertain whether copper carbide islands are being formed.

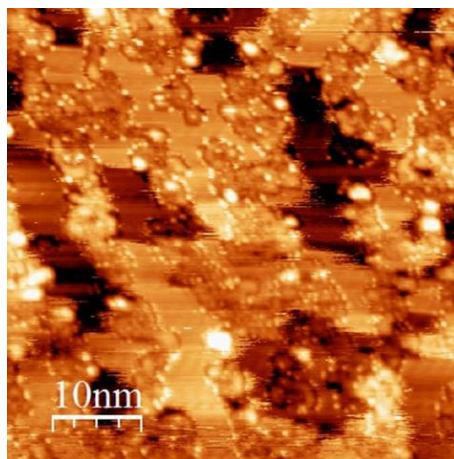


Figure 6.15: STM image showing decomposition after annealing the Cu(110) substrate to 500°C, ($V_b = -1.48V$, $I_t = 0.11nA$).

Figure 6.16 shows an STM image after annealing the surface to 700°C. Large irregularly shaped islands, up to 40nm in width, have formed. The islands observed have become smoother and more distinguishable to those observed in Figure 6.15.

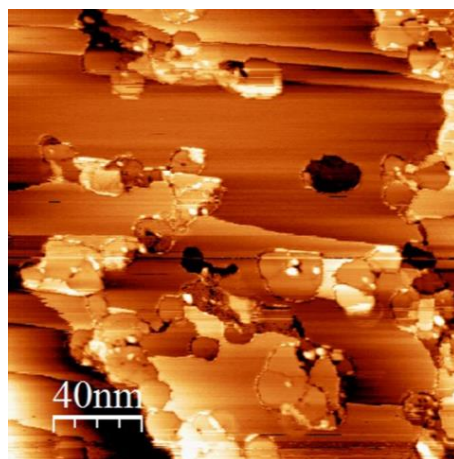


Figure 6.16: STM image of graphene island formation on the Cu(110) substrate after annealing to 700°C, ($V_b = 1.0V$, $I_t = 0.1nA$).

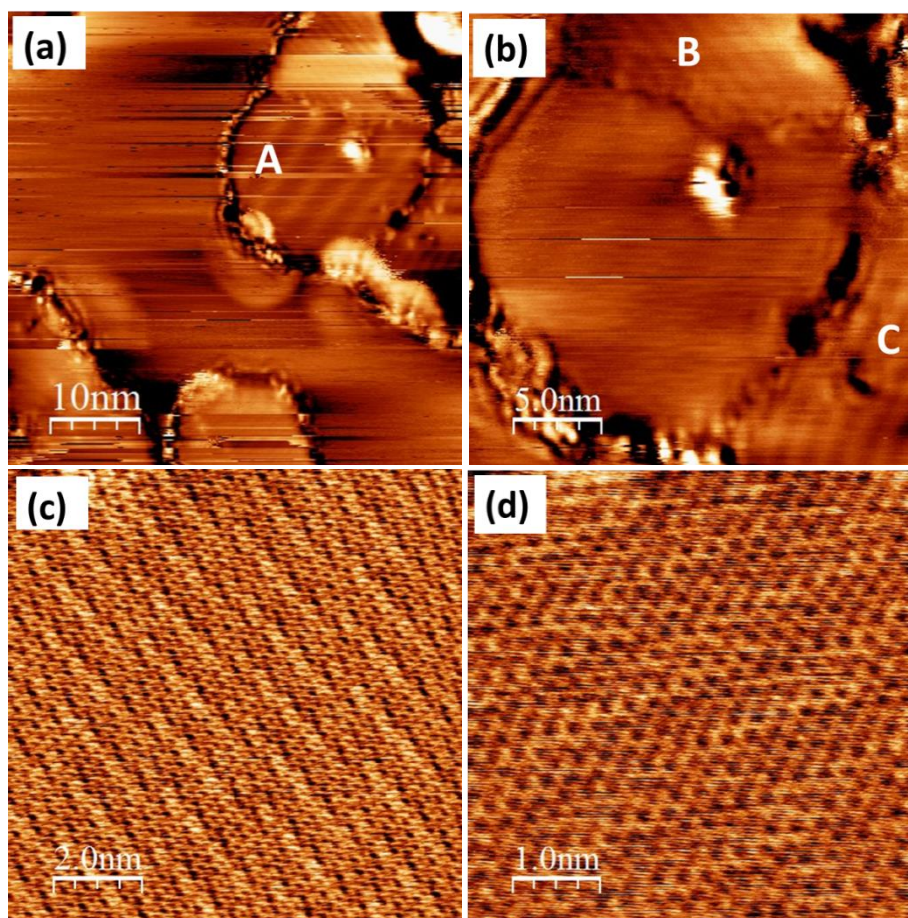


Figure 6.17: STM images showing graphene domains through subsequent magnifications. (a) showing large periodicity 'A', ($V_b = 0.02V$ $1.00V$, $I_t = 0.10nA$), (b) shows smaller periodicity at different orientations, 'B' and 'C' ($V_b = 0.02V$ $1.00V$, $I_t = 0.10nA$), (c) and (d) showing highly magnified graphene domains exhibiting hexagonal lattice, ($V_b = 0.02V$, $I_t = 1.00nA$) and ($V_b = 0.03V$, $I_t = 4.00nA$) respectively.

Upon closer inspection and magnification of these islands, interesting features become apparent as shown in Figure 6.17. Figure 6.17 (d) shows a 5×5 nm STM image of one of these islands where measured pore to pore distances are 0.248 ± 0.06 nm indicative of graphene (the lattice constant of graphene is 0.246 nm). Perfectly ordered domains of graphene are observed with domain dimensions of up to $\sim 40 \times 40$ nm. In most cases, the well-ordered graphene domains exhibit a moiré pattern associated with a lattice mismatch between the graphene (0.246 nm) and the underlying Cu(110) substrate (0.256 nm). In some cases, no such moiré pattern is observed which is probably due to the orientation of the structure relative to the STM tip scanning direction. This has previously been reported by Goa *et al.* who observed similar graphene structures on the Cu(111) surface ^[12]. Ripples

are observed with different periodicities and this is attributed to the graphene growth in different directions with respect to the underlying substrate ^[13]. The minimum and maximum periodicities observed here are 1.15 ± 0.05 nm and 3.39 ± 0.05 nm respectively (domain A being the largest and domains B and C the smallest). The angle between the directions of the rippling patterns in domains ‘B’ and ‘C’ in Figure 6.17 (b) is $116^\circ \pm 5^\circ$. Line profile measurements between neighbouring carbon rings of graphene in the magnified STM image in Figure 6.18 (a) are 0.25 ± 0.02 nm. Measurements taken from a FFT image of a graphene domain (see Figure 6.18 (b)) results in periodicities of 0.25 ± 0.01 nm (graphene), 0.71 ± 0.01 nm, (this exact periodicity has been reported by Tapaszto *et al.* ^[14]) and 2.63 ± 0.30 nm, which coincides with the line profile measurements.

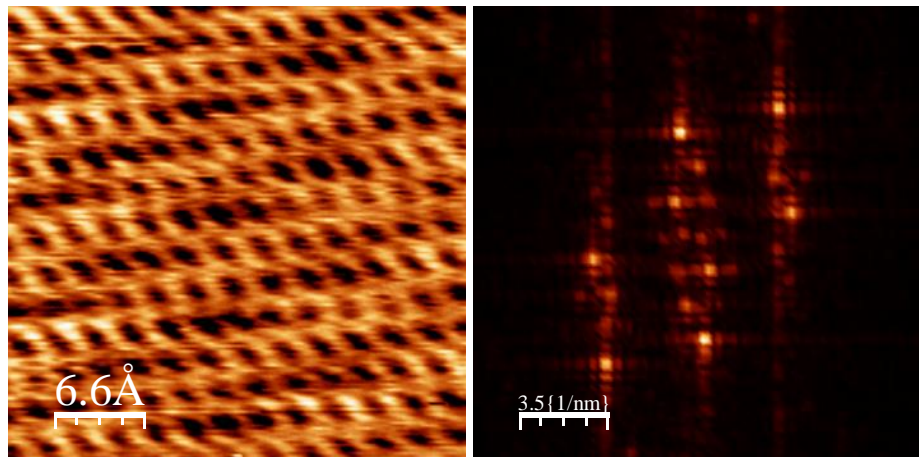


Figure 6.18: Magnified STM image showing the hexagonal carbon lattice structure of graphene and the corresponding FFT, ($V_b = -0.02$ V, $I_t = 1.75$ nA).

In order to test the stability of these graphene islands, the sample was annealed to 800°C . The STM images of this anneal stage (Figure 6.19) shows that graphene domains are still present (Figure 6.19 (a)), albeit larger, with dimensions up to 100×40 nm. The STM image in Figure 6.19 (b) shows an example of the moiré pattern and in this case exhibits a different periodicity than previously observed, 1.30 ± 0.05 nm. There are additional measured from the same image; 0.33 ± 0.05 nm and 0.25 ± 0.05 nm. These are in close agreement to periodicities measured from the FFT image in Figure 6.19 (c); 1.21 nm, 0.376 nm and 0.235 nm. An interesting feature is the emergence of multiple layers of

graphene stacked together i.e. graphite (Figure 6.19 (d)). Successive magnifications at different orientations to the original graphite flake (insets of Figure 6.19 (c)) are also shown to emphasise the hexagonal features of the individual graphene lattices. These 8 ‘step-like’ sheets of graphene have an apparent height of 80.0 ± 0.5 pm. Generally, the apparent height of the graphene above the underlying substrate, averaged over several domains, is 20.0 ± 0.5 pm and in some cases, two layers are observed with heights of 40.0 ± 0.5 pm. This leads to the conclusion that the graphene layers in this 8 ‘step-like’ graphite flake pack more closely together, perhaps due to a strong π bonding interaction.

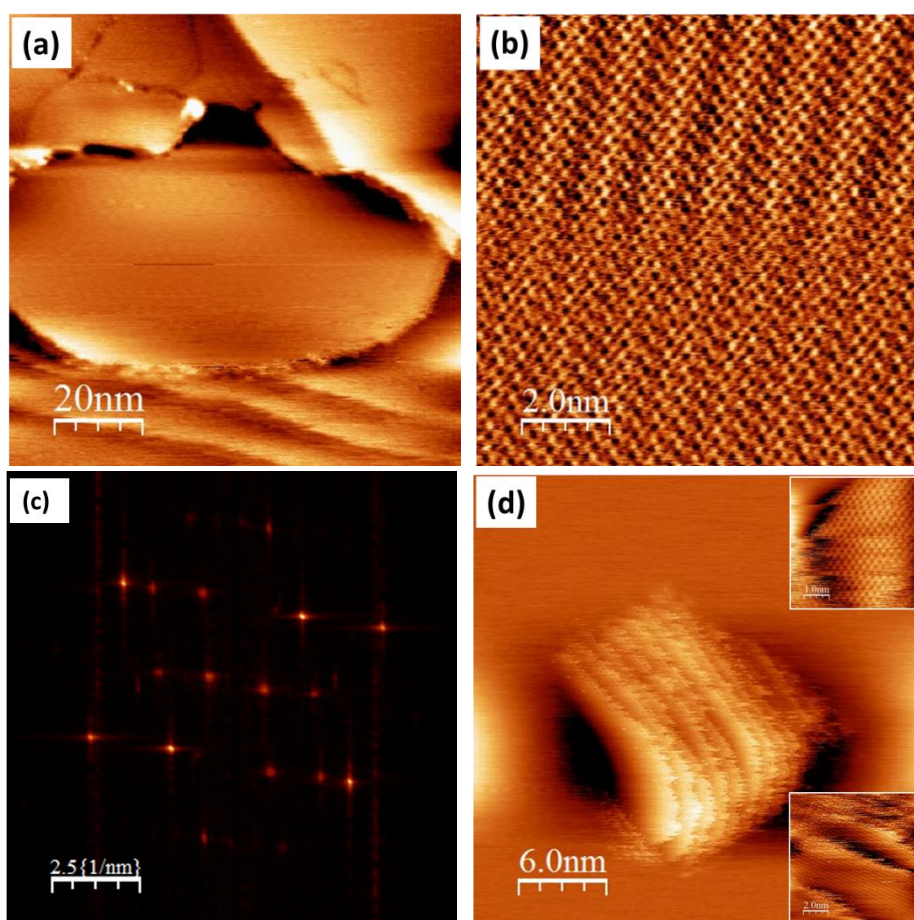


Figure 6.19: STM images showing (a) large graphene domains, ($V_b = 1.00V$, $I_t = 1.00nA$), (b) and (b) magnified graphene domain to emphasise the hexagonal lattice and moiré pattern with (c) corresponding FFT, ($V_b = -0.02V$, $I_t = 20.00nA$) and (d) observation of graphite, ($V_b = 0.02V$, $I_t = 2.50nA$).

Defects occasionally appear on some of the graphene islands as shown in Figure 6.20 and are due to atomic irregularities within the graphene lattice itself occurring during the formation process. These defects, which appear topographically as mounds 10.0 ± 0.5 pm higher than the rest of the graphene sheet, are accompanied by distortions in the lattice and contribute to an increase in the local density of states in the regions of defection and hence appear as brighter features in the image ^[15].

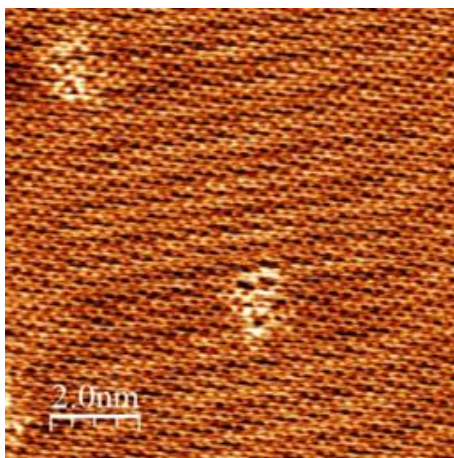


Figure 6.20: STM image of a graphene domain exhibiting defects in the layer, ($V_b = 0.02V$, $I_t = 1.00nA$).

Further experiments were carried out to investigate whether graphene nanoribbons could be fabricated between the graphene islands by addition of DBBA molecules and the subsequent anneal stages described in Chapter 5. Figure 6.21 shows DBBA deposited at room temperature onto the graphene/Cu(110) surface described above.

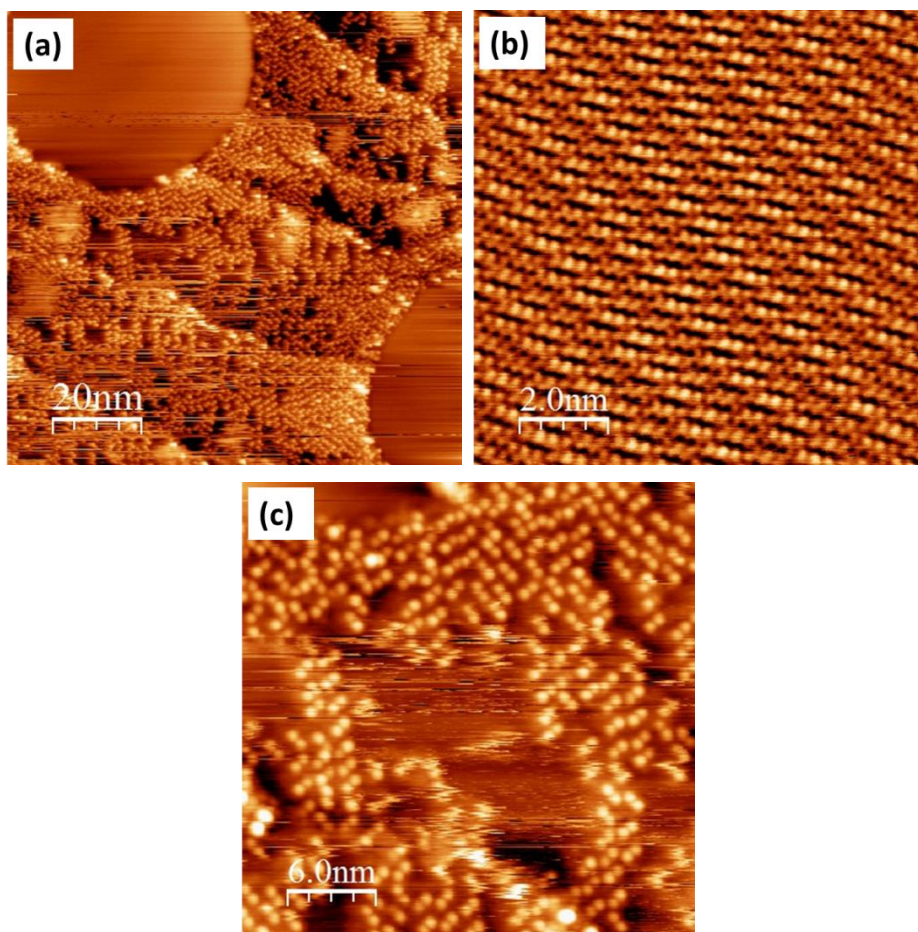


Figure 6.21: STM images showing (a) DBBA organo-metallic chains on the Cu(110) surface surrounded by graphene islands, ($V_b = -1.00V$, $I_t = 0.02nA$), (b) magnification of a graphene domain, ($V_b = 0.03V$, $I_t = 2.74nA$) and (c) the DBBA chains exhibiting the previously observed tilting effect, ($V_b = -1.00V$, $I_t = 0.02nA$).

Figure 6.21 (a) shows there are no DBBA molecules on the graphene domains. The DBBA molecules diffuse preferentially to the Cu(110) surface as opposed to the graphene islands, suggesting that the DBBA molecules exhibit a high degree of mobility on the graphene surface. Upon interaction with the Cu(110) substrate, they exhibit debrominated chain-like structures as previously observed in Chapter 5 (DBBA on the Cu(110) surface) and shown here in Figure 6.21 (c).

The alignment of the chains is again predominantly in the [001] direction of the Cu(110) substrate and the chains exhibit centre to centre distances of 1.30 ± 0.10 nm in agreement with previous measurements of 1.45 ± 0.05 nm and 1.21 ± 0.05 nm for DBBA on the

Cu(111) and Cu(110) respectively. Debromination and the subsequent chain formation, through radical addition by C-Cu-C bonding, have occurred.

Annealing this surface to 250°C shows no discernable change in the graphene domains (Figure 6.22 (a) and (b)) where a moiré periodicity of 1.37 ± 0.05 nm is measured which agrees closely with those measured from Figure 6.19 (b) (1.30 ± 0.05 nm). The tilt and alternating bright lobes in the debrominated DBBA molecules has now disappeared and instead appear square with widths of 0.93 ± 0.05 nm (Figure 6.22 (d)). This measurement is in close agreement with the width of a flat lying bianthracene molecule (0.97 nm). This suggests that the chains have flattened as a consequence of intra molecular cyclodehydrogenation between adjacent anthracene units.

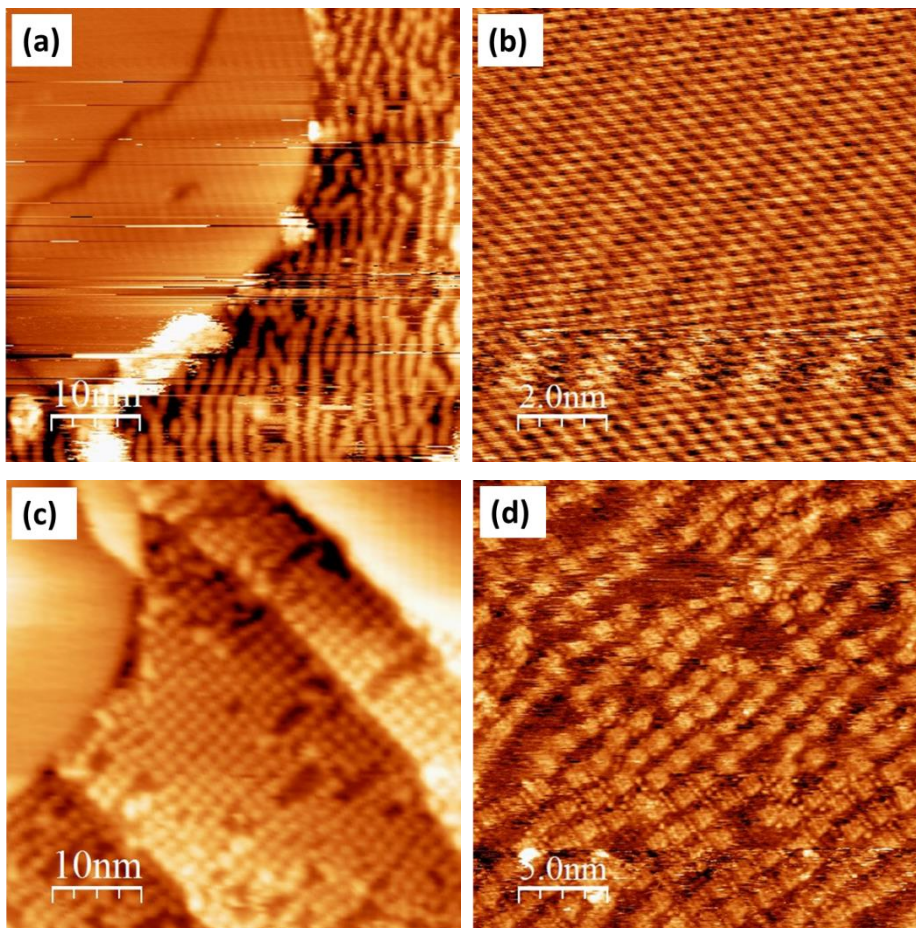


Figure 6.22: STM images of (a) and (c) exhibiting graphene and cyclodehydrogenated DBBA molecules, ($V_b = 1.36$ V, $I_t = 0.04$ nA) and ($V_b = 0.70$ V, $I_t = 2.50$ nA) respectively, (b) a magnified graphene domain, ($V_b = 0.02$ V, $I_t = 1.00$ nA) and (d) DBBA where copper 'spacers' are observed, ($V_b = 0.11$ V, $I_t = 1.98$ nA).

Copper atoms are observed between the flat lying molecules and contribute to the molecular centre to centre distance of 1.69 ± 0.05 nm. There is no direct evidence of the organo-metallic bonding and this is probably due to the low surface coverage of DBBA molecules. Using the known distance between copper rows in the [001] direction (0.361 nm) it is proposed that the cyclodehydrogenated DBBA molecules cover three underlying copper rows as observed and shown in Chapter 5 (Figure 5.6) and presented again here in Figure 6.23.

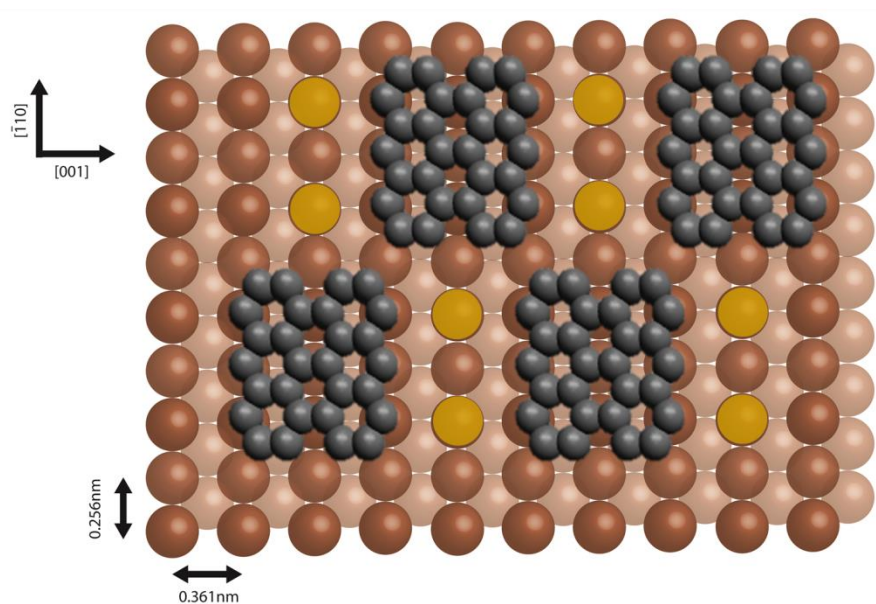


Figure 6.23: Schematic showing the proposed orientation of DBBA molecules on the Cu(110) surface.

Annealing to 350°C sees a disordering of the DBBA molecules accompanied by the onset of molecular decomposition as shown in Figure 6.24 whereas the graphene remains unaffected by the anneal.

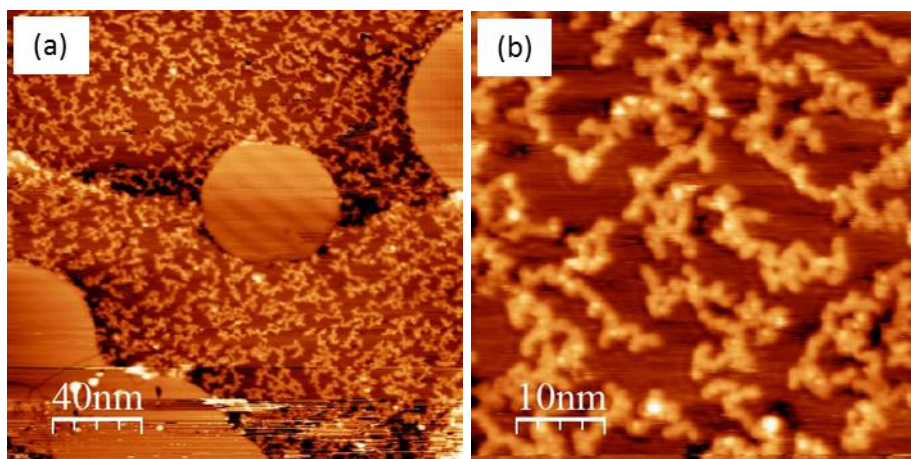


Figure 6.24: STM images of (a) the graphene domains surrounded by (b) disordered, decomposed DBBA molecules, ($V_b = 0.39V$, $I_t = 0.56nA$) and ($V_b = -1.12V$, $I_t = 0.10nA$) respectively.

The objective here was to produce chemically stable connections between neighbouring graphene domains using previous knowledge of GNR formation from DBBA precursor molecules. It is clear that the DBBA molecules form preferential chains on the Cu(110) substrate as previously observed. However, as before, GNR formation on the Cu(110) surface is restricted by the underlying substrate and hence this objective of graphene domains connected by graphene nanoribbons was not achieved. It is proposed that this experiment would prove more favourable on the Cu(111) surface where GNR formation and graphene have been independently observed.

6.4 Summary

The goal of this chapter was the bottom up fabrication of covalently bonded porphyrin structures through debromination and subsequent polymerisation via radical addition. Low and high coverage depositions of DBrDPP on the Cu(110) surface have been investigated through STM analysis.

At low coverages ($\sim 0.1\text{ML}$) after a 100°C anneal, the DBrDPP molecules form organo-metallic chains aligned along the [001] direction through a C-Cu-C interaction between subunits. At this stage, individual porphyrins are observed to diffuse on the Cu(110) surface until interaction and bonding with an existing chain occurs. This molecular diffusion is still evident after annealing to 250°C where a Ni-Cu exchange in the porphyrin macrocycle is observed. This exchange reaction completes after annealing to 300°C where all porphyrins have been metallated by copper atoms.

When a higher coverage of DBrDPP ($\sim 0.9\text{ML}$) was deposited onto Cu(110), the molecules again align in the [001] direction and exhibit the behaviour observed during low coverage analysis up to 300°C . Annealing this surface in steps from 500°C to 800°C results in decomposition at 500°C , followed by the formation of graphene domains, up to 100 nm wide at 700°C , and which remain stable to at least 800°C . The graphene domains exhibit a Moire rippling with varying periodicities have orientations approximately 120° to each other. Defects became evident and appear as mounds on the graphene domains. This occurs due to the graphene growth dynamics. Furthermore, isolated graphite flakes were observed which appeared to stack together more tightly than individual or bilayer graphene.

Finally it was proposed that GNRs, by DBBA deposition and subsequent annealing, could create covalent bonding between graphene domains. The DBBA molecules formed polymerised C-Cu-C anthracene chains. However, due to molecular mobility and low reactivity of the graphene domains resulted in DBBA diffusion and no chain growth on the domains themselves. GNRs were unable to form due to large molecular separation caused by copper atoms in the underlying Cu(110) surface.

6.5 References

- [1]Lipton-Duffin, J.A., Ivasenko, O., Perepichka, D.F. & Rosei, F. 2009, "Synthesis of Polyphenylene Molecular Wires by Surface-Confined Polymerization", *Small*, vol. 5, no. 5, pp. 592-597.
- [2]Doyle, C.M., Cunniffe, J.P., Krasnikov, S.A., Preobrajenski, A.B., Li, Z., Sergeeva, N.N., Senge, M.O. & Cafolla, A.A. 2014, "Ni-Cu ion exchange observed for Ni(II)-porphyrins on Cu(111)", *Chemical Communications*, vol. 50, no. 26, pp. 3447-3449.
- [3]Diller, K., Klappenberger, F., Allegretti, F., Papageorgiou, A.C., Fischer, S., Wiengarten, A., Joshi, S., Seufert, K., Eciya, D., Auwaerter, W. & Barth, J.V. 2013, "Investigating the molecule-substrate interaction of prototypic tetrapyrrole compounds: Adsorption and self-metalation of porphine on Cu(111)", *Journal of Chemical Physics*, vol. 138, no. 15, pp. 154710.
- [4]Bieri, M., Nguyen, M., Groening, O., Cai, J., Treier, M., Ait-Mansour, K., Ruffieux, P., Pignedoli, C.A., Passerone, D., Kastler, M., Muellen, K. & Fasel, R. 2010, "Two-Dimensional Polymer Formation on Surfaces: Insight into the Roles of Precursor Mobility and Reactivity", *Journal of the American Chemical Society*, vol. 132, no. 46, pp. 16669-16676.
- [5]Haq, S., Hanke, F., Dyer, M.S., Persson, M., Iavicoli, P., Amabilino, D.B. & Raval, R. 2011, "Clean Coupling of Unfunctionalized Porphyrins at Surfaces To Give Highly Oriented Organometallic Oligomers", *Journal of the American Chemical Society*, vol. 133, no. 31, pp. 12031-12039.
- [6]Hanke, F., Haq, S., Raval, R. & Persson, M. 2011, "Heat-to-Connect: Surface Commensurability Directs Organometallic One-Dimensional Self-Assembly", *Acs Nano*, vol. 5, no. 11, pp. 9093-9103.
- [7]Gonzalez-Moreno, R., Sanchez-Sanchez, C., Trelka, M., Otero, R., Cossaro, A., Verdini, A., Floreano, L., Ruiz-Bermejo, M., Garcia-Lekue, A., Martin-Gago, J.A. & Rogero, C. 2011, "Following the Metalation Process of Protoporphyrin IX with Metal Substrate Atoms at Room Temperature", *Journal of Physical Chemistry C*, vol. 115, no. 14, pp. 6849-6854.
- [8]Roeckert, M., Ditze, S., Stark, M., Xiao, J., Steinrueck, H., Marbach, H. & Lytken, O. 2014, "Abrupt Coverage-Induced Enhancement of the Self-Metalation of Tetraphenylporphyrin with Cu(111)", *Journal of Physical Chemistry C*, vol. 118, no. 3, pp. 1661-1667.
- [9]Fan, Q., Wang, C., Han, Y., Zhu, J., Kuttner, J., Hilt, G. & Gottfried, J.M. 2014, "Surface-Assisted Formation, Assembly, and Dynamics of Planar Organometallic Macrocycles and Zigzag Shaped Polymer Chains with C-Cu-C Bonds", *Acs Nano*, vol. 8, no. 1, pp. 709-718.

- [10]Di Giovannantonio, M., El Garah, M., Lipton-Duffin, J., Meunier, V., Cardenas, L., Revurat, Y.F., Cossaro, A., Verdini, A., Perepichka, D.F., Rosei, F. & Contini, G. 2013, "Insight into Organometallic Intermediate and Its Evolution to Covalent Bonding in Surface-Confined Ullmann Polymerization", *Acs Nano*, vol. 7, no. 9, pp. 8190-8198.
- [11]Gonzalez-Moreno, R., Sanchez-Sanchez, C., Trelka, M., Otero, R., Cossaro, A., Verdini, A., Floreano, L., Ruiz-Bermejo, M., Garcia-Lekue, A., Martin-Gago, J.A. & Rogero, C. 2011, "Following the Metalation Process of Protoporphyrin IX with Metal Substrate Atoms at Room Temperature", *Journal of Physical Chemistry C*, vol. 115, no. 14, pp. 6849-6854.
- [12]Gao, L., Guest, J.R. & Guisinger, N.P. 2010, "Epitaxial Graphene on Cu(111)", *Nano Letters*, vol. 10, no. 9, pp. 3512-3516.
- [13]Zhang Yan-Feng, Gao Teng, Zhang Yu & Liu Zhong-Fan 2012, "Controlled Growth of Graphene on Metal Substrates and STM Characterizations for Microscopic Morphologies", *Acta Physico-Chimica Sinica*, vol. 28, no. 10, pp. 2456-2464.
- [14]Tapaszto, L., Dumitrica, T., Kim, S.J., Nemes-Incze, P., Hwang, C. & Biro, L.P. 2012, "Breakdown of continuum mechanics for nanometre-wavelength rippling of graphene", *Nature Physics*, vol. 8, no. 10, pp. 739-742.
- [15]Rutter, G.M., Crain, J.N., Guisinger, N.P., Li, T., First, P.N. & Stroscio, J.A. 2007, "Scattering and interference in epitaxial graphene", *Science*, vol. 317, no. 5835, pp. 219-222.

Chapter 7

Future Work and Summary

7.1 Future Work

The objective of the future work is to employ ‘bottom-up’ techniques to grow atomically precise GNRs with well-defined lateral dimensions and large length-to-width aspect ratios. The intention is to control the electronic and optical properties of the graphene nanoribbons by functionalising them with organic molecules directly integrated into the body or ends of the nanoribbon. These techniques should allow control of the energy band-gap and add functionality to the GNRs. Such functionally-integrated GNRs (fGNRs), depending on their observed characteristics, could be used in applications such as sensing and molecular electronics ^[1]. The new challenge is to successfully grow and functionalise novel fGNRs and to characterise their properties.

Preliminary investigations have already been conducted to advance some of the work presented in this thesis in order to develop and realise this concept. Most significant is the incorporation of porphyrin molecules into the GNRs which have already been characterised and understood when using DBBA as a precursor. Porphyrin-terminated GNRs as well as GNRs with intermittent porphyrins within the ribbons have been identified as being worthy candidates for investigation due to the alterations in the electronic and physical characteristics which they could create. Additionally, the proposition of different building blocks for GNR creation could be considered e.g. pre-cursor molecules with increased increased dimensions.

Tetrabromophenyl porphyrin (TBrPP), shown in Figure 7.1, was co-deposited onto Au(111) with DBBA to confirm that covalent bonding between these molecules (through debromination reactions) would occur.

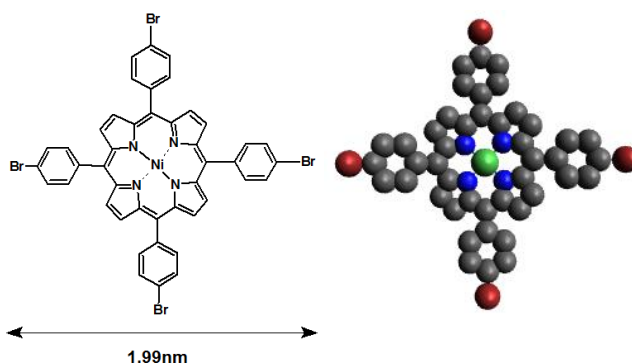


Figure 7.1: TBrPP molecule proposed as a promising candidate for GNR integration.

Figure 7.2 shows STM images after TBrPP and DBBA (in a ratio of approximately 1:3) were co-deposited onto the Au(111) surface and subsequently annealed to 415°C. This temperature was chosen since experience had shown that on Au(111) all debromination reactions and GNR formation had taken place above 400°C. Figure 7.2 (a) and (c) show short chains of GNRs (3.5 ± 0.5 nm in length) have formed between large areas of covalently bonded predominantly disordered TBrPP molecules. GNRs linking the disordered TBrPP networks as indicated by the circled areas in Figure 7.2 (a) are observed and magnified in Figure 7.2 (b). Similar structures are shown in Figure 7.2 (c) and a magnified version in Figure 7.2 (d). A graphical representation of the bonding configuration between TBrPP and DBBA is presented in Figure 7.2 (e), based on the magnified image in Figure 7.2 (c).

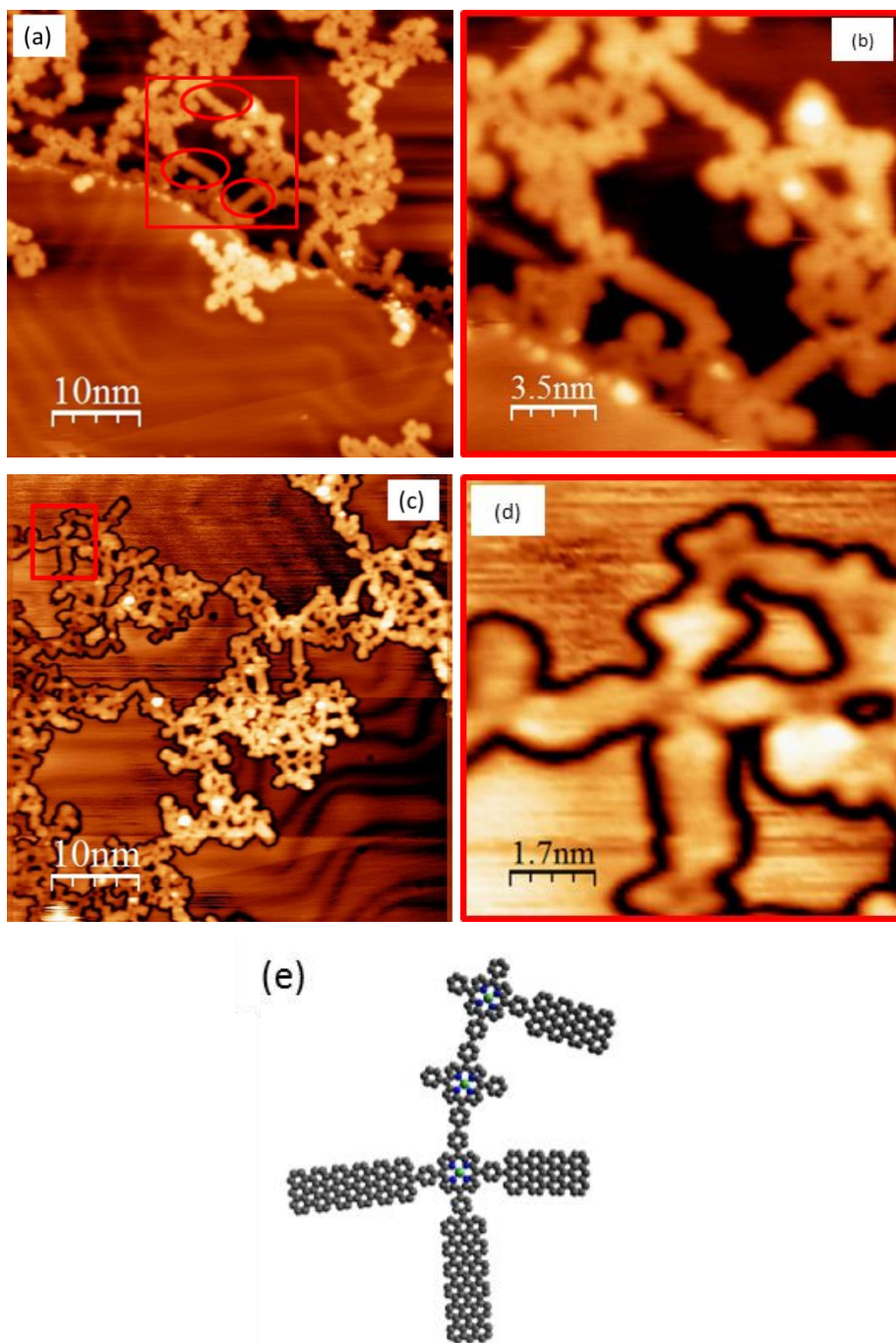


Figure 7.2: STM images ((a), (b), (c) and (d)) showing TBrPP covalently bonding with DBBA molecules and (e) a schematic model of the bonding configuration shown in (d).

The disordered porphyrin network and multidirectional growth of GNRs emanating from these TBrPP networks are due to the in plane rotation of the phenyl rings relative to the macrocycle, creating different directions for nanoribbon growth.

This experiment was repeated but on this occasion TBrPP and DBBA were deposited in a significantly altered ratio (approximately 1:8) in the hope that elongated GNRs could be formed with a reduced number of porphyrin links. STM images shown in Figure 7.3 are the results of this altered molecular ratio deposition after annealing again to 415°C.

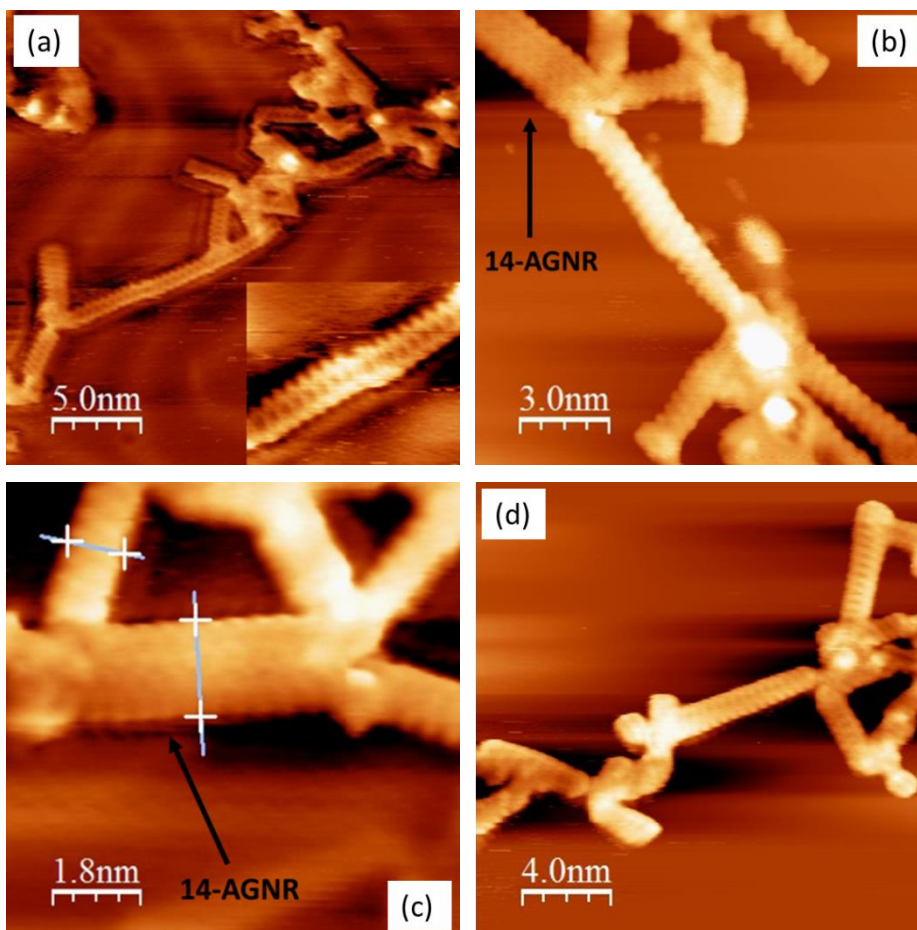


Figure 7.3: STM images showing covalent bonding between TBrPP molecules and GNRs. (a) chains up to 15 nm are observed, (b) and (c) 14-AGNRs and (d) disordered porphyrin junctions.

Figures 7.3 (a) and (d) show a significant increase in the GNR length between adjacent and disordered TBrPP molecules. This is attributed to the increased ratio of DBBA to TBrPP molecules. GNR lengths now range from a few nanometres up to 15 nm where junctions of porphyrins interrupt their growth. 14-GNRs are observed (highlighted by a black arrow in Figure 7.3 (b) and (c)) where cross cyclodehydrogenation between adjacent 7-AGNRs has occurred. The widths of the 7-ANGRs (measured as 1.28 ± 0.05 nm) are in close agreement

to those previously observed in Chapter 4 on the Au(111) surface (1.32 nm). The 14-AGNRs, previously unseen on the Au(111) surface, have widths measuring 1.88 ± 0.05 nm. This distance is in close agreement to the width of 14-AGNRs found on Ag(111) (2.11 nm) and to the theoretical width (1.87 nm). As discussed previously, the fact that this is not double the width of a 7-AGNR is due to the cross cyclodehydrogenation between adjacent 7-AGNRs, eliminating steric hindrance in the adjoining region.

It can be concluded from this preliminary study that although TBrPP and DBBA are able to form fGNRs, the ability of the phenyl rings to rotate in plane, relative to the TBrPP macrocycle proves troublesome to the growth of fGNRs. Therefore, the pathways for covalent bonding must be reduced or the outer phenyl rings eliminated from the precursor porphyrin molecule in order to achieve more ordered networks.

For this reason, 5,15-dibromo-10,20-diphenyl porphyrins (DBDPP, Figure 7.4 (a)) with two bromine atoms, directly bonded to the macrocycle are proposed as a better candidate to form functionalised nanoribbons with DBBA (Figure 7.5 (a)). DBDPP deposited onto Cu(110) (see Chapter 6) does not result in cyclodehydrogenation between molecules. This is partly due to the organo-metallic bonds and copper adatoms which restrict direct porphyrin-porphyrin covalent bonding. Therefore, investigation of DBDPP on the Cu(111) surface could prove more favourable and enable fGNRs to form. Alternatively, 5-bromo-10,15,20-triphenyl porphyrins (BrTriPP) (Figure 7.4 (b)) can be incorporated at the GNR termination point due to the single radical bond once debromination occurs. The resultant porphyrin terminated fGNR is shown in Figure 7.5 (b).

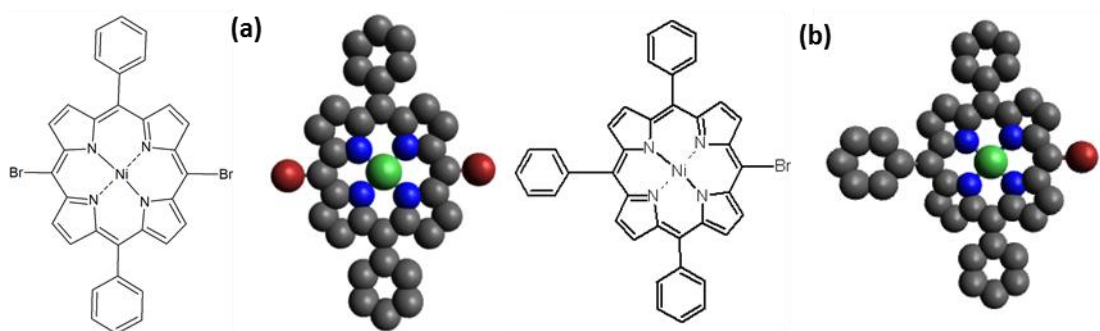


Figure 7.4: (a) 5,15-dibromo-10,20-diphenyl and (b) 5-bromo-10,15,20-triphenyl.

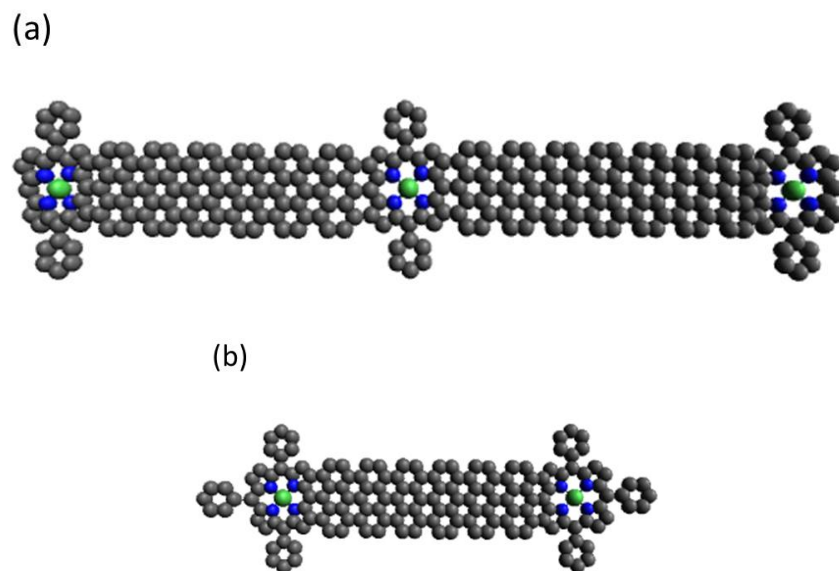


Figure 7.5: (a) Proposed arrangement of DBDPP/DBBA and (b) BrTriPP/DBBA.

Initial insight has been obtained of the BrTriPP/Cu(111) system. Approximately 0.05ML of BrTriPP was deposited onto RT Cu(111) and subsequently annealed to 250°C. BrTriPP molecules are observed to covalently bond as shown in Figure 7.6.

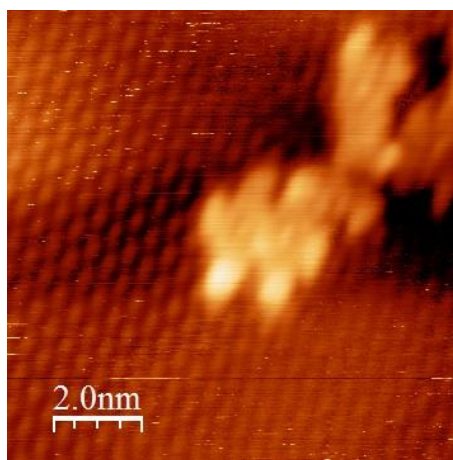


Figure 7.6: Evidence of dimer formation between two BrTriPP molecules.

Dimers of BrTriPP are observed, with a macrocycle centre-to-centre separation of 0.89 ± 0.02 nm indicating that direct covalent bonding between porphyrins has occurred,

i.e. no organo-metallic bonding. There is only one bromine atom per molecule which will result in BrTriPP terminated GNRs.

To date GNRs fabricated by bottom-up approaches are limited to those with lateral dimensions smaller than 1 nm (essentially 7-AGNRs), which show absorption only up to 670 nm and have band gap larger than 2.0 eV ^[2,3]. For future electronic device applications, it is essential to synthesise GNRs with tailored band gaps. There are synthetic routes to a range of molecular precursor building blocks that provide bottom-up routes to GNRs having a range of widths (and hence band gaps), and provide a facile route to functionalisation and improved solubility of the GNRs. The overall synthetic strategy is based on the Suzuki cross-coupling, Yamamoto coupling and Scholl reactions ^[4, 5, 6]. Results provide, for example, 2,2'-di((1,10-biphenyl)-2-yl)-10,10'-dibromo-9,9'-bianthracene; a precursor suitable for the assembly of 13-AGNRs. Examples of proposed molecular building blocks, synthesised using these cross-coupling reactions, and the resulting GNRs are shown in Figure 7.7. Precursors could be synthesised to provide variation in the width (17-AGNRs (blue)), edge-functionalised 13-AGNRs (purple and black) and porous 17-AGNRs (red). Finally, Figure 7.8 shows the nitrogen and oxygen examples for functionalization of the GNR edges which could potentially prove useful due to their improved solubility.

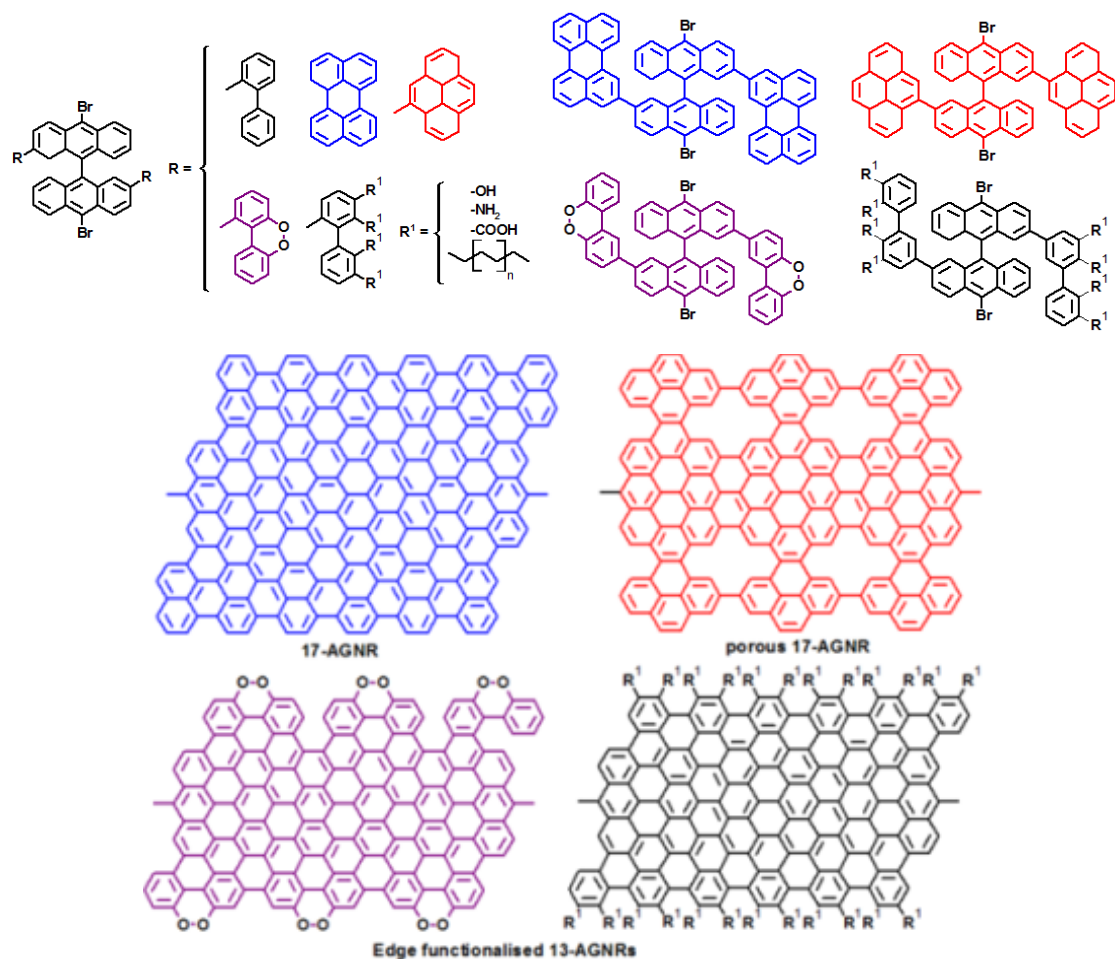


Figure 7.7: Molecular building blocks, synthesised precursor molecules for GNR growth and the resultant GNRs.

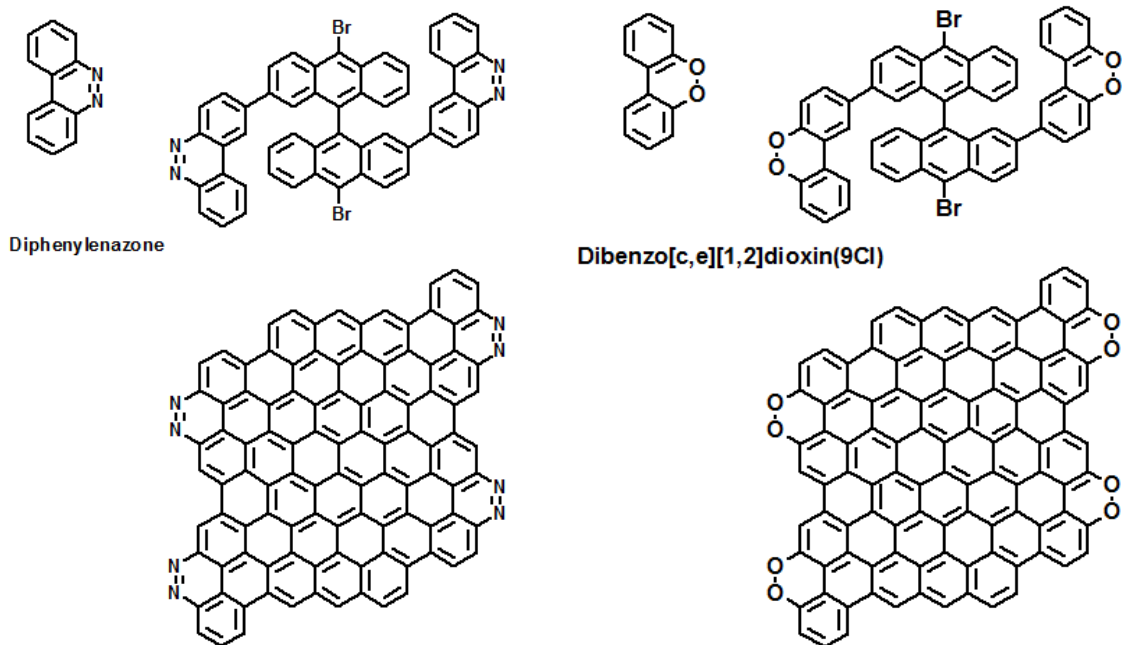


Figure 7.8: Examples of nitrogen and oxygen functionalised Graphene Nanoribbons.

7.2 Summary

This thesis presents an investigation of the deposition, self-assembly, debromination, network formation and molecule/substrate interaction of organic materials on metal surfaces. These processes were characterised using Scanning Tunnelling Microscopy, X-ray Photoelectron Spectroscopy, Photoemission Spectroscopy and X-ray Absorption Spectroscopy.

Initially, HBTP was investigated on Au (111), Ag(111) and Cu(111) surfaces to gain an understanding of the debromination process and subsequent covalent bonding which were found to depend on the reactivity of the substrate. These results are presented in Chapter 3. Covalently bonded structures were observed on all three surfaces with limited order due to the presence of six bromine atoms per molecule i.e. six possible bonding radicals after debromination occurs. When covalent bonding takes place, competition for bonding sites leads to predominantly disordered structures. Furthermore, the dissociated bromine on the Ag and Cu surfaces interferes with the molecular network growth. Gold proved to be the most amenable surface for polymerised nano network formation since desorption of bromine occurred at lower temperatures in comparison to silver and copper surfaces. Pores of differing sizes and shapes were observed from squares to irregular hexagons. There was evidence of dissociated bromine forming a $(\sqrt{3} \times \sqrt{3})R30^\circ$ structure on both the Ag(111) and Cu(111) surfaces. The most significant conclusion derived from the investigation of HBTP deposition on the three (111) surfaces were that the reactivity of the substrates varies considerably, gold being the least reactive and copper the most.

These initial findings were followed by an investigation of DBBA deposition on the Au, Ag and Cu (111) surfaces (Chapter 4) and also on the Cu(110) substrate (Chapter 5). Evidence of H-terminated 7-AGNRs were observed on the Au(111), Ag(111) and Cu(111) surfaces via debromination, polymerisation and subsequent dehydrogenation. A comparison of reactivity of the substrates shows that debromination, resulting in tilted polymer chains, occurs at RT, 150°C and 200°C for Cu, Ag and Au respectively. Further annealing to 220°C, 350°C and 400°C for Cu, Ag and Au respectively results in cyclodehydrogenated graphene nanoribbons. In addition, 14-AGNRs were observed on the Ag(111) surface due to cross dehydrogenation between two adjacent 7-AGNRs. GNRs on the Cu(110) substrate were not observed due to the formation of organo-metallic bonds and copper surface atoms

inhibiting nanoribbon growth. However, thermally decomposing the DBBA molecules and annealing to temperatures in excess of 700°C, allows the decomposed carbon material to reform into graphene islands. These graphene islands were also observed on the Cu(111) surface and in both cases, a moiré pattern is observed due to a lattice mismatch between the graphene over layer and the underlying copper.

An investigation of the growth dynamics of DBDPP on the Cu(110) surface and subsequent addition of DBBA to the resulting system were presented in Chapter 6. At low coverages, and after annealing the RT deposited DBDPP molecules to 100°C, chains of covalently bonded porphyrins formed along the [001] direction of the Cu(110) substrate. Measurements indicate that a C-Cu-C organo-metallic bond has taken precedence over direct porphyrin-porphyrin bonding. Furthermore, the individual DBDPP molecules exhibit mobility on the Cu(110) surface until bonding to an existing chain is achieved. These observations are still evident after annealing to 250°C. At this stage, a Ni-Cu exchange has occurred in the macrocycle core. This ion exchange completes after annealing to 300°C where all porphyrins appear to have a vacancy which is attributed to the bias conditions between the STM tip and DBDPP/Cu(110) substrate.

A higher coverage of DBDPP on the Cu(110) surface results in similar behaviour up to 300°C. Thereafter, the molecules decompose at 500°C followed by the emergence of graphene at 700°C. Graphene domains up to 100 nm wide which generally exhibit a moiré rippling effect with varying periodicities having orientations of approximately 120° to each other are observed. Defects became evident and appear as mounds on the graphene domains. This occurs due to the graphene growth process and competition for bonding. Furthermore, isolated graphite flakes were observed which appeared to stack together more tightly than individual or bilayer graphene.

Finally it was proposed that GNRs, formed by DBBA deposition and subsequent annealing, could potentially create covalent bonding between graphene domains. The DBBA molecules formed polymerised C-Cu-C anthracene chains. However, due to molecular mobility and low reactivity of the graphene domains, the DBBA molecules diffused on the graphene surface and no chain growth occurred. Furthermore GNRs were unable to form on the underlying Cu(110) surface.

The future work presented previously in this chapter show that the plausibility for functionalised graphene nanoribbons (fGNRs) by incorporating porphyrin molecules into the already established and understood DBBA GNRs.

It is with hope, that the conclusions and findings presented in this study, lead the way for further discussion and experimental investigation into the chemical and physical reactions of molecules on metal surfaces.

7.3 References

- [1]Lin, Y.-., Dimitrakopoulos, C., Jenkins, K.A., Farmer, D.B., Chiu, H.-., Grill, A. & Avouris, P. 2010, "100-GHz Transistors from Wafer-Scale Epitaxial Graphene", *Science*, vol. 327, no. 5966, pp. 662-662.
- [2]Wu, J.S., Gherghel, L., Watson, M.D., Li, J.X., Wang, Z.H., Simpson, C.D., Kolb, U. & Mullen, K. 2003, "From branched polyphenylenes to graphite ribbons", *Macromolecules*, vol. 36, no. 19, pp. 7082-7089.
- [3]Yang, X., Dou, X., Rouhanipour, A., Zhi, L., Raeder, H.J. & Muellen, K. 2008, "Two-dimensional graphene nanoribbons", *Journal of the American Chemical Society*, vol. 130, no. 13, pp. 4216-+.
- [4]Vo, T.H., Shekhirev, M., Kunkel, D.A., Morton, M.D., Berglund, E., Kong, L., Wilson, P.M., Dowben, P.A., Enders, A. & Sinitskii, A. 2014, "Large-scale solution synthesis of narrow graphene nanoribbons", *Nature Communications*, vol. 5, pp. 3189.
- [5]Bennett, P.B., Pedramrazi, Z., Madani, A., Chen, Y., de Oteyza, D.G., Chen, C., Fischer, F.R., Crommie, M.F. & Bokor, J. 2013, "Bottom-up graphene nanoribbon field-effect transistors", *Applied Physics Letters*, vol. 103, no. 25, pp. 253114.
- [6]Chen, Y., de Oteyza, D.G., Pedramrazi, Z., Chen, C., Fischer, F.R. & Crommie, M.F. 2013, "Tuning the Band Gap of Graphene Nanoribbons Synthesized from Molecular Precursors", *Acs Nano*, vol. 7, no. 7, pp. 6123-6128.